UNIVERSIDAD DE BUENOS AIRES
Facultad de Ciencias Exáctas y Naturales
Departamento de Física

Medición del flujo de neutrinos cósmicos ultra energéticos con el detector de superficie del Observatorio Pierre Auger

Trabajo de Tesis para optar por el título de
Doctor de la Universidad de Buenos Aires en el área Ciencias Físicas
por **Yann Guardincerri**

Directores de Tesis: Prof. Ricardo Néstor Piegaia y Prof. Jaime Alvarez Muñiz

Lugar de Trabajo: Dpto. Física - FCEyN - UBA

Buenos Aires, Argentina
24 de junio de 2013

Resumen

Medición del flujo de neutrinos cósmicos ultra energéticos con el detector de superficie del Observatorio Pierre Auger

El Detector de Superficie del Observatorio Pierre Auger es sensible a tau neutrinos que cruzan la Tierra de forma rasante interactuando en su corteza. Los leptones tau que surgen de las interacciones via corriente cargada pueden emerger de la Tierra y decaer en la atmósfera produciendo lluvias de partículas casi horizontales que contienen una componente electromagnética significativa. En esta tesis se diseñan técnicas de reconstrucción y de identificación que permiten distinguir estas lluvias de las producidas por rayos cósmicos iniciados por protones o núcleos de hierro, usando como observable la estructura temporal de las señales que se detectan en los detectores de agua que miden radiación de Cherenkov. Se describe el procedimiento de búsqueda de neutrinos, el método desarrollado para calcular la exposición del observatorio y las incertezas sistemáticas asociadas. Ningún candidato a neutrino fue encontrado en los datos adquiridos entre 1 de Enero del 2004 hasta 31 de Diciembre del 2012. Asumiendo un flujo diferencial $\Phi(E_\nu) = k \cdot E_\nu^{-2}$, se fija un límite superior con un nivel de confianza del 90% al flujo difuso de neutrinos de todos los sabores de $k < 5 \times 10^{-8}$ GeV cm^{-2} s^{-1} sr^{-1} en el intervalo de energías de 10^{17} eV a $10^{19.1}$ eV. Se testean modelos astrofísicos concretos de producción de neutrinos, y se derivan límites a flujos de fuentes puntuales en función de su declinación.

Palabras claves: astropartículas, neutrinos cosmogénicos , neutrinos UHE, rayos cósmicos, Observatorio Pierre Auger

Abstract

Measurement of the ultra-high energy cosmic neutrino flux with the Surface Detector array at the Pierre Auger Observatory

The Surface Detector of the Pierre Auger Observatory is sensitive to Earth-skimming tau neutrinos that interact in Earth's crust. Tau leptons from charged-current interactions can emerge and decay in the atmosphere to produce a nearly horizontal shower with a significant electromagnetic component. In this thesis techniques are developed to reconstruct and distinguish these showers from the ones produced by regular hadronic cosmic rays by the broad time structure of the signals in the water-Cherenkov detectors. The neutrino search procedure, the method to compute the observatory exposure and the associated systematic uncertainties are described. No neutrino candidate has been found in data collected from 1 January 2004 to 31 December 2012. Assuming a differential flux $\Phi(E_\nu) = k \cdot E_\nu^{-2}$ in the energy range from 10^{17} eV $- 10^{19.1}$ eV, we place a 90% CL upper limit on the all flavour neutrino diffuse flux of $k < 5 \times 10^{-8}$ GeV cm^{-2} s^{-1} sr^{-1}. Concrete astrophysical neutrino models are tested and limits to point-like source fluxes are derived as a function of declination.

Keywords: astroparticles, cosmogenic neutrinos, UHE neutrinos, cosmic rays, Pierre Auger Observatory

Acknowledgments

Mi experiencia en el Observatorio Pierre Auger fue excelente. Voy a estar siempre agradecido a mis directores Ricardo Piegaia y Jaime Alvarez Muñiz. Fue un inmenso placer trabajar bajo su tutela y aprender de ellos en diferentes aspectos de mi formación. Los dos me dejaron un ejemplo gigante de lo que significa trabajar en ciencia.

Estoy profundamente agradecido con Javier Tiffenberg. Para mi sos un grande! No tengo palabras para agradecerte todo lo que me enseñaste y ayudaste durante estos años.

Hay mucha gente de la colaboración que contribuyó mediante discusiones con mi trabajo de doctorado. Particularmente quiero agradecerle a Enrique Zas, Gonzalo Parente, Sergio Navas, Jose Luis Navarro, Mathieu Tartare, Pierre Billoir, Markus Roth, Carla Bonifazi, Isabelle Lhenry-Yvon, Piera Ghia, Paolo Privitera, Diego Harari y Esteba Roulet.

Estoy infinitamente agradecido a mi familia. A mis papás, Carlos e Inés, quienes me formaron como persona y lo siguen haciendo cada día con su ejemplo. Muchísimas gracias por ser como son, por su incondicional amor y apoyo durante todos estos años de esfuerzo para que pueda alcanzar mis objetivos. A mi hermano que me muestra lo que significa la pasión y la lealtad. Gracias Lu! Te admiro montones. A mis primos, tíos y abuelos, quienes siempre están cuando necesito una mano. En especial a Gusti, Caro y Sampipit que me prestaron la oreja cuando necesitaba hacer catarsis.

A mis amigos gracias por estar durante todos estos años de esfuerzo, por compartir asados, noches de teg y mucho más. En especial a Santi quien sabe mostrarme mis falencias.

A toda la gente del grupo experimental de altas energías del Departamento: Hernán, Pablo, Laura, Gastón, Sabrina, Orel y Gustavo. En particular, gracias Pablo por ser mi compañero de aventuras en Auger durante los últimos años, gracias Hernán por cada vez que te pedí ayuda y encontraste el tiempo para tratar de responder y gracias Gustavo por tus consejos.

Hay mucha más gente que estuvo muy presente durante mi paso por la Facultad.

En particular, muchas gracias a Mati, Diego, Tifi, Fede, Guille y tantos más.

Me gustaría resaltar mi agradecimiento a toda la gente que trabaja para que la Facultad de Ciencias Exáctas y Naturales funcione. Esta Institución tiene mucho que ver en mi formación como persona y me siento extremadamente orgulloso de haber pertenecido a ella durante los últimos años.

Por último, pero de importancia mayúscula quiero agradecerle a Tef, el cuore de mi cuore, por la paciencia de estos últimos meses y por compartir los sueños de futuro. Me diste la fuerza para terminar!

Contents

1

Introduction

The field of astroparticle physics is currently undergoing rapid development. The traditional messenger on the sky, the photon, has been complemented starting early last century by charged cosmic rays observations and, during the last decades, by the development of neutrino astrophysics. They are all rich messengers allowing us to probe the properties of astrophysical sources.

Neutrino astronomy is only just beginning. It has the possibility to open a new window on the universe, expanding what is possible to know about astrophysical phenomena. Charged cosmic rays are deflected by magnetic fields and gamma rays can be absorbed by intervening material or pair produce on photon backgrounds prevalent throughout the universe. Neutrinos suffer from neither problem since they are neutral and only interact via the weak force. Even though they are difficult to observe particle astrophysicists are stepping up to the challenge. The era of dedicated high-energy neutrino telescopes began in earnest a couple of decades ago and it promises to open a new and exciting window on the Universe. There are several extensive reviews [1] highlighting the potential physics and astrophysics objectives using the neutrino messenger.

In this dissertation, we focus on the search of neutrinos in the energy interval between 10^{17} eV to 10^{20} eV with the Pierre Auger Observatory. This thesis is organized as follows. In this Chapter we review the present status of theoretical and experimental neutrino astrophysics. Chapter 2 describes extended air showers and, in particular, the ones produced by neutrinos. Chapter 3 presents an overview of the Pierre Auger Observatory. The processes involved in neutrino simulations are explained in Chapter 4. The reconstruction and identification of neutrinos is the subject of Chapters 5 and 6. In Chapter 7 we detail the determination of the observatory exposure, i.e., its sensitivity to cosmological neutrinos. Chapter 8, finally, is dedicated to the search results and the comparison with theoretical predictions.

1.1 Why ultra-high energy neutrinos?

The study of charged ultra-high energy cosmic rays (UHECRs) has stimulated much experimental and theoretical activity in the field of Astroparticle Physics. Although, their energy spectrum is measured over an astonishing energy range covering 14 orders of magnitude, many mysteries remain to be solved, such as their origin and production mechanism. In particular, charged UHECRs measurements suffer from two limitations, source pointing and the GZK cutoff.

At energies below $10^{19.5}$ eV, charged particles trajectories are substantially bent by galactic and intergalactic magnetic fields and their arrival direction on Earth does not point back to their source of origin.

The GZK cutoff, proposed in the 1960s by Greisen, Zatsepin and Kuzmin [2,3], arises as cosmic rays above an energy $\geq 5 \times 10^{19}$ eV rapidly lose energy through interactions with the photons of the CMB via:

$$p + \gamma_{\mathrm{CMB}} \rightarrow \Delta^{+}(1232) \rightarrow p + \pi^{0} \quad \text{or} \quad n + \pi^{+} \tag{1.1}$$

The attenuation length for this process is $L_{att} = \frac{L_{int}}{y}$, where y is the average energy fraction lost per interaction and L_{int} is the interaction length, $L_{int} = (\sigma_{p\gamma} \times n_{\gamma})^{-1}$. Typical values are $\sigma_{p\gamma} \sim 10^{-28}$ cm^2, $n_{\gamma} = 410\,\mathrm{cm}^{-3}$ and $y \sim 0.5$[1], resulting in $L_{att} = (\sigma_{p\gamma} \times n_{\gamma} \times y)^{-1} \sim 15$ Mpc. Since at these energies CRs are likely extragalactic, the GZK mechanism limits the maximum energy that can be observed on the Earth and predicts the cosmic ray spectrum to be suppressed above 50 EeV [2].

The cosmic ray experiments HiRes [4] and AGASA [5] early on reported conflicting results regarding the flux of particles above $10^{19.5}$ eV. However, the Pierre Auger Observatory combining the detection techniques from these two experiments at higher statistics confirmed the expected break in the spectrum [6], as shown in Figure 1.1. The break at $10^{19.6}$ eV is consistent with the expectation from the GZK cutoff, although the possibility that the sources themselves fail at accelerating particles at the highest energies cannot yet be excluded .

Likewise, photons above $\sim 10^{14}$ eV of extragalactic nature, never reach our local neighborhood due to electron pair production when they collide with the CMB [7,8]:

$$\gamma_{\mathrm{UHE}} + \gamma_{\mathrm{CMB}} \rightarrow e^{-} + e^{+}$$

In Figure 1.2 the attenuation length of the photons as a function of their energy is shown. Depending on their energy the γ_{UHE} can interact also with the infrared background radiation (IR) [9] or with the universal radio background (URB) [10].

This leaves the third type of messenger – the neutrino – as an option for investi-

[1] $y \sim 0.2$ at threshold energies and increases up to 0.5.
[2] 1 EeV=10^{18} eV

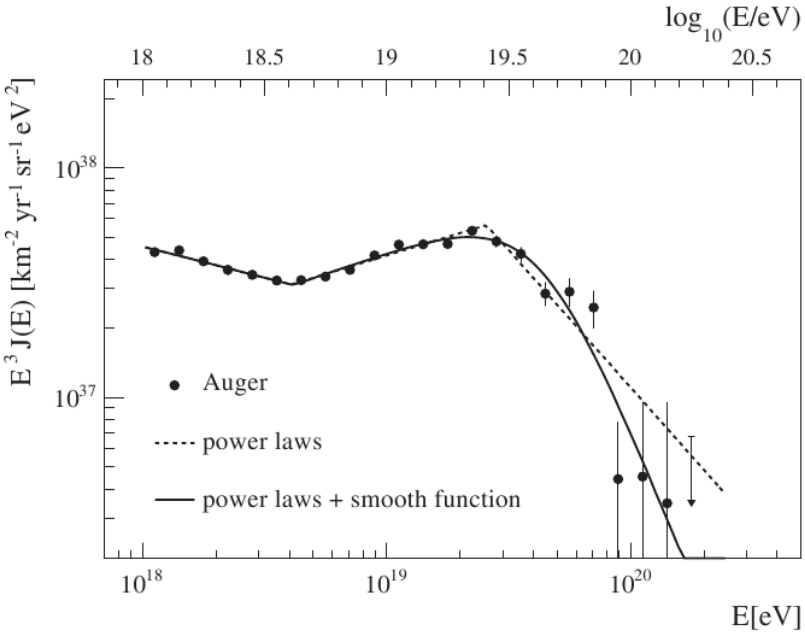

Figure 1.1 The UHECR spectrum obtained by the Pierre Auger Observatory. It is fitted with three power-law functions (dashed) and two power-law plus a smooth function (solid line). Only statistical uncertainties are shown. The systematic uncertainty on the energy scale is 22%.

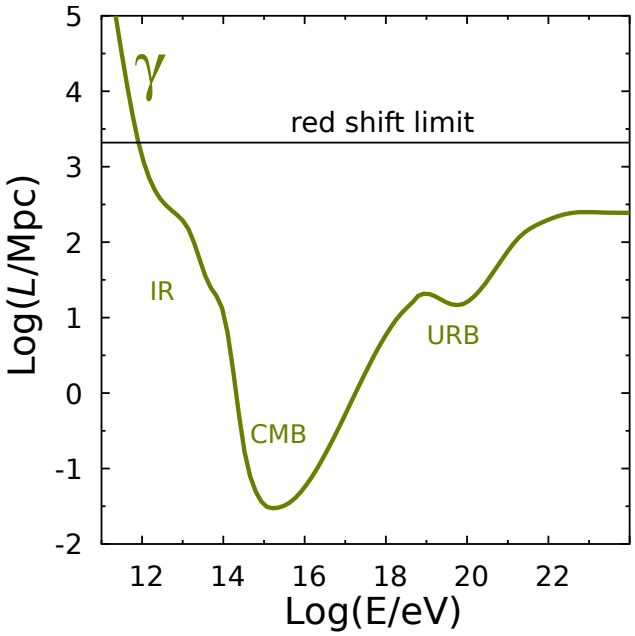

Figure 1.2 Attenuation length L for photons [11]. Photons with energy between 10^{14} and 10^{18} eV cannot reach the Earth if created at distances larger than 1 Mpc. Labels IR, CMB and URB (see text) indicate the dominant background against which the γ_{UHE} interact.

gation at the highest reaches of astrophysics. Indeed, soon after the GZK mechanism was proposed, it was realized that high energy neutrinos, which we call cosmogenic or GZK neutrinos, were a natural by-product of that process through its consequent pion decay [12, 13]:

$$\pi^+ \rightarrow \mu^+ + \nu_\mu \rightarrow e^+ + \nu_e + \bar{\nu}_\mu + \nu_\mu \tag{1.2}$$

Neutrinos do not suffer from any of the aforementioned disadvantages. They interact only through the weak interaction with a very small cross section. They travel cosmological distances without interacting and, moreover, if they are produced at the source, they escape from the object without loosing energy. As they are electrically neutral, they will not be bent by the magnetic fields of the universe and point back to their origin. Therefore, neutrinos are unique messengers with which we can probe the possible sources of cosmic rays and study the mechanism of UHECR interaction during their propagation in the Universe. Furthermore, with energies above 10^{17} eV, they would produce interactions with nucleons at center-of-mass energies near 100 TeV, exceeding those achieved at terrestrial accelerators. This provides a laboratory to search for new physics beyond the scope of the Standard Model of particle physics.

In the following sections of this chapter, we will present a discussion of astrophysical neutrino sources and fluxes, namely from the GZK mechanism, Active Galactic Nuclei (AGNs) and Gamma Ray Bursts (GRBs). We also briefly survey past, current and future experimental endeavors in the field.

1.2 Potential Sources of Diffuse Neutrino Flux

Various models in the literature predict UHE neutrinos and estimate their corresponding fluxes. As mentioned, the observations of CRs above 50 EeV and a cutoff in the spectrum imply the likely existence of cosmogenic neutrinos. In this case the neutrinos are produced during the propagation of UHECRs through the Universe. They could also potentially be produced by the acceleration of protons and nuclei in active galactic nuclei (AGN) [14], or by photopion production in cosmological gamma ray burst (GRB) [15]. Detectors such as AMANDA, or IceCube, its successor, are well-suited to search for sources with strong power-law ($\sim E^{-2}$) energy spectra that extends from TeV to above the PeV scales. Sources that emit neutrinos with energy spectra that peak at energies above 100 PeV are expected to have lower fluxes which require detectors with larger exposures.

It has been previously speculated that UHE neutrinos could also possibly be associated with the decays of extremely massive exotic particles such as topological defects [16], or the interaction of energetic neutrinos with Big-Bang relic cosmic background neutrinos via the Z-burst resonance [17]. These ideas, primarily moti-

vated to explain the highest energies cosmic rays, have now been severely constrained by recent experiments. A review can be be found in [18]. In the next subsections we summarize the main ideas.

1.2.1 GZK Neutrinos

Greisen, Zatsepin and Kusmin proposed that as cosmic rays with energies greater than 5×10^{19} eV propagate in the universe, they interact with the cosmic microwave background and generate neutrinos via pion decay, equation1.2.

The presence of the GZK cutoff hint that UHECRs are likely to be extragalactic. This implies that GZK neutrinos are the most secure predictions for neutrino fluxes in the energy interval between 10^{16} eV and 10^{21} eV. Nevertheless there are significant theoretical uncertainties in the calculations as we see next.

Estimates of the flux and shape of the GZK neutrino flux depend on the following factors [19–23]:

1. Composition of UHECRs,
2. UHECR energy spectrum (spectral shape, normalization and energy cutoff),
3. Cosmological model,
4. Cosmological evolution of the sources with redshift,
5. Proton-photon cross section, and
6. Neutrino oscillations.

1. Composition of UHECR

The first predictions of the cosmogenic neutrino flux assumed that the UHECR primaries were pure protons. More recent cosmogenic neutrino fluxes calculations [20, 24] take pure ^{56}Fe, ^{4}He, or ^{16}O and mixtures of these nuclei with protons as the primaries. The heavier nuclei lose energy via photo-disintegration, in which secondary nucleons are produced. The photopion production of these secondary nucleons creates UHE neutrinos. In addition, a small flux of anti-electron neutrinos are produced via neutron decays [25] but the energies are too small to be of interest to Auger. For non-pure proton composition, the neutrino flux is small compared with that expected from a pure proton component [24]. The energy per nucleon after photo-disintegration is much smaller than the primary energy (in the case of Fe, $\frac{E}{A} \sim \frac{E_p}{56}$) and may be too low to interact by the GZK process. Some neutrino flux estimations assume the sources inject a mixture of primaries with the same initial abundances as the observed Galactic cosmic rays [22]. Changing the primary component produces an uncertainty in the prediction of neutrino fluxes of more than an order of magnitude.

Recent experimental results by Auger [26] , though highly debated, indicate that the flux of UHECRs may be dominated by heavier nuclei. This is at variance with the results from HiRes, and more recently, Telescope Array (TA) [27]. Conversely, if neutrino fluxes are observed above the predictions from a large Z cosmic ray composition, they will shed light on the elemental composition of extragalactic cosmic ray sources or even rule out heavy composition.

2. Energy profile

The injection spectrum of UHECR can be inferred from experimental results of cosmic ray detectors on Earth. Typically it is assumed that the UHECR spectrum at injection is a power-law with the following energy dependence:

$$\frac{dN}{dE} = P_0 \times E^{-\alpha} \times \exp\left(-\frac{E}{E_c}\right) \tag{1.3}$$

where P_0 is a normalization constant. The spectral index α lies between 1.8 and 2.7, favored to be close to $\alpha \approx 2.3$. The cutoff energy at injection, E_c , is assumed to be between 10^{20} eV and 10^{23} eV. The values of α and E_c are both dependent on the corresponding source characteristics and the acceleration mechanism of cosmic rays at the source. Once the spectral index and cutoff energy are set, the normalization is chosen so that the propagated CRs at Earth fit the observed CR spectrum. A steeper injection spectrum and smaller cutoff energy generate smaller neutrino fluxes at 10^{18} - 10^{19} eV due to the decreased number of protons at high energies that would be responsible for such neutrinos.

3. Cosmological model

The cosmology of the Universe is another factor that drives the uncertainty of the GZK neutrino flux. Astrophysical observations now point to models with a cosmological constant Λ [28], compared with the flat, mass dominated Einstein-de Sitter Universe ($\Omega_M = 1$) typically assumed by calculations prior to mid-90's. The currently favored model is one with $\Omega_\Lambda = 0.7$ and $\Omega_M = 0.3$ [29], which means that dark energy accounts for 70% of the total mass-energy of the Universe. Consequently, the Universe was expanding less quickly during the epoch that generated cosmological ν's leading to a proportionally larger contribution to the neutrino yield from higher redshifts. Engel et al. [19] compared the neutrino fluxes derived from the two cosmological models and found that the $\Omega_\Lambda = 0.7$ model increases the neutrino flux by 60% for a moderate redshift evolution.

4. Cosmological evolution

Predictions of neutrino fluxes are strongly dependent on the cosmological evolution of the potential cosmic ray sources. There are at least four evolution models that have been most commonly discussed in the literature, namely:

i. No evolution,

ii. Star Formation Rate (SFR),

iii. Active Galactic Nuclei-FRII (FRII) and

iv. Strong Gamma Ray Burst (GRB).

When describing the cosmological evolution of sources, a source evolution term $\mathcal{H}(z)$ is used to specify evolution of mass (or rate) density of sources with redshift z within a comoving volume. It represents the ratio of the mass density of sources between redshift z and now. The mass density of sources at redshift of z would be $\rho(z) = \mathcal{H}(z) \times \rho(0)$.

i. No evolution: The simplest model assumes that there is no evolution with redshift (i.e. $\mathcal{H}(z) = 1$) and it yields the most conservative neutrino flux.

ii. SFR: This model was first introduced in [30] and then studied in more detail in [31]. They use data from different experiments measuring the number of sources as a function of redshift to infer when were the stars formed. In this model, the density of sources first increases, then remains constant or with a small decrease and, finally, there is a cutoff. As an example we show the parametrization given in [31]:

$$\mathcal{H}(z) \propto \begin{cases} (1+z)^{3.4} & z < 1, \\ (1+z)^{-0.3} & 1 < z < 4.5 \\ (1+z)^{-8} & z > 4.5 \end{cases}$$

iii. FRII: Radio galaxies are a kind of active galaxy very luminous at radio wavelengths. One way of classifying these galaxies is by the morphology of the large-scale radio emission. FRI galaxies typically have bright jets in the centre, while FRIIs have faint jets but bright hotspots at the ends of the lobes. FRI are far from satisfying the energetic criteria to accelerate particles to the highest energies [32]. FRIIs appear to be able to transport energy efficiently to the ends of the lobes, although it is worth mentioning that no outstanding correlation has been observed between catalogues of FRII galaxies and the most energetic events seen by the Pierre Auger Collaboration. The distribution of these sources as a function of redshift is described in [33]. In order to compare with SFR we present here a simple approximation to the distribution: increasing faster than in the case of SFR ($(1+z)^4$) until redshifts of 2 and then decreasing as $\exp\left[(2-z)/1.5\right]$ [3]. The effect of this kind of source evolution on the expected neutrino flux is studied in [22] and the result is an enhancement of the flux in a factor 7 with respect to the SFR.

iv. GRB: The latest Swift observations indicate that the GRB rate departs from the SFR rate at the highest redshifts ($z > 4$) [34]. However, the difference in the expected neutrino fluxes between SFR and GRB is very small because the contribution of sources at redshifts $z > 4$ is less than 1% to the total flux due to the redshift dilution.

[3] The parametrization used in [22] is $2.7z + 1.45z^2 + 0.18z^3 - 0.01z^4$.

5. Proton-photon cross-section

The neutrino yield from the interaction:

$$p\gamma \rightarrow \Delta^{+} \rightarrow n + \pi^{+} \rightarrow n + \bar{\nu}_{\mu} + e^{+} + \nu_{e} + \nu_{\mu} \tag{1.4}$$

is determined by the proton-photon cross-section, $\sigma_{p\gamma}$. Cross-section measurements from accelerator data are used to estimate the fraction of energy going into neutrinos and the number of neutrinos produced in one interaction. Generally, it is assumed that the fraction of energy going into the charged pion from the proton is on average $x_{p\rightarrow\pi} \approx 0.2$ and that the four leptons carry an equal amount of energy, so on average each neutrino carries about 1/20 of the proton energy. The energy carried by a neutrino in a neutron decay is only $\sim 3 \times 10^{-4}$ times the energy of the origina proton [35].

6. Neutrino oscillations

In the decay of a pion the ratio of muon neutrinos to electron neutrinos is about 2. In this work, unless stated otherwise, muon neutrinos (ν_{μ}) refer to $\nu_{\mu} + \bar{\nu}_{\mu}$, and the same applies for electron neutrinos (ν_{e}) and tau neutrinos (ν_{τ}). Due to the fact than neutrino oscillate, original cosmic neutrino fluxes with a $\nu_{e} : \nu_{\mu} : \nu_{\tau}$ ratio at the source of 1:2:0 oscillate to a ratio of 1:1:1.

Though the existence of cosmogenic neutrinos is very likely, flux predictions span four orders of magnitude. Some of these predictions are shown in Fig. 1.3 for the total neutrino flux summed over all three flavors.

1.2.2 Active Galactic Nuclei and Gamma Ray Bursts

Active Galactic Nuclei (AGN) are the most persistent objects isotropically distributed in the sky and one of the most powerful source classes with luminosities on the order of $10^{45\pm3}$ erg/s [36]. Therefore they are considered as one of the best candidate sources for UHE cosmic ray production and many authors predict measurable fluxes of neutrinos if the acceleration site is surrounded by a sufficiently thick cocoon of material.

The enormous radiation from AGNs is thought to be fueled by gravitational energy released as matter infalls onto a supermassive black hole at its center. During this process, angular momentum causes the material to flatten into an accretion disk. Infalling matter is diverted into a perpendicular oriented jet, with turbulent shocks accelerating particles to high energies. Thereby, a significant fraction of gravitational energy is converted into highly relativistic particles via first-order Fermi acceleration [37] of charged particles. Frictional heating turns the infalling matter into plasma, which thereby produces a strong magnetic field. The collisions of ultra-relativistic protons with the intense photon fields of AGN yield high energy

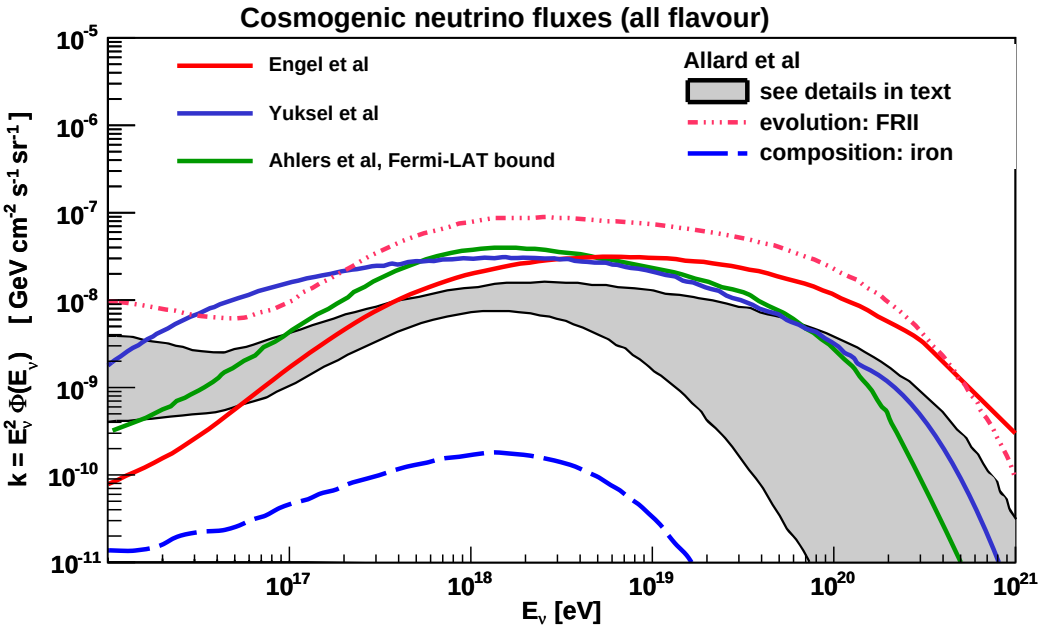

Figure 1.3 Cosmogenic neutrino fluxes (all flavour): In all cases the cosmological model used considers $\Omega_M = 0.3$ and $\Omega_\Lambda = 0.7$. In red a standard GZK flux with pure proton composition and an index $\alpha = 2$ and $E_c = 10^{21.5}$ eV for the spectrum [19]. In solid light blue the GRB model for the cosmological evoultion is used [23]. In solid green a prediction using the measurements of the Fermi-LAT experiment [21]. The shaded area is obtained from Ref. [22], bracketing a wide range a parameters: several source evolution models (not including uniform and FRII), for pure protons and a mixed Galactic composition. Including the uniform source evolution would lower the prediction by almost an order of magnitude. The pink dot-dashed line corresponds to an optimistic scenario with a FRII strong source evolution case with a pure proton composition, and $E_c = 10^{21.5}$ eV [22]. The blue dashed lineis an extreme pessimistic scenario with pure iron composition and uniform evolution [22].

neutrinos through photopion production via $p\gamma \rightarrow \pi^+ + n$ and subsequent decay of $\pi^+ \rightarrow \mu^+ + \nu_\mu$ followed by $\mu^+ \rightarrow e^+ + \nu_e + \bar{\nu_\mu}$.

Other models imagine that protons collide with gas and dust, so the mechanism is $pp \rightarrow \pi\mathrm{s} + X$. As in the GZK mechanism, the neutrinos initially include only ν_μ and ν_e, but oscillation turns them into equal flavor ratios on their way to Earth.

Depending on where neutrino production takes place, there are two classifications: AGN core model or AGN jet model. In the first one, initially proposed by Stecker et al [14], protons are accelerated and interact with the photon field inside the cores of AGNs. In the second model, there are two relativistic jets that are emitted perpendicular to the accretion disk, which transport matter in the form of lobes. Protons are accelerated at shock waves in the jets and then, upon interacting with photons radiated from the accretion disk, produce neutrinos. The neutrino flux can be estimated using the measured luminosity and by integrating over redshift and

luminosity [38]. Mannheim et al. [39] calculated the maximum possible neutrino flux originating from AGNs using source evolution functions for blazars and varying the energy where the cosmic ray spectrum changes its slope.

Gamma Ray Bursts (GRBs) are brief flashes of γ-ray emitted by sources at cosmological distances. They are the most energetic explosions in the Universe and are thought to be possible sources of high energy neutrinos. Their neutrino emissions have been calculated under various scenarios.

In the currently favored GRB fireball shock model [42,43], the prompt γ rays are produced by collisions of plasma material moving relativistically along a jet (internal shocks), i.e. a fireball. Late time collisions of jetted material with an external medium, like interstellar medium (external shocks), produce a broad band radiation like X-ray, UV and optical radiation, collectively known as the GRB afterglow. In the jet, electrons and protons are accelerated by relativistic shocks via Fermi mechanism. The synchrotron radiation and inverse Compton scattering by the high energy electrons lead to the observed prompt photons. The accelerated protons on the other hand interact with observed prompt γ-rays or afterglow photons via photopion production interaction, and produce a burst of high energy neutrinos accompanying the GRB. The neutrinos generated in the original fireball with internal shock are called burst neutrinos, and those from GRB external shock are called afterglow neutrinos.

Another popular GRB model is the supernova model [44] in which a supernova remnant shell from the progenitor star is ejected prior to the GRB burst. Protons in the supernova remnant shell and photons entrapped from a supernova explosion or a pulsar wind from a fast-rotating neutron star remnant provide ample targets for protons accelerated in the internal shocks of the gamma-ray burst to interact and produce high energy neutrinos.

In Figure 1.4 we present several neutrino flux predictions from AGNs and GRBs.

1.2.3 Unconventional Neutrino Sources

These models were proposed to explain the apparent lack of a GZK cutoff in the high energy cosmic ray spectrum in early observations. Top-down (TD) models are based on the assumption that both UHECR and neutrinos are the decay products of some super-massive exotic particles (X) with mass $m_X > 10^{20}$ eV and energies all the way up to the grand unified theory scale ($\sim 10^{16}$ GeV $= 10^{25}$ eV). The X particles first decay into quarks and leptons. As the quarks hadronize, jets of hadrons are produced. The decay products of the unstable leptons, together with the jets of hadrons, result in a cascade of energetic photons, neutrinos and light leptons with a small fraction of neutrons and protons, some of which contribute to the observed UHECR. S. Yoshida et al. proposed that the X particles could be

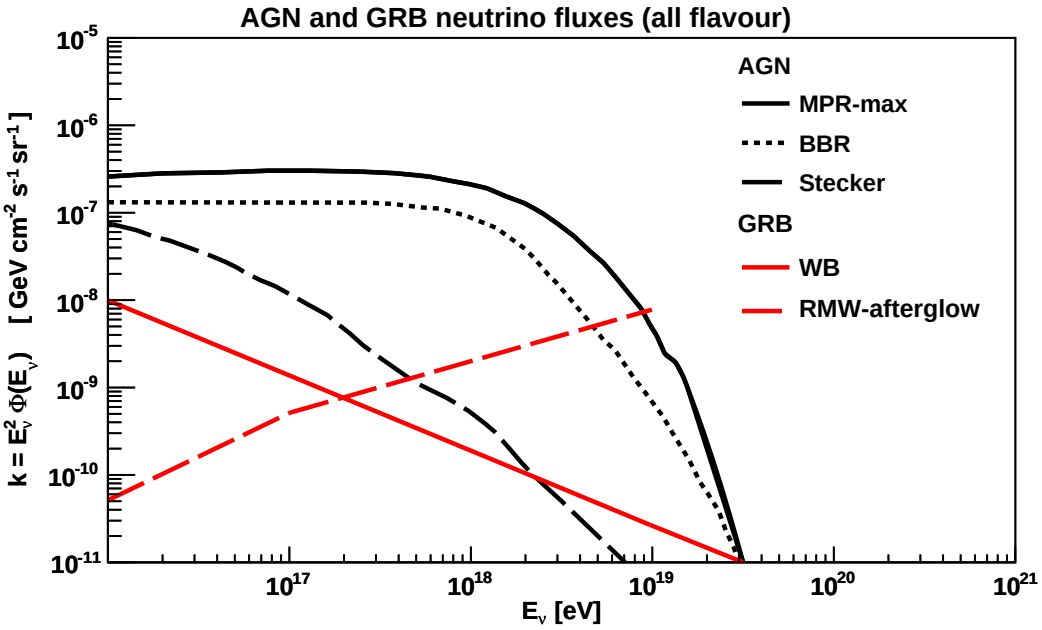

Figure 1.4 Predicted neutrino fluxes from AGNs and GRBs(all flavour): In black we show three different models for AGNs [39–41] and in red two models for GRBs [43, 44].

released from topological defects, such as monopoles and cosmic strings, which were formed in the early universe; and that the UHECR well above 10^{20} eV and UHE neutrinos are the result of the annihilation or collapse of topological defects [16].

The Z-Burst model proposed that neutrinos may not only be cosmological by-products but could also be the sources of UHECR. This model was presented when AGASA reported a flux of particles above 10^{19} eV which was not suppresed by the GZK cutoff. It assumes a large flux of neutrinos at energies of order 10^{22-23} eV. These can annihilate with Big-Bang relic cosmic background neutrinos ($T_\nu \sim 1.9$ K) in our own Galactic halo via the interaction as: $\nu + \bar{\nu} \rightarrow Z_0$ [17]. The decays of the neutral weak vector boson Z_0 yields UHECRs, while the high energy neutrinos that do not interact could be detected at the Earth.

In Figure 1.5 we present neutrino flux predictions from these two unconventional neutrino sources.

1.2.4 Theoretical limits on Neutrino Flux

E. Waxman and J. Bahcall in Ref. [46] established theoretical bounds on the flux of neutrinos produced by photopion interactions of protons.

They considered that the observed cosmic ray spectrum is consistent with that expected for a cosmological distribution of sources of protons, with injection spectrum $dN_{CR}/dE_{CR} \propto E_{CR}^{-2}$, as typically expected for Fermi acceleration [47]. If the

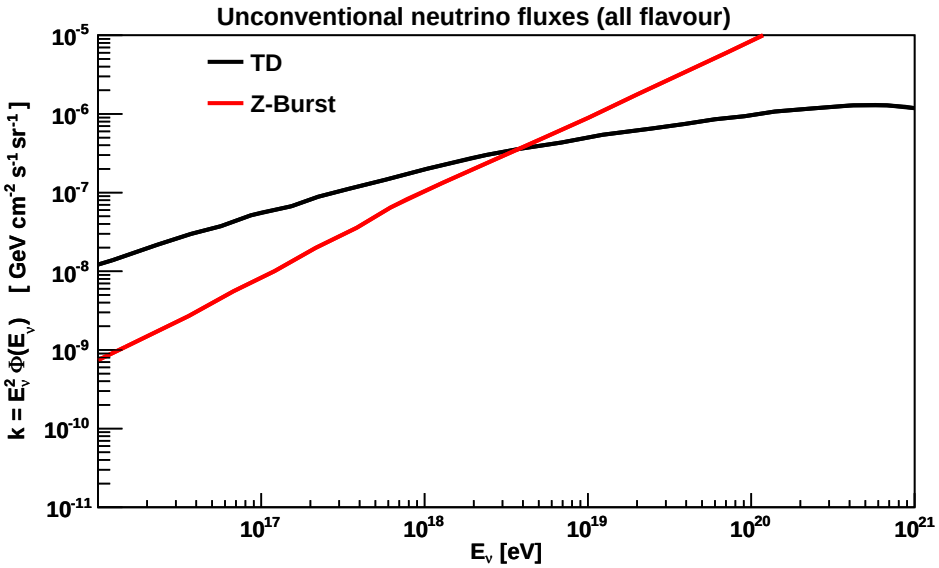

Figure 1.5 Neutrino fluxes from unconventional sources (all flavour): A model considering a super-massive ($m_X \geq 2 \times 10^{23}$ eV) exotic particle decay and a Z-burst model [45].

high-energy protons produced by the extra-galactic sources lose a fraction $\epsilon < 1$ of their energy through photo-meson production of pions before escaping the source, for energy independent ϵ the resulting present-day energy density of muon neutrinos follows the proton generation spectrum. Assuming that all the energy injected as high-energy protons is converted to pions via photopion or p-p collision, the energy generation rate of neutrinos cannot exceed the energy generation rate of protons at the sources. Using this energy-dependent generation rate of cosmic-rays they derived a characteristic E^{-2} spectrum bound on the muon neutrino flux (ν_μ and $\bar{\nu_\mu}$ combined) for the cosmological model of no redshift evolution and for a Quasi Stellar Objects cosmological model. To get an upper bound on the total neutrino flux, the muon neutrino intensities are multiplied by 1.5 due to the ratio of $\nu_e : \nu_\mu : \nu_\tau = 1 : 2 : 0$ at the origin.

It is important to emphasize that the calculations produce an upper bound. There are no lower bounds in the literature.

1.3 Experimental searches

We review[4] some current and upcoming experiments that are involved in searches for UHE neutrinos of cosmic origin. The detection techniques rely on Cherenkov radiation, either in optical or radio for the very highest energies. Acoustic detectors

[4]Many extensive reviews and status reports appear in the literature. Ref [48] provide concise summary of astrophysical neutrino searches.

sensitive to the sudden local expansion that occurs when a high-energy neutrino interaction deposits energy in water or ice are also methods being considered.

1.3.1 Optical Methods

Particle tracks from the products of the neutrino interaction in a dense medium can create visible Cherenkov radiation than can be picked up by photomultiplier tubes. Lake Baikal in Siberia is host to NT-200 [49], one of the pioneering experiments searching for neutrino detection using phototubes.

The largest of such experimental searches is IceCube, the successor to AMANDA (Antarctic Muon And Neutrino Detector Array). It consists of thousands of spherical optical sensors buried in the South Pole ice between 1450 m and 2450 m depth, spreading over an instrumented volume of ~ 1 km^3. The main goal is to detect neutrinos of energies spanning from 10^{11} eV to about 10^{20} eV through the Cherenkov light given off by the muons produced through a charged-current interaction of a muon-neutrino with nucleons in the ice. Construction was completed in early 2011 and recent data are helping further constrain the astrophysical neutrino flux over different energy regimes. The latest published results on extremely-high energy diffuse neutrino searches with data collected between April 2008 and May 2009 (333.5 days of livetime) from the half-completed array places a limit of

$$E^2\phi_\nu \leq 3.6 \times 10^{-8}\,\mathrm{GeV\,cm^{-2}\,s^{-1}\,sr^{-1}} \tag{1.5}$$

over the energies of 2×10^{15} eV to 6.3×10^{18} eV. In this energy region, this result is the first constraint of neutrino fluxes below the Waxman-Bahcall flux bound [50].

Another very recent and spectacular result by IceCube is the discovery of two $\sim$1 PeV neutrinos, the highest neutrino energies observed so far, using data corresponding to 615.9 days effective livetime [51]. The probability to observe two or more candidate events under the atmospheric background hypothesis is 2.9×10^{-3} (2.8σ).

ANTARES [52] (off the coast of Southern France), NEMO [53] (near Sicily) and NESTOR [54] (15 km from the Greek coast), are all experiments using the same technique as IceCube but with the optical sensors spread over the Mediterranean Sea. These experiments complement IceCube by observing the Northern sky but the instrumented volume is smaller than in IceCube so they cannot reach high exposures at high energies. KM3NeT [55] is a future experiment with an instrumented volume of ~ 1 km^3 which will also be placed in the Mediterranean Sea.

1.3.2 Radio Cherenkov

At EeV (10^{18} eV) energies and above, the expected neutrino flux is too small to be detectable in km^3 telescopes. Radio detection in the MHz to GHz frequency range presents a viable way to probe the UHE range in a cost-effective way and has

been proposed as an avenue for neutrino detection by Gurgen Askaryan in the early 1960's [57] [56]. He realized that the coherence of the Cherenkov radiation in the radio regime results in the power of the pulse being proportional to the square of the primary of energy of the initial particle. Coupled with the fact that the attenuation lengths in naturally occurring media like ice, salt and sand is very long (hundreds of meters) at such frequencies (1 GHz), it is promising to instrument large volume of such media to listen to RF pulses. All the past, present and proposed radio Cherenkov experiments use one of these three media.

RICE (the Radio Ice Cherenkov Experiment) searches for radio emission from electromagnetic and hadronic cascades induced by UHE neutrinos colliding with nuclei in the Antarctic ice. It is an array of 16 antennas of bandwidth 200-1000 MHz contained within a cube of ice 200 m on a side, with a center about 150 m deep, near the South Pole. Based on data collected from 1999 to 2005, with a livetime of 74.1×10^6 s, RICE placed a 95% CL model-dependent limits on the neutrino flux of all flavors of

$$E^2\phi_\nu \leq 10^{-6}\,\mathrm{GeV\,cm^{-2}\,s^{-1}\,sr^{-1}} \tag{1.6}$$

over the energy regime of 10^{17} eV to 10^{20} eV [57], after no neutrino candidate events were found. For similar comparison with other flux limits, we scale the limit to 90% C.L. in Figure 1.6.

ANITA (ANtarctic Impulsive Transient Array) is an Antarctic balloon-borne experiment that is launched under NASA's balloon program from the McMurdo station. It consists of an array of broadband (200-1200 MHz) dual-polarization quadridged horn antennas that observes the Antarctic ice sheet from its in-flight altitude of 37 km. The first full ANITA flight, following the ANITA-LITE prototype test flight in early 2004, was launched on December 2006 and remained aloft above Antartica for 35 days [58].

The second flight, with a payload enhanced from 32 to 40 antennas and other hardware improvement, was in December 2008. From 28.5 days livetime and using one observed candidates, ANITA-II set a 90% CL integral flux limit on all neutrino flavors of

$$E^2\phi_\nu \leq 1.3 \times 10^{-7}\,\mathrm{GeV\,cm^{-2}\,s^{-1}\,sr^{-1}} \tag{1.7}$$

the strongest constraint to date over the energy range 10^{18} eV to $10^{23.5}$ eV [59].

GLUE (Goldstone Lunar Ultrahigh Energy) searched for ∼10 ns microwave pulses from the lunar soil, appearing in coincidence at two large radio telescopes separated by about 20 km and linked by optical fiber. The pulses can arise from subsurface electromagnetic cascades induced by interactions of up-going UHE neutrinos in the lunar regolith. Using data of about 30 hours of livetime which yielded zero events, GLUE sets upper limits on the diffuse cosmic neutrino fluxes over the energy range from 10^{19} eV to $10^{22.5}$ eV [60]. Kalyazin [61] and Parkes [62] experi-

ments have also previously monitored the moon for signals. There are ongoing efforts to exploit either existing radio telescopes like Westerbork Synthesis Radio Telescope through the NuMoon [63], and future giant arrays like the planned Square Kilometer Array (SKA), that is to be located in South Africa or Australia [64]. LUNASKA (Lunar UHE Neutrino Astrophysics using the Square Kilometer Array) is one such proposal, with first preparatory observations taken with the ATCA (Australian Telescope Compact Array) [65].

ARA (Askaryan Radio Array) is an initiative to develop a multi-phased teraton-scale ultra- high energy neutrino detector in deep, radio-transparent ice near the South Pole [66]. A station design consists of a cluster of 16 embedded antennas deployed up to 200 m deep in several vertical boreholes placed with tens-of-meter horizontal spacing to form a small sub-array. An initial prototype detector system was installed in January 2011 to perform studies relating to the radio environment of the site: background noise levels and radio clarity of the ice. There are plans to build a 200 km^2 array, known as ARA-37.

ARIANNA (Antarctic Ross Ice-shelf ANtenna Neutrino Array) [67] aims at using the enormous Ross Ice Shelf near the coast of Antarctica. It is designed to detect UHE neutrinos with energy greater than $10^{17.5}$ eV. The concept emerged following recent studies [68] at the Ross Ice Shelf that confirmed earlier glaciological surveys that found high fidelity radio reflectivity of the ice-water bottom. This would allow for detection of the reflected conical Cherenkov pulses generated by "down-going" neutrinos arriving from the whole southern celestial hemisphere . The advantages are low levels of anthropogenic radio noise in Antarctica, the possibility of long livetime and the scalability to large volumes attainable by covering vast expanses of the area with autonomous radio antenna stations.

SalSA (Salt Sensor Array) is a detector concept to deploy radio detectors in one of the large salt formations (a few $km^2 \times 10$ km are not atypical) that exist in many locations around the world [69]. One would find 2.5 times as many neutrino interactions per unit volume in salt compared to ice due to its higher density. Although the peak power of the emitted radio Cherenkov signal is lower than in ice, the width of the Cherenkov cone is broader [70]. Additionally, an experiment in the Northern Hemisphere would observe a region of the sky not in the field of view of an experiment in the South. Ground Penetrating Radar (GPR) experts have reported low radio loss in salt mines in the US, but it is difficult to deduce attenuation lengths measurements from their findings [71]. Before a SalSA experiment can move forward, long attenuation lengths (250 m) must be measured definitively at radio frequencies.

1.3.3 Cosmic Ray Detectors

We have already introduced three cosmic ray experiments that were involved in the determination of the GZK cutoff. Though designed for UHECR studies, they can be used to observe neutrinos.

AGASA (Akeno Giant Air Shower Array) used a widely spread ground array, consisting of 111 plastic scintillation detectors of 2.2 m^2 over an area of 100 km^2 with a separation of 1 km, to detect UHECR by measuring the secondary particles produced in a cosmic ray shower [5].

The **HiRes** (High Resolution Fly's Eye) experiment consists of two detector stations located 12.6 km apart. Each station monitors its surrounding sky for observing fluorescent emission from cosmic ray air showers in atmosphere [4]. The GZK feature in their measurements has been corroborated by Auger, as seen earlier in Figure 1.1. However, they diverge on other CR observations: no anisotropy in their smaller data sample and light primaries composition persistent up to the higher energies. Regarding neutrino detection, they have reported 90% C.L integrated flux limits $E^2\phi_\nu$ of 3.81×10^{-7} , 9.73×10^{-7} and 4.71×10^{6} GeV cm^{-2} sr^{-1} s^{-1} over three decades energy centered around $10^{18.5}$, $10^{19.5}$ and $10^{20.5}$ respectively. This calculation was based on a livetime of 3638 hours, with no neutrino events, and combining results from ν_τ and ν_e studies [72]. They were sensitive to decays of the outgoing tau's following ν_τ interactions in the Earth's crust and to electromagnetic showers induced by the ν_e also interacting in the Earth's crust [73].

Auger (Pierre Auger Observatory) hybrids both techniques of surface and fluorescence detectors to observe showers simultaneously [74]. It can detect UHE neutrinos by searching for extended inclined air shower from down-going neutrinos of any flavor or up-going tau neutrinos through a distinctive broad signal in time as their signature. In the first case, the neutrino can interact at any atmospheric depth to produce an extensive air shower [75]. Earth skimming UHE ν_τs may undergo a charged-current interaction to produce τs close to the surface, which can exit the Earth and decay in the atmosphere to produce a nearly horizontal electromagnetic shower [76]. Based on the published data taken until May 2010, an upper limit on the diffuse flux of UHE ν_τ is set at 90% C.L. for Earth-skimming neutrinos,

$$E^2\phi_\nu \leq 9.6 \times 10^{-8}\,\mathrm{GeV\,cm^{-2}\,s^{-1}\,sr^{-1}} \tag{1.8}$$

in the energy range 2×10^{17} eV $< E_\nu < 2 \times 10^{19}$ eV [77], and for downward-going neutrinos,

$$E^2\phi_\nu \leq 5.1 \times 10^{-7}\,\mathrm{GeV\,cm^{-2}\,s^{-1}\,sr^{-1}} \tag{1.9}$$

in the energy range 1×10^{17} eV $< E_\nu < 1 \times 10^{19}$ eV [75]. For better comparison with other experiments, we have converted from single flavour to all flavours limits by multiplying by 3.

In Figure 1.6, we summarize the flux limits imposed in the 10^{17} -10^{21} eV energy range.

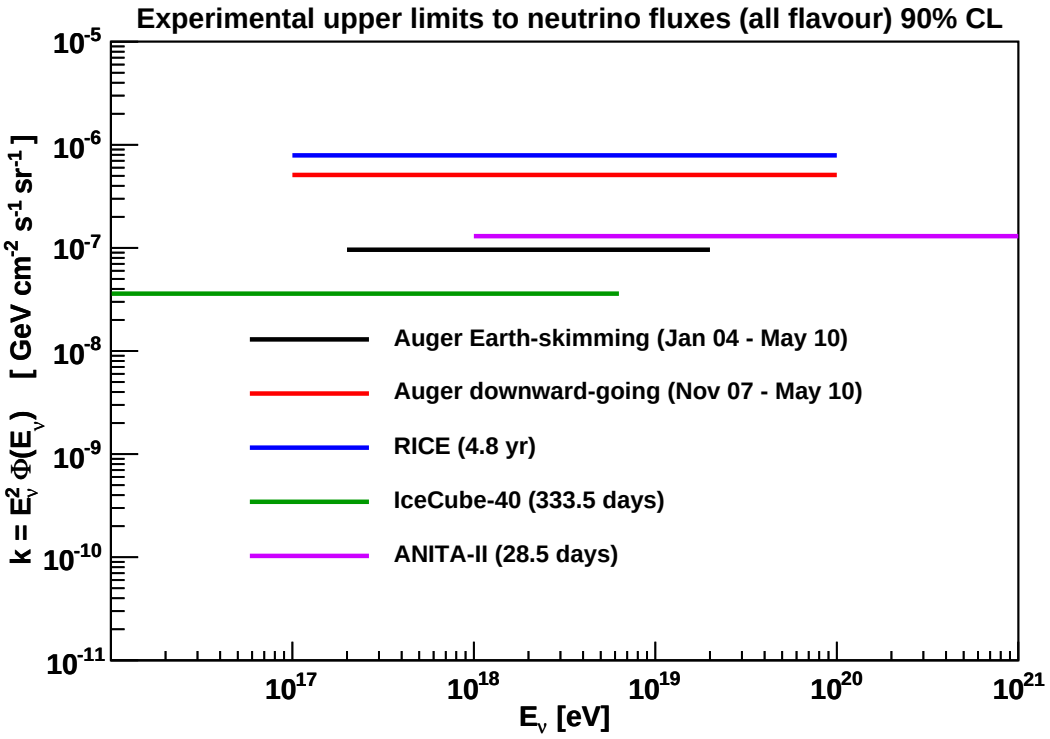

Figure 1.6 Limits for a diffuse neutrino flux of all flavors from the Pierre Auger Observatory [75, 77], RICE [57] (scaled to 90% C.L.), IceCube (IC-40) [50] and ANITA-2 [59]. The IceCube energy range of the integral limit is 2×10^{15} eV to 6.3×10^{18} eV. The ANITA-2 energy range of the integral limit is 10^{18} eV to $10^{23.5}$ eV.

2

Neutrino detection using atmospheric showers

The principle of detection of neutrinos using extended atmospheric showers, EAS, is the subject of this Chapter. Section 2.1 introduces the phenomenon of EAS discussing the differences between vertical and inclined showers. In Section 2.2 we describe the characteristics of showers initiated by neutrinos interacting in the atmosphere and in the Earth crust. In Section 2.3 the detection technique to measure these showers is explained.

2.1 Atmospheric particle showers

At the end of the 30's Pierre Auger observed that the trigger coincidence between cosmic ray detectors which were separated by several kilometers was higher than expected for independent events. He proposed an explanation postulating the existence of very energetic particles which generated new particles when they interacted high in the atmosphere. The first generation of new particles could again interact and produce a further generation, initiating a chain reaction which multiplied the number of particles. The phenomenon is known today as an extended atmopheric shower, EAS.

After 70 years of research, the structure and evolution of particle showers is considered to be well understood. After the first interaction, the development can be described as a set of particles of high energy (usually hadrons), which travel along the axis of the shower producing less energetic electrons, muons and photons that diffuse over the radial direction (see Fig. 2.1). In this way, the EAS are a thin disk of particles which propagates close to the speed of light in a path determined by the direction of the primary particle. This disk, also called front, presents a high

density of particles at the center which diminishes in an exponential way along the radial direction.

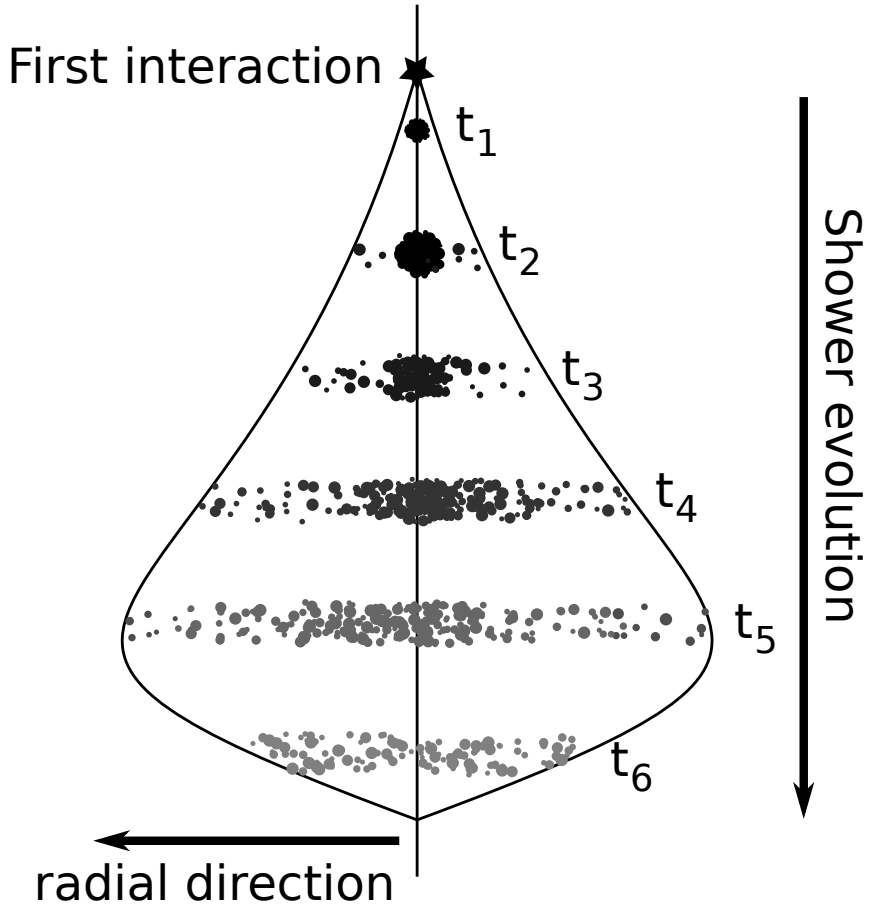

Figure 2.1 Scheme of the evolution of an atmospheric shower. After the first interaction the core of high energy showers is formed (usually hadrons) which moves along the direction of the shower producing new particles less energetic but with higher relative transverse momentum so they diffuse in the radial direction.

Nowadays it is considered that at least 99% of the showers with energies higher than 10^{17}eV are initiated by hadronic ultra high energy cosmic rays, UHECR [78]. These showers can be modeled with 3 components (see Fig. 2.2): hadronic, muonic and electromagnetic (photons and electrons). In the first generations of the shower the number of hadrons increases quickly. In each hadronic interaction, the energy is equally divided among π^+, π^- and π^0. As π^0 promptly decay into two photons, after crossing enough atmosphere, most of the energy carried by π^0 is dissipated through the electromagnetic component producing ionization. The rest of the energy is in the form of muons and neutrinos originated by $\pi^+ \to \mu^+ + \nu_\mu$ and $\pi^- \to \mu^- + \bar{\nu}_\mu$ decays.

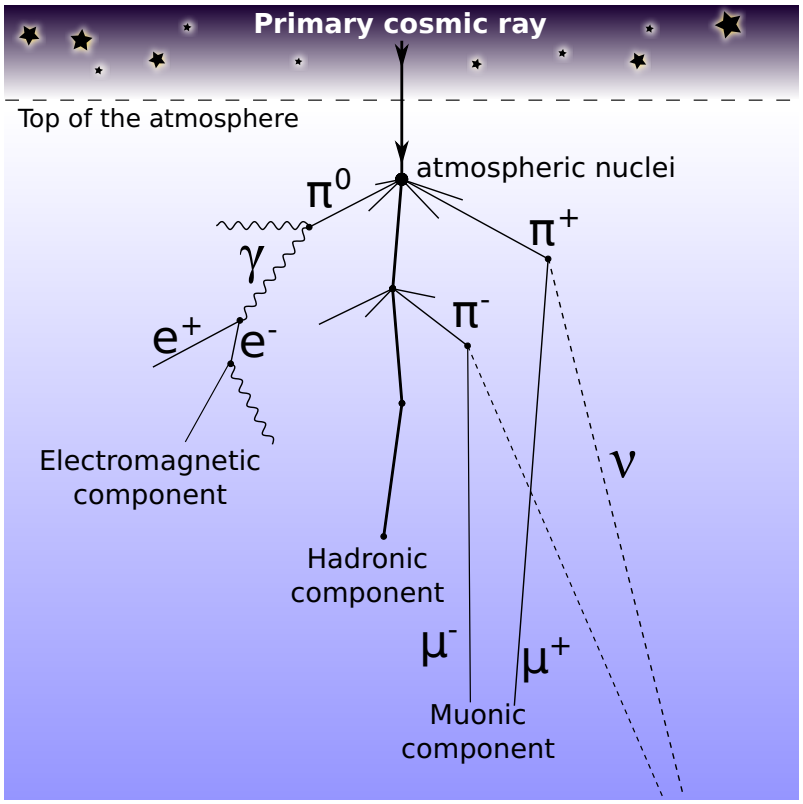

Figure 2.2 Scheme of the structure of an atmospheric cascade.

2.1.1 Model of the evolution of EAS

In this section we present a simplified model of the evolution of atmospheric showers originally developed by Heitler [79] in the middle of the 50's. Even though the model is far too simple to obtain precise results, it is useful to understand the dynamics qualitatively.

The model describes the evolution of the cascades as a discrete process in which the number of particles is multiplied in every generation (see Fig. 2.3). The speed at which a shower develops is determined by an interaction length λ, which depends on the kind of particle involved. Every time a particle interacts, the energy is divided among its children particles.

The hadronic component works as the engine of the shower transferring energy to the muonic and electromagnetic components. High energy photons and electrons interact producing new showers so that the number of EM particles increases quickly. On the contrary, muons are very penetrating particles so one can consider that once they are produced they don't interact and, consequently, do not contribute to the multiplication process.

In a simple version of this model, all the hadrons are pions, $\pi^{\pm}$ and π^0. When they interact they generate new $\pi^{\pm}$ and π^0 in a 2:1 ratio. π^0s decay immediately

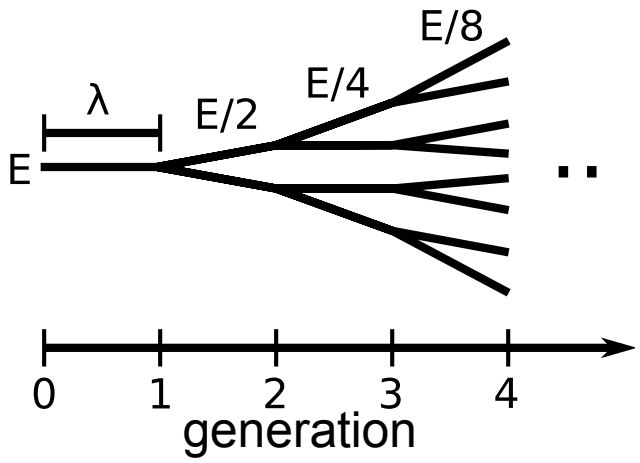

Figure 2.3 Heitler model for the evolution of an atmospheric shower. The interaction length λ defines the distance between generations. In each generation the number of particles is multiplied.

into two photons which feed the electromagnetic component. $\pi^{\pm}$s, having a longer lifetime, continue the hadronic shower until their energy is not enough them to generate new pions. When this happens they decay into muons and neutrinos. The high penetration power of muons allows them to go through the atmosphere without interacting along the path so that they generally reach the surface of the Earth before the electromagnetic component.

2.1.2 Heitler model: electromagnetic shower

If the primary particle is a photon or an electron of high energy the shower is purely electromagnetic. When modelling the evolution one assumes that each electron radiates through bremsstrahlung only one photon after travelling a distance $\lambda \simeq 37$ g cm^{-2} (radiation length in the atmosphere). Every photon produces a pair e^- e^+ after travelling the same distance. In both cases one considers that the energy is divided equally between the children particles. In this way, after n generations the shower has 2^n particles which can be electrons, positrons or photons. The production of new particles stops when the energy lost through ionization dominates over the bremsstrahlung and pair production processes. In air this energy ($E_{\rm cut}$) is around 86 MeV. At this point the number of particles is maximum and one can use the following equations:

$$E_0 = E_{\rm cut} N_{\rm max} = E_{\rm cut} 2^{n_{\rm max}} \tag{2.1}$$

$$X_{\rm max} = n_{\rm max} \lambda \tag{2.2}$$

The shower reaches the maximum number of particles $N_{\rm max}$ at a depth of $X_{\rm max}$ measured in the incident direction of the primary particle. By isolating n_{max} from

equation 2.1 and introducing it in equation 2.2 one obtains the following expresion for $X_{\max}$:

$$X_{\max} = \lambda \log_2 \left(\frac{E_0}{E_{\text{cut}}} \right) \tag{2.3}$$

Even though this model is very simple, this equation is capable of providing a rough estimate of the depth $X_{\max}$. As an example, a 10^{18} eV photon reaches the maximum quantity of particles at a depth of $\sim$ 800 g cm^{-2} [80], and the model predicts $\sim$1200 g cm^{-2}.

2.1.3 Showers produced by protons or nuclei

In a shower initiated by a hadron, typically 80% of the particles produced in the first interaction are pions (the rest being kaons, other mesons and nuclei-antinuclei pairs). Secondary hadrons with enough energy continue the hadronic shower which develops along the shower axis. Low energy mesons decay transferring their energy to the EM and muonic components.

Neutral pions π^0 have a lifetime of 8.4×10^{-17}s so they decay within a short distance[1]. The π^0 decays electromagnetically[2], producing electromagnetic sub-showers identical to the ones described in Sec. 2.1.2. The size of the shower increases until the energy of the electrons drops below the critical energy. At this point of the shower, around 90% of the total energy is in the form of electrons and photons. At lower energies, the losses through inoization overcome bremsstrahlung and the electromagnetic component starts to diminish.

Electrons and positrons suffer multiple scattering which determines the characteristics of the transversal structure of the shower.

Charged mesons have a larger lifetime (2.6×10^{-8}s), so they have a larger probability of interacting with atmopheric nuclei before decaying. The competition between the two processes depends essentially on the balance between the mean free path of the interaction, which depends on the cross-section and the medium density, and the decay length. Both of them vary with the energy and become the same at $\sim$ 115GeV for charged pions and $\sim$ 850GeV for kaons [80].

When kaons and pions decay they produce muons and ν_μ. The cross-section of the interaction of neutrinos is negligible and they escape carrying around $\sim$2% of the primary energy [80]. As the shower evolves, the muonic component increases until reaching a maximum and then decreases very slowly because the decay length is large[3]. Also muons loose energy at a much slower rate than electrons[4].

Showers induced by hadrons have a spatial structure very different from the

[1] The decay length of a GeV (PeV) π^0 is $\sim 0.2\mu$m (0.2m).
[2] The most frequent channel is into 2 photons ($BR = 98.8\%$).
[3] The decay length of a GeV (PeV) μ is $\sim$6km (6×10^6km).
[4] In air $\frac{dE}{dx}$(GeV (PeV)μ) $\sim$ 4(1000)MeVg^{-1}cm^2.

ones initiated by electrons or photons. The latter are more compact due to the fact that the transversal moment p_T of electrons and photons is usually small. On the contrary, deep inelastic scattering (DIS), typical in hadronic showers, usually produces particles with high p_T. Another important difference is that the hadronic showers present a muonic component 100 times more abundant than the observed in an EM shower. The few muons in an EM shower are the result of the decay of pions produced in photonuclear reactions.

2.1.4 Inclined showers

The term "inclined shower" is used, generally, to classify those showers with a zenith angle θ higher than 60°. In order to motivate this definition, it is interesting to study the amount of matter that a shower has to go through to reach the Earth surface as a function of θ. In Fig. 2.4 it can be seen that between 0° and 60° the change is only 1000 g cm^{-2}, a factor of 2 with respect to the vertical depth. At higher zenith angles the atmopheric depth increases quickly and reaches 36000 g cm^{-2} at $\theta = 90°$.

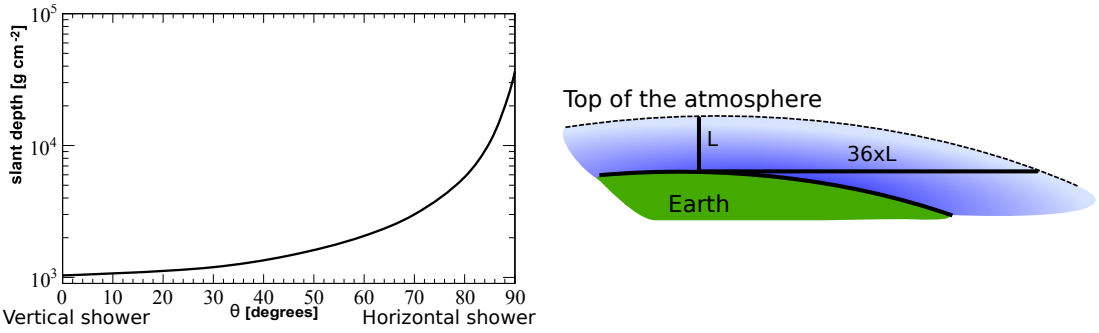

Figure 2.4 *Left:* Atmospheric depth as a function of the zenith angle θ. The amount of matter increases quickly after 60°. *Right:* A horizontal shower goes through 36 times more mass than a vertical shower.

As mentioned before, most of the detected cosmic rays with energies higher than 10^{17} eV are protons or nuclei. The interaction length of these particles is around 50 g cm^{-2}, so the showers are initiated essentially at the top of the atmosphere. Consequently, inclined showers go through an amount of matter much larger that vertical showers and their front arrives at the surface of the Earth much more developed. For this reason inclined showers are usually denominated "old". For $\theta > 70°$ the hadronic and EM components are completely absorbed in the atmosphere while the muonic component reaches the Earth (see Fig. 2.5). The result is that inclined showers are very different than vertical showers, in which the EM component is dominant.

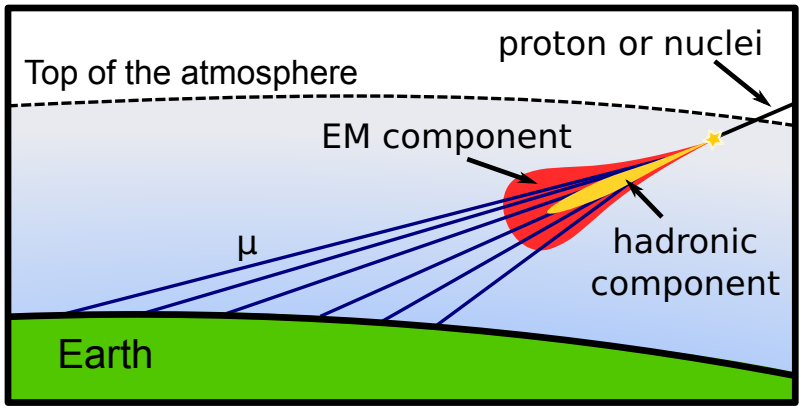

Figure 2.5 Inclined showers produced by protons or nuclei high in the atmosphere. The hadronic and EM components are absorbed and only muons reach the Earth.

2.2 Neutrino showers

2.2.1 Atmospheric neutrino induced showers

Within the Standard Model (SM), the neutrinos interact through the weak force. They also interact through gravity, but in practice, only weak interactions allow to detect individual neutrinos. The primary interaction of the neutrino is DIS. Fig. 2.6 summarizes the weak interaction channels. In all cases around 20% of the energy of the primary neutrino is transferred to the hadronic jet which results from the nucleon debris. These particles initiate cascades very similar to those produced by protons. The remaining 80% of the energy of the primary particle is contained in a ultra-energetic lepton. The actual energy that is transferred to the shower depends on the interaction channel and neutrino flavour.

If the shower is initiated by a ν_e through charged current (CC), the resulting electron initiates an electromagnetic shower overlapping the hadronic one produced by the jet. In this case 100% of the energy is transferred to the shower. On the contrary, neutral current interactions (NC) produce a secondary neutrino instead of an electron. This neutrino escapes and does not contribute to the process of multiplication, carrying around 20% of the energy of the primary neutrino.

Inclined showers initiated by a ν_μ through CC are very similar to the ones initiated via NC even though the fundamental interaction is very different. At 10^{18} eV, the probability that the high energy secondary muon decays before reaching the surface is less than 10^{-6} and it decreases for higher energies [5]. At the same time, the probability of interacting and transferring an important amount of its energy

[5]The Earth radious R is $\sim$ 6000 km and the decay length λ_D of a EeV μ is $\sim 6 \times 10^9$ km so the probability is $P = 1 - \exp(R/\lambda_D) = 1 - \exp(10^{-6}) \sim 10^{-6}$.

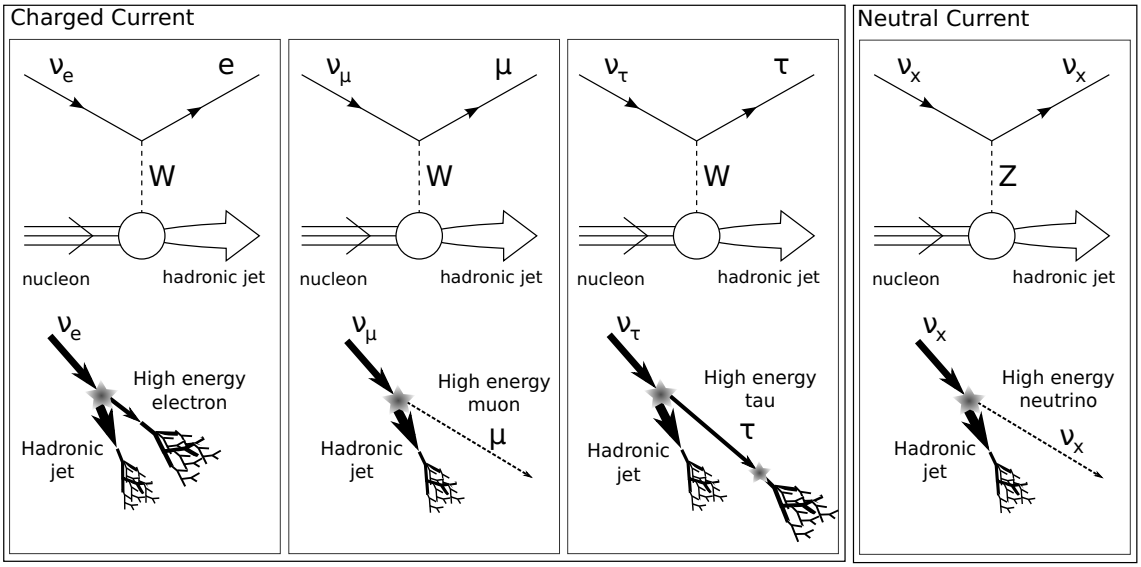

Figure 2.6 Neutrino interaction channels according to the Standard Model. In every case the Feynman diagram is shown at the lowest order. In all channels the emerging jet of the broken nuclei initiate a hadronic shower. The electron produced in the interaction of a ν_e through CC generates also an electromagnetic shower which is added to the hadronic. One ν_τ interacting through CC generates a high energy τ that can travel a distance which depends on its energy and produces a shower closer to the ground.

through bremsstrahlung or DIS is of the order of 10^{-3} [81]. Consequently, it is indistinguishable from a secondary neutrino that emerges from a NC interaction.

The ν_τ via CC presents an interesting characteristic. In the same way as the muon, the τ lepton is a very penetrating particle which can travel an important distance from the point at which it was produced. On the other hand, its lifetime is seven orders of magnitud lower so it can decay before reaching the surface producing a secondary shower that is added to the one initiated by the hadronic jet (see third panel in Fig. 2.6). This kind of showers are commonly known as "Double–Bang" (DB). Depending on the decay channel of the τ, the second shower will be of hadronic or EM nature.

The mean free path for neutrinos of 10^{18} eV is $\sim 10^8$ g cm^{-2} [82]. As this value is much higher than the atmospheric depth, neutrinos can interact at any point in the atmosphere with almost the same probability. In particular, neutrinos can initiate an inclined shower deep in the atmosphere, in which the EM component reaches the surface (see Fig. 2.7). This characteristic distinguishes neutrinos from other possible particles like protons, nuclei or photons which interact in the first hundred grams of the atmosphere with a probability close to 1.

Tau neutrinos can also initiate a deep shower in an indirect way through a high

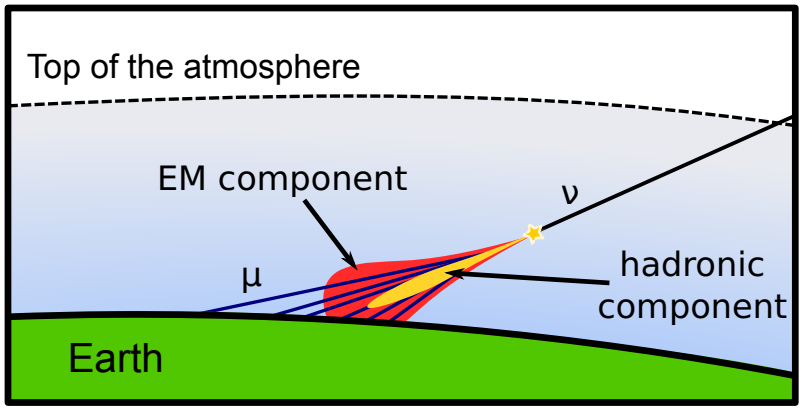

Figure 2.7 Neutrinos can initiate an inclined shower deep in the atmosphere. In this kind of events both the EM and the muonic components reach the surface. Compare to Fig. 2.5.

energy τ produced in the primary interaction. At 10^{18} eV the τ travels on average 50 km before decaying. In this way, even if the primary ν_τ interacts high in the atmosphere, the τ can travel and initiate a deep shower.

The search of deep inclined atmospheric showers is a fundamental method to detect those initiated by neutrinos.

2.2.2 Earth-skimming tau neutrino induced showers

Another very interesting possibility is that the ν_τ interacts in a dense medium like the Earth crust.

We have seen in Chapter 1 that tau neutrinos are suppressed in the neutrino production relative to ν_e and ν_μ, because they are not an end product of the charged pion decay chain. Nevertheless, because of neutrino flavour mixing, the usual 1:2 of ν_e to ν_μ ratio at production is altered to approximately equal fluxes for all flavours after travelling cosmological distances [83]. Soon after the discovery of neutrino oscillations [84] it was shown that ν_τ entering the Earth just below the horizon (Earth-skimming) [85–87] can undergo charged-current interactions, produce τ leptons and, since a τ lepton travels tens of kilometers at EeV energies (the decay length being $\lambda_d = c\tau_\tau\gamma_\tau = 49\text{km}\frac{E_\tau}{\text{EeV}}$), it can emerge into the atmosphere and decay in flight producing a nearly horizontal extensive shower (see Fig. 2.8).

The Earth crust, with a density 1000 times greater than the air density, is a target much more massive than the atmosphere. The mean free path for a 10^{18}eV neutrino in the Earth ($\rho_{Earth} = 2.65\frac{\text{g}}{\text{cm}^3}$) is $\sim$ 620km. Under a spherical Earth approximation the distance the neutrino has to go through is $d = 2R\cos\theta$, where R is the radius of the Earth and θ the zenith angle. This distance is $\sim$220 km at 89°. This means that 30% of these neutrinos should interact at this zenith angle.

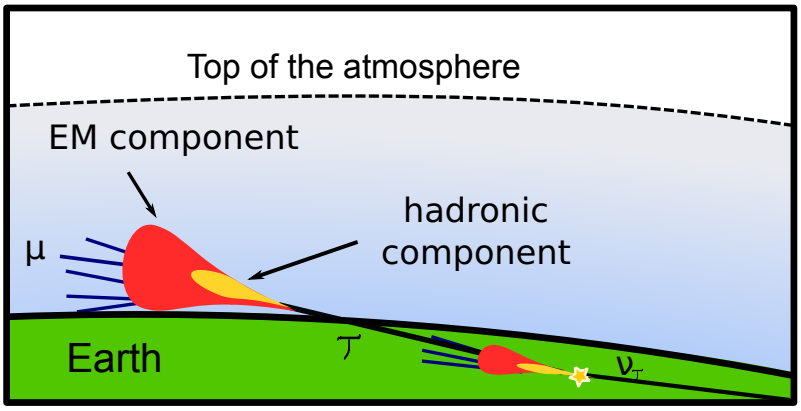

Figure 2.8 A ν_τ can interact in the Earth via charged current interactions and the resulting τ can emerge into the atmosphere and decay. The τ decay products can initiate a quasi horizontal shower which, although having an up-going direction, produces particles that reach the ground.

However, one needs also to consider the probability of the resulting τ escaping the Earth and decaying not very high in the atmosphere. We will analize this in detail in Section 4.1.

The main problem in going to higher zenith angles is that the showers are less horizontal (up-going) so few particles reach a ground detector. We show how the trigger efficiency decreases at higher zenith angles in Section 7.1.1.

The Earth-skimming channel only applies to ν_τs. The detection of electron neutrinos when interacting in the Earth is very suppressed as the resulting high energy electron will give rise to a shower in the Earth. The problem with muon neutrinos is that muons have a lifetime 7.5×10^6 longer than taus so even if they can escape the Earth they decay very high in the atmosphere and the particles from this upgoing shower never reach the ground.

2.3 Detection techniques

2.3.1 Surface detector methods

As the high energy CR flux is extremly low [6] it is necessary to use detectors with an area of several km^2 to obtain an amount of data statistically significant.

The classic way of dealing with the problem is distributing the particle detectors (stations) over a large surface. In this way it is possible to sample the secondary particles at different points of the shower front. This technique was used by P. Auger and his collaborators when discovering the EAS. In this method, the atmospheric

[6] Inferior to one particle per km^2 per year.

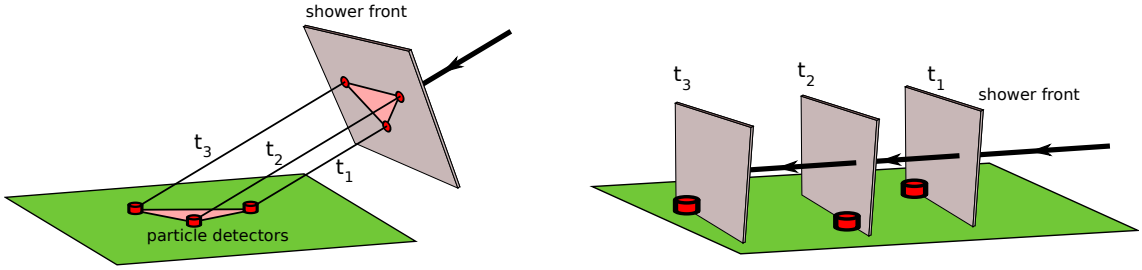

Figure 2.9 Arrival direction reconstruction scheme using a surface detector array. *Left:* Down-going shower. *Right:* Quasi-horizontal shower.

showers are identified when detecting particles in coincidence between two or more stations within a time window determined by the distance between them. If the shower front is registered by three or more non-aligned stations, the direction of the primary particle can be reconstructed from the relative time between the stations (see left panel of Fig. 2.9). The arrival direction resolution is limited by the time resolution of the stations. When the shower is quasi-horizontal the time difference between the stations is given by the distance between stations projected along the direction of the shower, which moves at the speed of light.

The stations composing the surface array can be of different kinds depending on the charateristics of the shower one wants to measure. Nowadays the most common are scintillators and water Cherenkov detectors. Scintillators are generally flat surfaces which register particles that go through them. In this way, they allow to measure the particles density by unit of area. In most of the atmospheric showers, the amount of photons and electrons is very superior to the other particles. For this reason scintillators, if not shielded, are less sensitive to the muonic component. Telescope Array, Yakutsk and AGASA are examples of experiments which chose these kind of detectors [88–90].

Water Cherenkov detectors were developed by the Haverah Park experiment in the middle of the 60's [91]. These are water tanks that contain inside one or more sensors which register the Cherenkov radiation produced by the relativistic particles when they propagate through the water. One of the advantages of these detectors is that, being bulky, they are sensitive to particle fluxes very inclined or even horizontal. A detailed description of this kind of detector is given in the next chapter.

3

The Pierre Auger Observatory

The Pierre Auger Observatory is a hybrid observatory in the sense that it uses two independent detectors to study the most energetic cosmic rays. The first one is a surface detector, deployed over an area of $\sim 3000\,\mathrm{km}^2$. The second one is a fluorescense detector which is capable of observing the development of the showers along their path through the atmosphere before reaching the surface detector.

In this chapter a brief description of the surface detector is presented putting emphasis on the relevant aspects for the neutrino search studies. A detailed description can be found in [92].

3.1 Surface Detector

The surface detector (SD) is composed by 1600 water Cherenkov stations which are set in a triangular array with a separation of 1500 m (see Fig. 3.1). Each of these detectors is sensible to the muonic, electronic and photonic components of a shower. Water Cherenkov detectors were chosen by the Pierre Auger Observatory instead of scintillators because the stopping power of the first ones is higher and the electrons are fully stopped leaving all its energy in the detector. This enhances the posibility of identifying the primary composition [93]. Moreover, the experience of the Haverah Park [91] experiment showed that this kind of detector can work properly for 20 years, which is the programmed duration of the Observatory.

Each station is a cylinder of 1.2 m high and 3.57 m of diameter (see Fig. 3.2), which contains approximately $12\,\mathrm{m}^3$ of ultra pure water. The interior walls are covered by a material called Tyvec which reflects the Cherenkov light with very high efficiency but in a diffuse way so that the dependence of the signal with the direction of the incoming particles is reduced. The Cherenkov light is collected

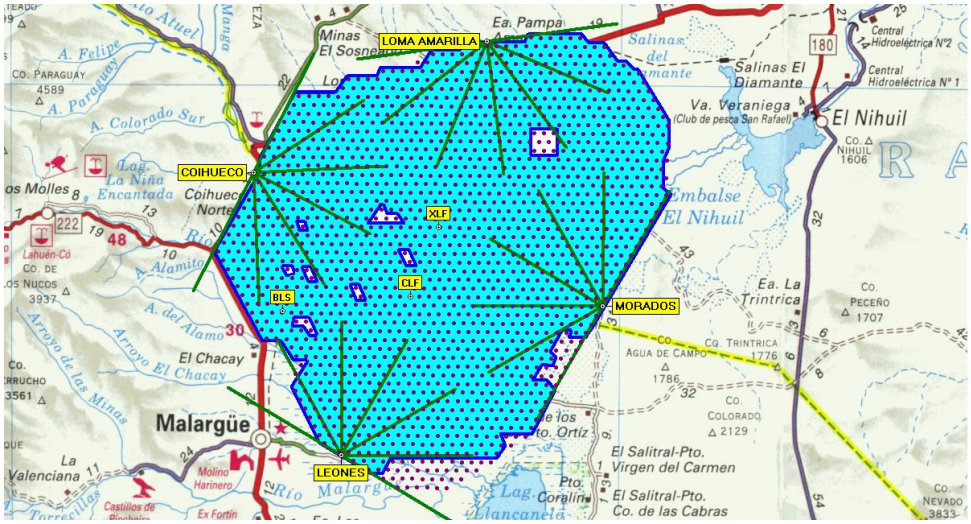

Figure 3.1 Schematic map of the Pierre Auger Observatory. The stations working on June 11 2008 are marked in light blue.

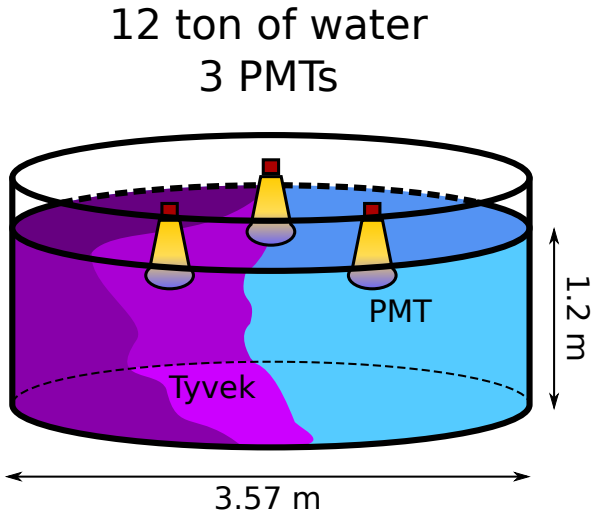

Figure 3.2 Geometry and dimensions of one of the surface stations. They are filled with 10 m^3 of ultra pure water which is overlooked by 3 photomultipliers. The Tyvec covered walls reflect the Cherenkov light until it reaches one of the photomultipliers.

by three 9 inches photomultipliers, whose signal is continuously digitilized with a 40 MHz sampling frequency and a 10 bits resolution. The base of each PMT has two outputs connected to the last anode and to the dynode. The dynode signal is additionally amplified by a factor of 32. When the dynode is saturated the anode signal is used.

As the stations are spread over an area of $\sim 3000\,km^2$ the stations need to be autonomous units so every one is equipped with a solar panel which feeds a battery (see Fig. 3.3). Furthermore, each station is equipped with a GPS which allows to

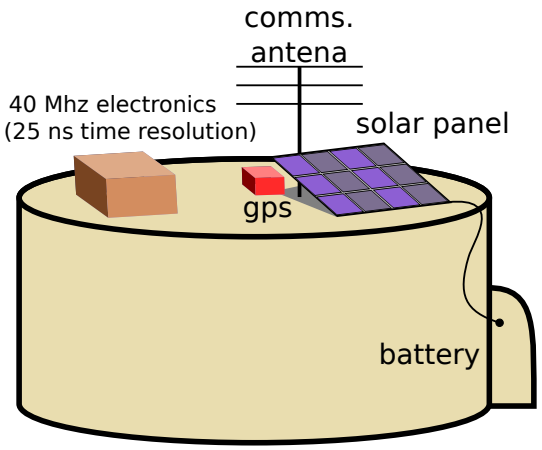

Figure 3.3 Autonomous stations need a solar panel, a GPS and a communication antenna.

synchronize the clocks between stations with a precision of 8 ns [94]. The signal acquired by the phototubes and the timing are kept in memory until it is sent to the Central Data Acquisition System (CDAS) using the communication antenna.

3.1.1 Surface detector calibration

The signal calibration of the SD stations is documented in full detail in Ref. [95], which is the basis of the following summary.

The calibration of each detector is performed locally and automatically because the total bandwidth available for data transmission from the detectors to the CDAS is 1200 bits per second, which precludes the possibility of any remote calibration. In addition, calibration histograms are transmitted to the central control with each event for offline testing of the online calibration.

Cherenkov pulses generated by charged particles within the water volume show exponential decays with a typical decay time of 60 ns. The integral and the height of the pulse above the baseline are proportional to the Cherenkov light generated by the particle. The pulse integral Q is equivalent to the charge collected and the pulse height I to the peak current at the PMT.

The average values of Q and I generated by identical particles vary from station to station and from PMT to PMT. The same is true for their ratio. Each PMT has slight differences in its amplification properties and its optical coupling to the water. Each station has slight variations in the quality of the water and the liner reflectivity.

The trigger sensitivity of individual SD stations and the analysis of SD data should not be dependent on such individual and varying properties. Therefore, the

SD stations continuously perform a self-calibration. Nature provides an excellent calibration source: a uniform background flux of atmospheric muons is constantly generated by cosmic rays of a few GeV, which produces a high rate of muon hits of roughly 2.5 kHz in each station.

This flux can be used to express both Q and I in terms of a physical reference: the vertical equivalent muon (VEM). A VEM has a corresponding pulse height I_{VEM} and charge Q_{VEM}, which are used as base units for I and Q. Signals and trigger thresholds expressed in VEM are independent of individual station or PMT characteristics.

A single station cannot measure the directions or impact points of individual background muons. However the distribution of the light of atmospheric muons gives a peak on both the charge distribution Q^{peak}_{VEM} and the pulse height I^{peak}_{VEM} (see Figure 3.4) which are proportional to those produced by a vertical muon. The second peak produced by the response of atmospheric muons is clearly visible, while the first peak is caused by the combination of the trigger on a steeply falling distribution from low energy particles. The dashed histogram is produced in a reference station with an external muon telescope providing the trigger to select only vertical and central muons. The shift observed is caused by the convolution of photo-electron statistics on an asymmetric peak in the track length distribution. The Q^{peak}_{VEM} is at approximately 1.09 VEM.

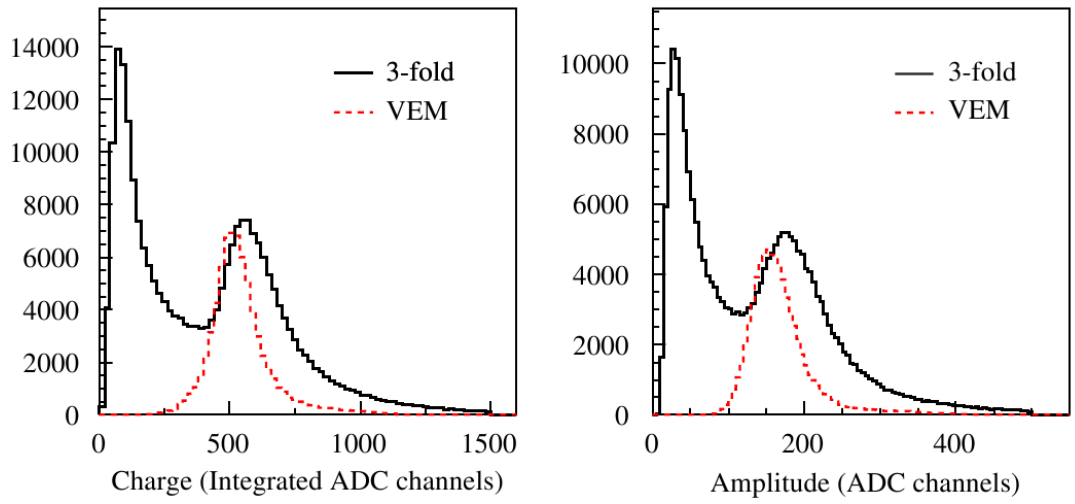

Figure 3.4 Charge and pulse height histograms from a SD station triggered with a 3-fold coincidence between the three PMTs at a trigger level of five channels ($\sim 0.1 I^{peak}_{VEM}$ in each PMT) above the baseline. The signal is summed for the three PMTs. In the solid histogram the second peak is due to the vertical through-going atmospheric muons (VEMs), while the first peak is a trigger artifact. The dashed histogram is produced by vertical and central muons selected with an external muon telescope in a reference station.

The SD calibration procedure can be summarized in three main steps:

1. **Initial set up:** When a local station electronics is turned on, the high voltage of each PMT is adjusted until the rate is 100 Hz for a trigger of 150 channels above baseline. 100 Hz corresponds to approximately $3I_{VEM}^{peak}$, as determined with the reference station. This means that each PMT is set so that 50 channels are equivalent to I_{VEM}^{peak}.

2. **Online calibration:** Once the high voltage of the 3 PMTs are set up, there will be drifts from the initial settings. The PMT high voltage is not changed during normal operation. Instead, the compensation is done via adjusting the trigger levels. The main purpose of this rate-based calibration is to retain a uniform trigger performance over the whole SD array.

   The trigger requirement is set so that the rate is 70Hz. If it is higher (lower) the trigger channel is increased (decreased) until converging. A signal rate of 70Hz corresponds to $1.75I_{VEM}^{est}$, where I_{VEM}^{est} is the estimation of the peak position.

   A comparison of the I_{VEM}^{est} with the peak in the real pulse height histogram, I_{VEM}^{peak}, gives $I_{VEM}^{est} = (0.94 \pm 0.06)I_{VEM}^{peak}$. In order to monitor the status of the detector the procedure also calculates Q_{VEM}^{est} computing the charge of pulses with exactly I_{VEM}^{est}. A comparison of Q_{VEM}^{est} with the peak in the charge histogram, Q_{VEM}^{peak}, yields $Q_{VEM}^{est} = (0.96 \pm 0.03)Q_{VEM}^{peak}$.

3. **Offline calibration:** The SD electronics has a separate trigger designed for collecting high-rate data at a lower threshold ($0.1I_{VEM}^{est}$). A set of histograms is created every minute with approximately 150000 entries per histogram. These histograms are sent to the central control along with any events that are requested. Therefore, each event has high-statistics of charge and pulse histograms from the previous minute accompanying the data.

   The histograms created every minute are:

   - Charge histograms for individual PMT.
   - Charge histograms for the sum of all 3 PMTs.
   - Pulse height histograms for each PMT.
   - Histogram of the baseline of each FADC channel.

   The signals used in the event analysis are based on the calibrated magnitudes: $\frac{Q}{Q_{VEM}^{peak}}$ and $\frac{I}{I_{VEM}^{peak}}$.

3.1.2 Trigger system and data aqcuisition

The trigger system of the surface detector is documented in Ref. [96]. Given the limitations on the quantity of data that the stations can save and that the communication between them and the CDAS is slow, it is necessary that a station be capable of imposing a first level trigger over the signals that are continuously generated due to the atmospheric muons. At the same time, the trigger system has to be efficient in a wide range of energies and zenith angles. The Pierre Auger Collaboration has adopted a hierarchical trigger structure for the surface detector. The system has three levels, however the procedure can be divided into two steps (see Fig. 3.5):

1. Station: trigger conditions imposed in real time for each station (T1 y T2).

2. Detector: analysis of the distribution of the triggered station in the whole detector (T3). This procedure is done in the CDAS with the T2 that are transmitted by the stations.

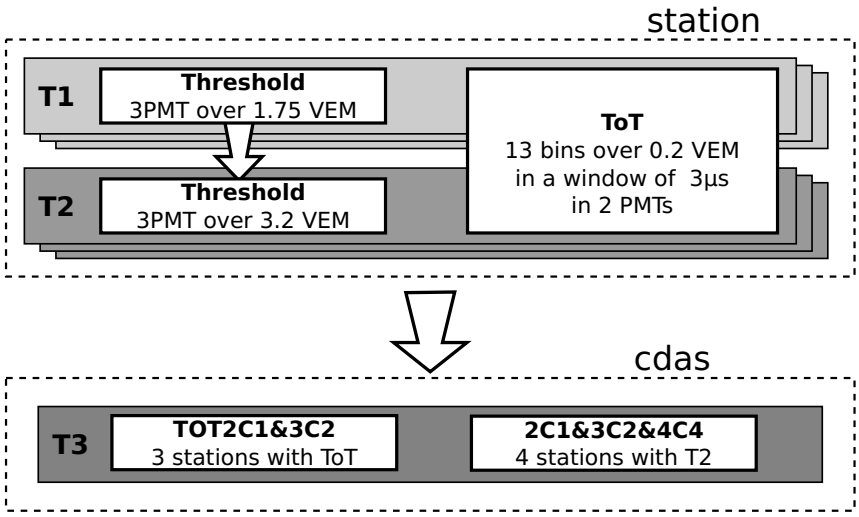

Figure 3.5 Trigger hierarchy scheme in the SD.

At the station stage there are two trigger sub-levels, T1 and T2. The first one is less demanding that the second one and it is the first one to be applied. A signal trace passes the T1 trigger condition if it satisfies one of the following conditions:

- Time over Threshold (ToT): more than 13 bins with a signal superior to 0.2 VEM within a time window of 120 bins (3 μs), in coincidence within at least two of the three PMTs in the station (see left panel in Fig. 3.6).

- Threshold: a signal superior to 1.75 VEM in coincidence in the 3 PMTs.

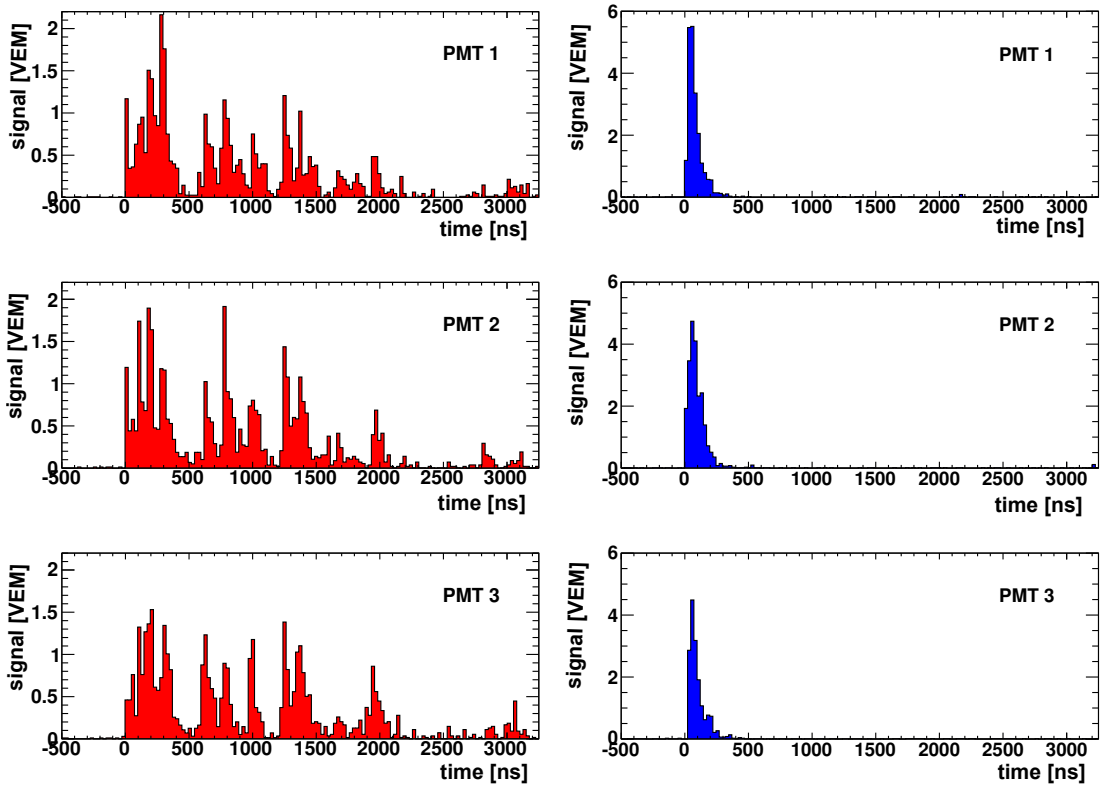

Figure 3.6 *Left:* Example of a typical electromagnetic signal resulting in a T2 ToT trigger. *Right:* Example of a signal produced by a muon generating a T2-Threshold.

The ToT criteria is designed to separate long signals in time produced by the shower front (composed of electrons, photons and muons) from short signals produced by atmospheric muons. It has a trigger frequency of $1-5\,\mathrm{Hz}$, which is the expected for the random coincidence within the $3\,\mu\mathrm{s}$ window between two atmospheric muons.

The Threshold criterion is more noisy, having a trigger frequency of 100 Hz. It was included to take into account the muonic component which is dominant in horizontal showers.

The T2 trigger conditions are evaluated at the stations over the signals that already passed the T1. The purpose is to filter random triggers and diminish the trigger rate from 100 Hz to 20 Hz, which is the limitation imposed by the comunication system[1]. In order to be promoted to a T2 the T1 must accomplish one of the following conditions:

- Time over Threshold (ToT): all T1 that are ToT are promoted to T2 with no other condition.
- Threshold: the signal needs to be higher than 3.2 VEM in the three photomultipliers (see right panel in Fig. 3.6).

[1]The purpose of having an initial T1, instead of applying the T2 directly, is that once the event passes the third level trigger all T1 stations will be read.

If a signal satisfies both conditions it is labeled as ToT. Only when the station has a T2, it sends the trigger (not the trace) information to the CDAS.

The T3 trigger conditions are applied in real time at the level of the global detector. The CDAS monitors the stream of incoming T2 events with a software on a central computer. The T2 events are stored in a temporary buffer and sorted according to their trigger time. This buffer is then scanned with a sliding window of 50μs in search of a compact spatial configuration of the T2-emmitting stations in the window. The two possible conditions for a set of T2 stations producing a T3 in the surface detector are:

- TOT2C1&3C2: Only ToT stations are considered. The compact spatial configuration requires that one of the stations must have at least one neighbour in the first crown and a second in the second crown (see left panel in Fig. 3.7). Once the spatial coincidence is verified, timing criteria are imposed: each T2 must be within $(6 + 5C_n)\mu$s of the first one, where C_n denotes n^{th} crown. .

- 2C1&3C2&4C4: The second T3 mode is more permissive. It requires a four-fold coincidence of any T2 with a moderate compactness. Namely, among the four fired stations at least one must have a neighbour in the the first crown, another in the second and the last one can be as far as in the fourth (see right panel in Fig. 3.7). Concerning timing criteria, the same logic as for the "ToT2C1&3C2" is applied.

If any of those conditions is fullfilled, the central computer emits a T3.

Up to January 2007, the entire surface detector array was read out upon a T3 event. The SD array was still growing at that time up to a point, where the read-out of the whole array produced an unacceptably high load on the radio communication system. The CDAS was therfore changed and since then it reads out only the first six crowns around each T2.

Upon a read-out request, every candidate station sends its station ID, signal traces, trigger information, position, calibration histograms, and error code concerning the communication to the CDAS.

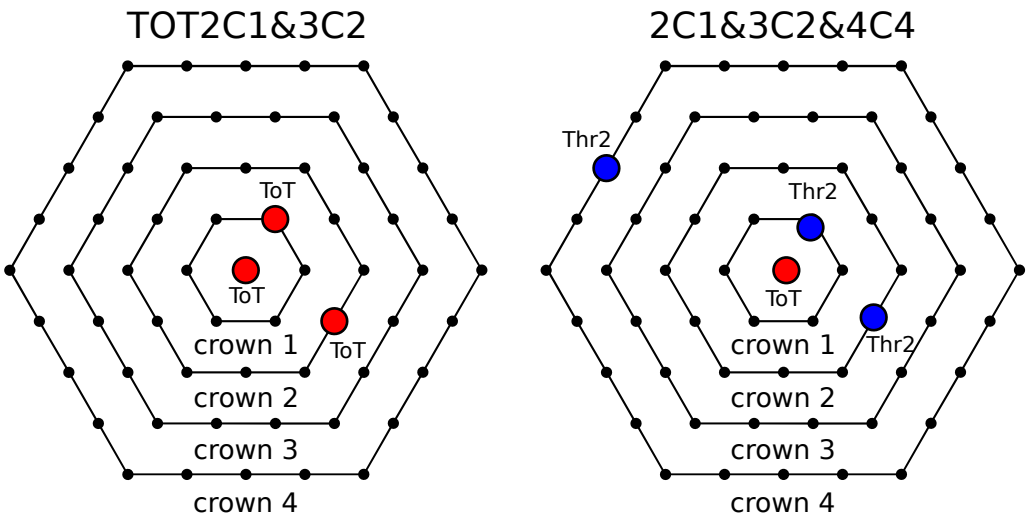

Figure 3.7 *Left:* One of the possible configurations producing a T3 TOT2C1&3C2. *Right:* One of the possible configurations producing a T3 2C1&3C2&4C4.

4

Monte Carlo simulations: neutrinos

Monte Carlo (MC) simulations of neutrino interactions and neutrino-induced showers are a fundamental tool in this thesis. Given the fact that there are no neutrino induced showers detected until now, it is necessary to rely on simulations for the development of the identification criteria and for the calculation of the surface detector exposure to UHE neutrinos.

In Chapter 2 we have summarized the weak interaction channels through which a neutrino can initiate an atmospheric shower. In this chapter we will concentrate on the "Earth-skimming" channel and explain the simulation process. We will separate this process into two steps:

1. Earth processes: neutrino interaction and tau propagation in the Earth crust (Section 4.1).

2. Atmospheric processes: tau decay, atmospheric shower and particle detection (Section 4.2).

In Section 4.3 we define a weight for each simulated shower to take into account the probability to be produced by a diffuse isotropic E^{-2} neutrino flux.

4.1 Earth processes

In order to simulate the interactions of UHE ν_τ in the Earth, we have to characterize the different physical processes at work in the neutrino and tau propagation.

4.1.1 Neutrino Interaction

During the propagation of the neutrino through the Earth, it will interact with nucleons from the surrounding matter. The interaction with electrons is negligible[1] [82]. In the framework of the Standard Model, the neutrino-nucleon charged currrent (CC) ($\nu_\tau + N \to \tau + X$) and neutral current (NC) ($\nu_\tau + N \to \nu_\tau + X$) cross-sections, $\sigma^{CC}_{\nu_\tau}$ and $\sigma^{NC}_{\nu_\tau}$, describe deep-inelastic scattering (DIS) processes. The X stands for all the resulting particles disregarding the τ (ν_τ) in the CC (NC) process which result in a jet.

The cross-sections are expressed in terms of the structure functions of the nucleon, which in turn depend on the individual parton distribution functions (PDFs). The PDFs are obtained from measurements at accelerators, in restricted ranges of Bjorken-x and momentum transfer Q^2. However, the kinematic range probed by UHE neutrinos is outside the measured domain and therefore extrapolations are needed. If a neutrino interacts with a nucleon at a center of mass energy $\sqrt{s} = 10^{14}$ eV ($E_\nu = 5.3 \times 10^{18}$ eV) the relevant range of x is: $10^{-8} \lesssim x \lesssim 10^{-4}$. The relevant range in Q^2 is: $50 \lesssim Q^2 \lesssim 10^4$ GeV^2, where the exact region increases only slowly with E_ν because the contribution of higher Q^2 ($Q^2 > M_W^2$) is suppressed by the W-propagator.

The calculation of the σ_{ν_τ} at energies above 10^{17} eV has been performed by several authors. Pioneering estimates were presented in 1996 by Gandhi *et al* using PDFs from the CTEQ and MRS collaborations and applying a leading-order (LO) Altarelli-Parisi evolution to obtain the distributions at high Q^2 [82]. More recently, between 2006 and 2011, Sarkar *et al* updated the result using new HERA data which modified the PDFs and also extended the calculation at next-to-leading-order (NLO) [97, 98]. We adopt this result as the reference cross-section used in this work. In 2008, Armesto *et al* studied different methods to calculate the σ_{ν_τ} in order to estimate the uncertainty of this magnitude [99]. The uncertainty is dominated by the way the PDFs are extrapolated to very low x. The highest estimate of σ_{ν_τ} was derived extrapolating the structure function as $F_2 \propto x^{-\lambda}$ with $\lambda = 0.0481 \ln(Q/0.0292)^2$ saturating at $\lambda = 0.4$ as higher values of λ are in contradiction with perturbative calculations. The lowest σ_{ν_τ} estimate was derived using an extrapolation of F_2 following the ASW parametrization which saturates faster [100].

In Figure 4.1 we show the three calculations for the $\sigma^{CC}_{\nu_\tau}$ described before together with the relative difference between the highest (lowest) and the reference [2]. Similar considerations apply to the neutral current channel, which is ~ 2.5 lower than the CC case.

[1] The $\sigma(\nu_\tau e)$ is 0.01 that of $\sigma(\nu_\tau N)$.

[2] The relative difference for a given model A is $\frac{A-Ref}{Ref}$

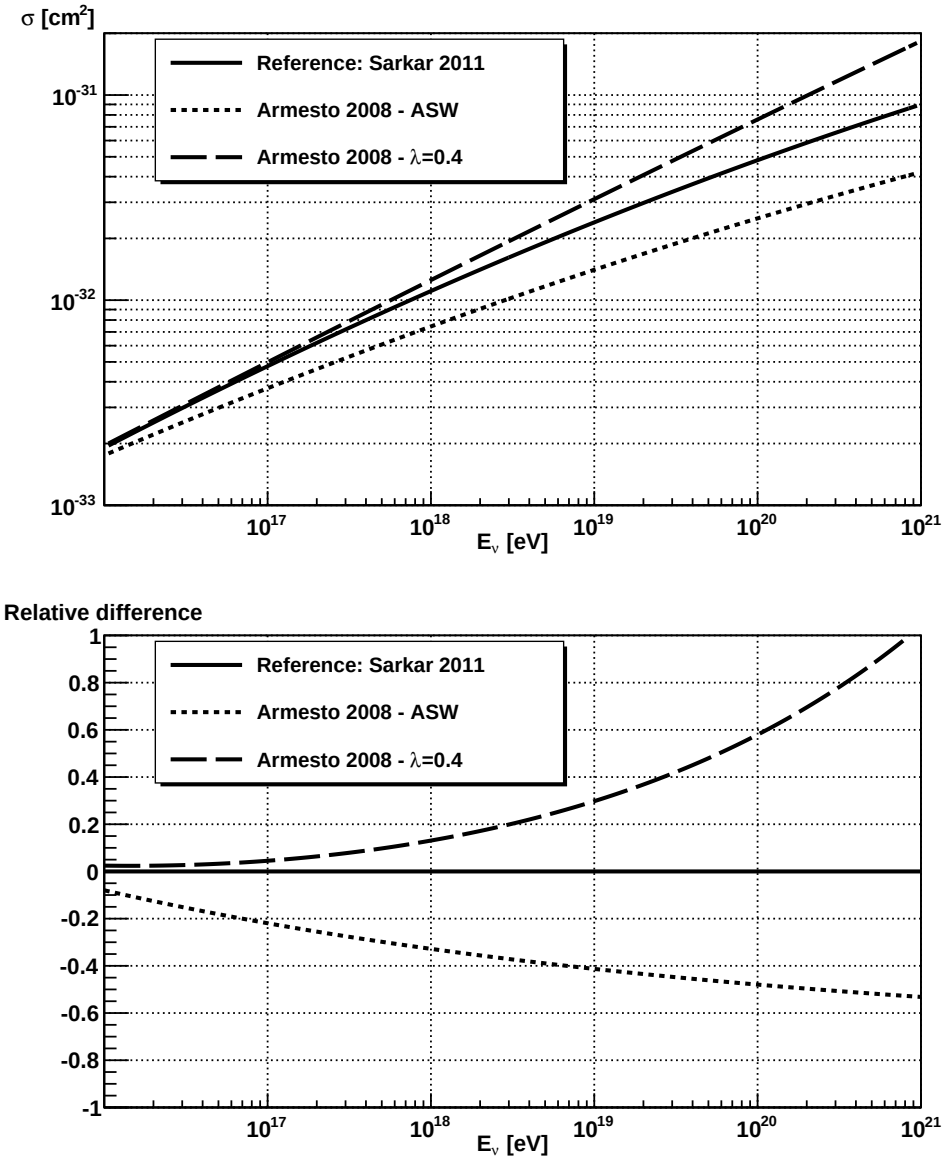

Figure 4.1 *Top:* Neutrino cross-section on isoscalar targets for CC scattering. *Bottom:* Relative difference between the highest (lowest) and the reference.

We have performed a parametrization for the three calculations assuming a dependence of:

$$\log\left(\sigma/\mathrm{cm}^{32}\right) = A + B\log\left(E_\nu/\mathrm{eV}\right) + C(\log\left(E_\nu/\mathrm{eV}\right))^2 \tag{4.1}$$

where A, B and C are fitted parameters. The parametrization agrees with the data within less than 5% in the entire range. The results of the parametrizations are presented in Table 4.1.

The cross-section of neutrinos and antineutrinos are the same at energies above

Model	A	B	C
Reference: Sarkar 2011	-0.39	0.64	-0.016
Highest (optimistic): pQCD $\lambda = 0.4$	0.27	0.45	-0.003
Lowest (pesimistic): ASW	0.25	0.52	-0.013

Table 4.1 Parameters in equation 4.1 for the three models described in the text.

10^{17} eV. At 10^{14} eV the neutrino cross-section is higher by only 15%. This means that we can consider only neutrino cross-sections and use the same results for the antineutrinos.

Another important parameter when considering the DIS processes is the distribution of the energy transfered to the jet in an interaction. This magnitude is called the inelasticity y. In Figure 4.2 we show the distribution of the inelasticity for CC and NC channels for an interaction of a 10^{18} eV neutrino with an isoscalar target. The average inelasticity is ~ 0.2 for both CC and NC processes. This distribution also does not change when considering antineutrinos and remains the same at higher energies.

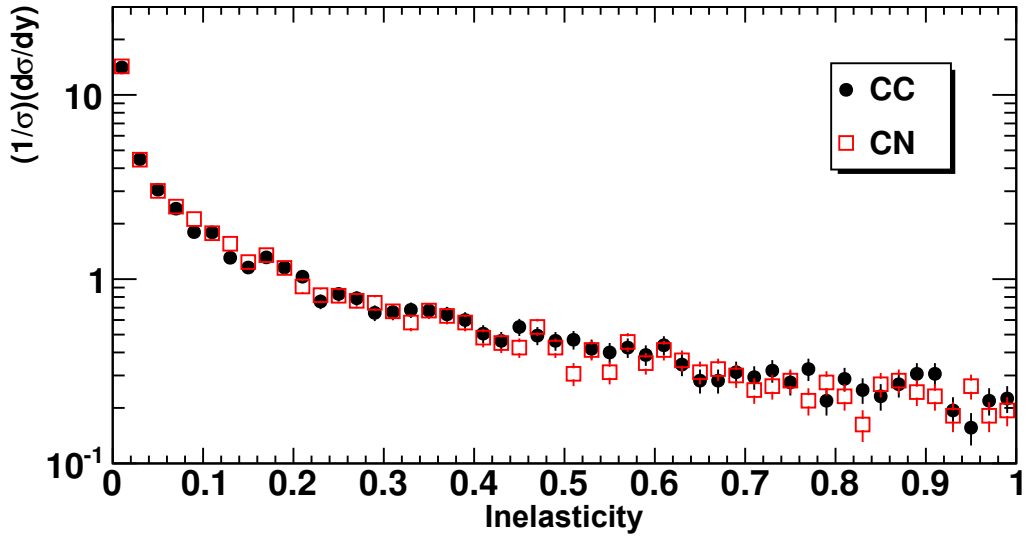

Figure 4.2 Inelasticity distribution for the charged and neutral interactions of a 10^{18} eV neutrino and an isoscalar target.

4.1.2 Tau Propagation

There are different processes through which the tau can loose energy as it propagates through the Earth. The four dominant ones are ionization, bremsstrahlung,

pair production and photonuclear effect.

To first order energy loss by ionization is independent of the τ energy, while the other three processes are linear in E. For this reason the energy loss per unit length can be written as:

$$-\left\langle \frac{dE}{dX} \right\rangle = \alpha(E) + \beta(E) \times E \tag{4.2}$$

$\alpha(E)$ and $\beta(E)$ are functions of the energy and describe the deviations from the first order behaviour. $\alpha(E)$ represents the ionization losses and $\beta(E) = \beta_{bremss}(E) + \beta_{pair}(E) + \beta_{nuc}(E)$, where the suffixes stand for the different electromagentic processes, bremsstrahlung (brem), pair production (pair) and photonuclear effect (nuc).

Ionization is produced by the coulomb interaction of the τ with the electrons in the medium. This process is described by the Bethe-Bloch equation, with a correction for density effects, which comes from the fact that, in a dense medium like Earth, atoms cannot be considered isolated. For the range of energies considered in this work, the effect of ionization is negligible compared to the three other processes:

$$-\left\langle \frac{dE}{dX} \right\rangle \sim 10^{-3} \text{ GeV g}^{-1}\text{cm}^2 \tag{4.3}$$

Between 10^{20} eV and 10^{16} eV the increase of the energy loss due to ionization is only 30% [3].

The evaluation of bremsstrahlung and pair-production tau energy loss is carried in detail in Ref [101] based on the differential bremsstrahlung cross-section developed by Petrukhin and Shestakov [102] and pair production differential cross-section estimation from Kokoulin and Petrukhin [103].

For muons, bremsstrahlung is a dominant source of energy loss, but for tau leptons it appears highly suppressed by a $\left(\frac{m_\mu}{m_\tau}\right)^2$ factor, where $m_\tau \approx 17 \times m_\mu \approx 3500 \times m_e$. For the range of energies considered in this work, the effect of bremsstrahlung large compared to ionization:

$$-\left\langle \frac{dE}{dX} \right\rangle_{bremss} \sim 8 \times 10^{-9} \times E \text{ g}^{-1}\text{cm}^2 \tag{4.4}$$

$\beta_{bremss}(E)$ can be considered constant in the entire range.

For pair-production the energy dependence is also negligible:

$$-\left\langle \frac{dE}{dX} \right\rangle \sim 1.4 \times 10^{-7} \times E \text{ g}^{-1}\text{cm}^2 \tag{4.5}$$

It is more important than bremsstrahlung by a factor 175, so bremsstrahlung can also be ignored.

[3] $\frac{\alpha(10^{20}\text{eV})}{\alpha(10^{16}\text{eV})} \sim 1.3$

The fourth process responsible for tau energy loss is the photonuclear effect. This corresponds to the interaction of the tau with the nuclei through the exchange of a virtual photon (DIS). This process exceeds pair production above $\sim 5 \times 10^{14}$ eV.

There are many different parametrizations for this cross-section, as it involves the structure function for a nuclear target A (F_2^A). Armesto *et al* [99] reviewed the different approaches to calculate β_{nuc} in order to estimate its uncertainty [99]. The relevant range of x for a 10^{18} eV neutrino is $10^{-9} \lesssim x \lesssim 10^{-6}$ while the relevant range in Q^2 is: $10^{-1} \lesssim Q^2 \lesssim 50$ GeV^2. The uncertainty is also dominated by how the structure function is extrapolated to low x.

In this work, we adopt as a reference the β_{nuc} derived using the structure function from ALLM [104]. The highest β_{nuc} considered is obtained using the F_2^A by Petrukhin *et al.* (PT) [105] and the lowest using F_2^A from Armesto *et al.* (ASW) [100].

In Figure 4.3 we show the different contributions to $\beta(E)$ under the different models considered. The bremstrahlung and pair-production are shown added together although the pair-production is highly dominant $\beta_{brem} + \beta_{PP} \sim \beta_{PP}$. We show the β_{nuc} alone and β_{total}. In the case of ASW the contribution of β_{PP} is relevant, however, for the other two models it becomes negligible, particularly in this energy range where pair production is constant, whereas β_{nuc} increases with E. It is to be remarked that the model by PT provides estimates of β_{nuc} only up to 10^{18} eV, so for higher energies we have to rely on an extrapolation.

We have performed a parametrization for the three models assuming a dependence of of the form:

$$\beta(E_\tau) = b_0 + b_1 E_\tau^{b_2} \tag{4.6}$$

where b_0, b_1 and b_2 are free fit parameters. The parametrization agrees with the calculation in less than 5% in the entire energy range. The fit results are presented in Table 4.2.

Model	b_0	b_1	b_2
Reference: ALLM	2.1×10^{-7}	4.9×10^{-9}	0.23
Highest: PT	3.1×10^{-7}	4.4×10^{-10}	0.42
Lowest: ASW	-4.7×10^{-8}	1.9×10^{-7}	0.05

Table 4.2 Parameters in equation 4.6 for tau energy losses for the three models described in the text.

The energy of the tau after traveling a distance x is obtained integrating:

$$-\left\langle \frac{dE}{dX} \right\rangle = \rho\beta(E) \times E \tag{4.7}$$

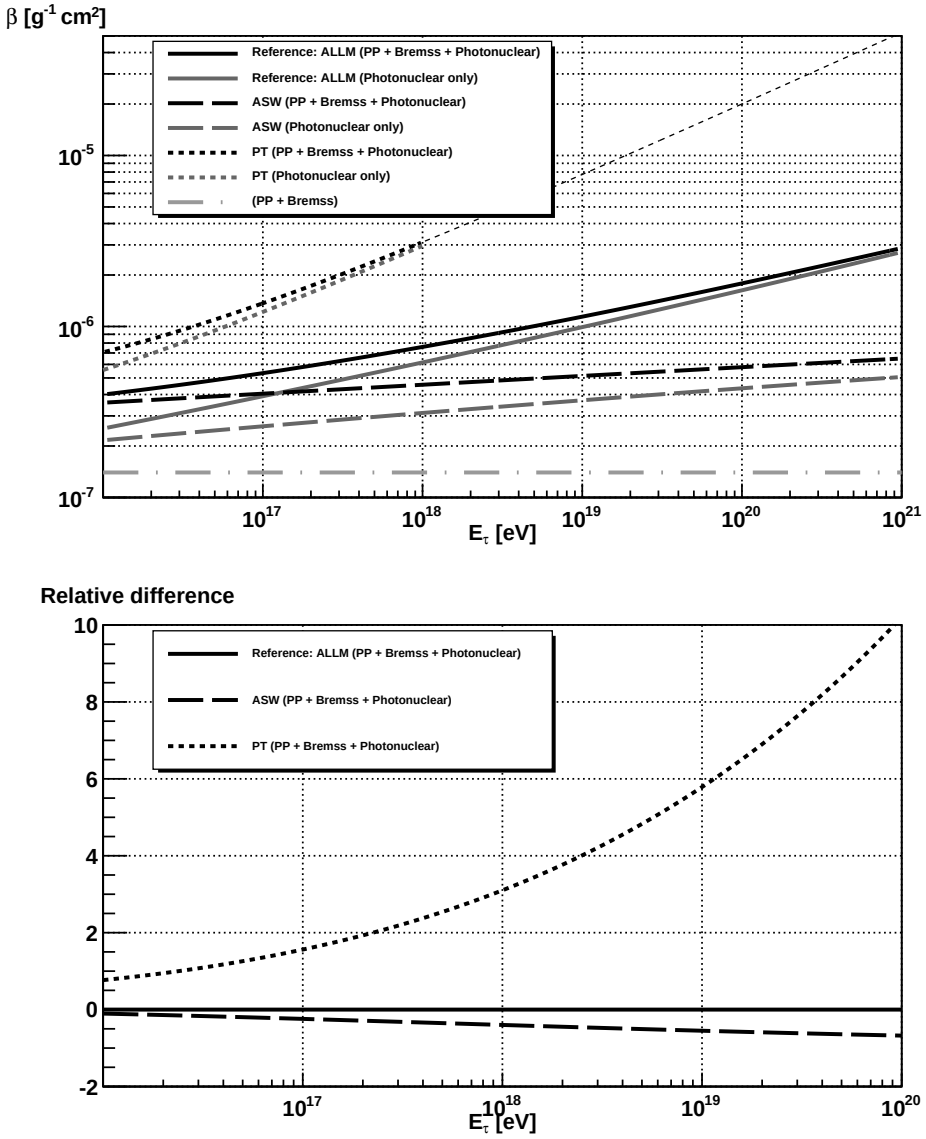

Figure 4.3 *Top panel:* Tau energy losses in standard rock (A=22). In grey dot-dashed the contribution from pair-production (PP) and bremsstrahlung (Bremss) dominated by PP (see text for details). In (dashed/dotted) grey solid the contribution from photonuclear effect for the ALLM (ASW/PT) parametrization. In black the sum of the three processes. *Bottom panel:* The relative difference between ASW (PT) and the referece model, ALLM.

The result using the parametrization in equation 4.6 is:

$$E(X) = \left[\frac{b_0 E_0}{(b_0 + b_1 E_0^{b_2}) \exp\left(\rho b_0 b_2 X\right) - b_1 E_0^{b_2}} \right]^{\frac{1}{b_2}} \tag{4.8}$$

where E_0 is the initial τ energy.

The τ is a particle with a short lifetime ($\tau_\tau = 2.9 \times 10^{-13}$s, $c\tau_\tau = 87\mu$m). The decay length is $\lambda_{dec} = c\,\tau_\tau \frac{E_\tau}{m_\tau} \approx 49 \left(\frac{E_\tau}{10^{18}\text{eV}}\right)$km. At low energies the tau decay length is small enough so that energy losses can be neglected. However, in the range of energies considered in this work ($E > 10^{16.5}$eV) this is not the case. The survival probability as a function of distance X is given by:

$$P(X) = \exp\left[-\int_0^X \frac{m_\tau}{c\tau_\tau}\frac{dX}{E(X)}\right] \tag{4.9}$$

If no energy losses are considered the result for a τ with an initial energy E_0 is straightforward: $P(x) = \exp\left(-\frac{m_\tau X}{c\tau_\tau E_0}\right) = \exp\left(-\frac{X}{\lambda_{dec}}\right)$. When tau energy losses are taken into account we have to integrate equation 4.8.

The range R is defined as the distance a beam traverses before its inelasticity is reduced to $1/e$, i.e. $P(R) = e^{-1}$. In Figure 7.13 we show the range as a function of the initial energy of the τ.

Even though the range decreases when the tau energy loss increases the realation between the two is not inversely proportional. For example, at 10^{20} eV PT is 11 times higher than ALLM, while the range is only 3 times lower.

Now we can estimate the probability that a 1° Earth-skimming neutrino will give rise to an emerging tau. Given that the interaction length, λ_{int}, for a 10^{18} eV tau neutrino in rock is 620 km, and that at 1° the distance through Earth is 220 km, only 30% of the incident neutrinos will interact. Figure 4.5 shows the interaction probability density as a function of travelled distance. Now, 10^{18} eV interacting neutrinos will produce taus with average energy of 8×10^{17} eV, which have a 12 km range in rock. Therefore, only the neutrinos interacting in the last 12 km of their journey through Earth will produce an emerging tau. These are signaled by the black area on Figure 4.5, and correspond to 1.4% (4.6%) of the incident (interacting) neutrinos.

4.1.3 Monte Carlo simulations

The Monte Carlo generator provides a natural way to deal with both neutrino interactions and tau energy losses. The method consists in following the incident particles all the way through the rock, deciding at each step on their fate according to the distribution of possible processes. The algorithm used is schematically represented in Figure 4.6.

Using this MC generator with a fixed neutrino energy and angle of incidence [4], one obtains the energy probability density for producing a tau that reaches the surface of the Earth $\frac{dn_\tau}{d\log E_\tau}$. To a very good approximation the angle of incidence

[4]The angle of incidence fixes the amount of matter the particles traverse.

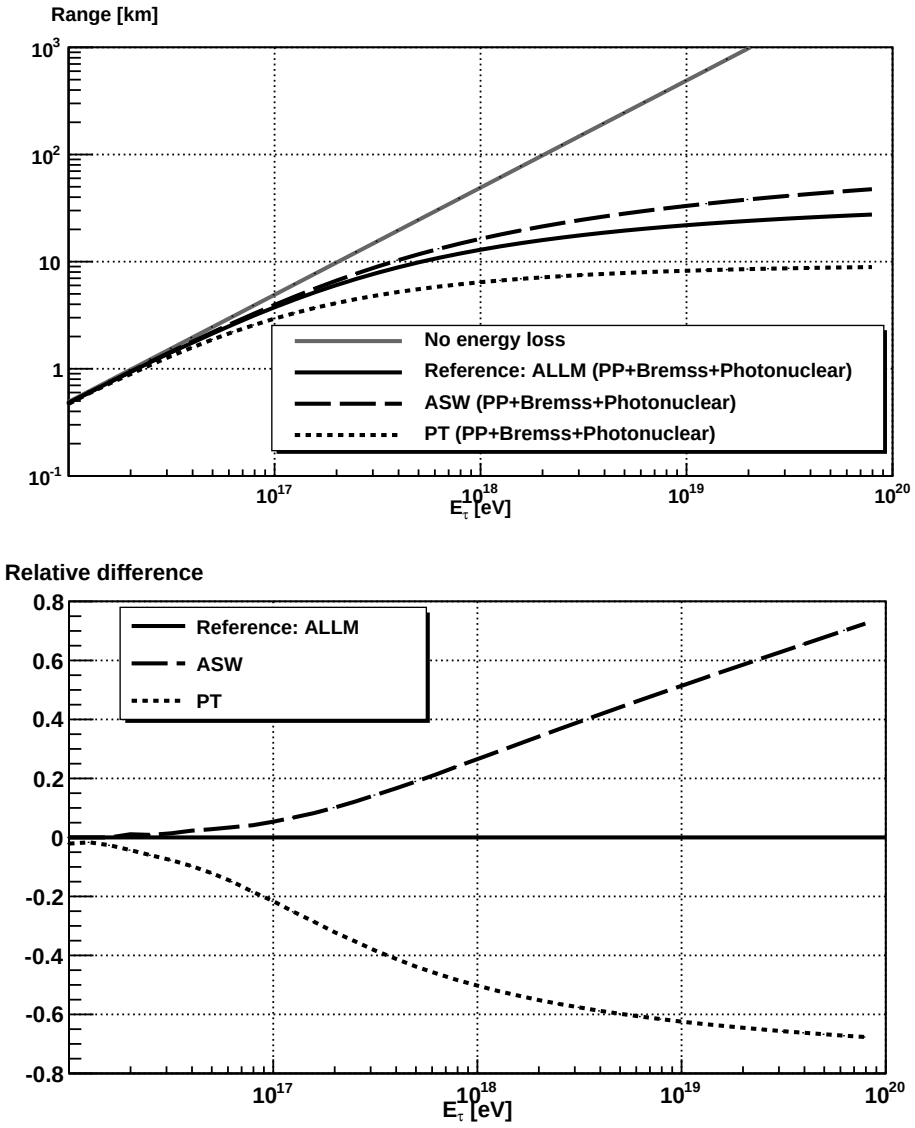

Figure 4.4 *Top panel:* Range: average distance before the τ decays. Solid grey: no τ energy losses are considered. Solid (dashed/dotted) black: the range considering pair production (PP), bremsstrahlung (Bremss) and photonuclear for the ALLM (ASW/PT) parametrization. *Bottom panel:* The relative difference between the range calculated in with ASW and PT and the reference model, ALLM.

is considered to be the same as the one of the injected neutrino. In Figure 4.7 we show these probabilities for 10^{18}eV neutrinos.

The integral values of the probability density functions are in agreement with the expectations discussed in the previous Section.

In Section 7.2.5.1 we will evaluate how these probability density functions change according to different parametrizations of the interaction cross-section and tau energy loss.

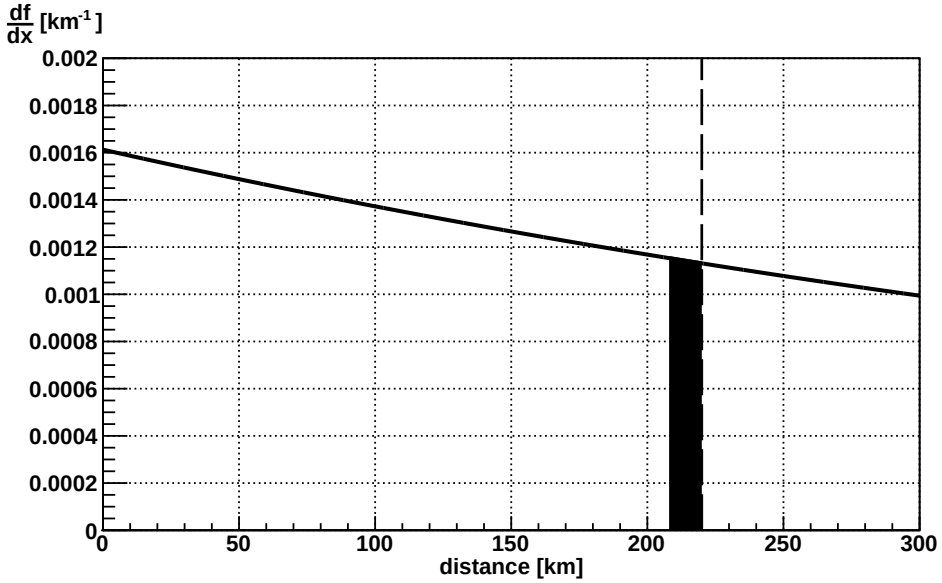

Figure 4.5 Interaction probability density of a 10^{18} eV neutrino skimming the Earth at 1° below the horizon. At this angle the distance that a neutrino has to go through is 220 km. The surface of the Earth is marked with a dashed line. The differential probability is an exponential with $\lambda_{int} = 620$ km. The approximate depths where on average an interacting neutrino can give rise to an emerging τ is shown with the black area, and corresponds to 1.4% of the incident flux.

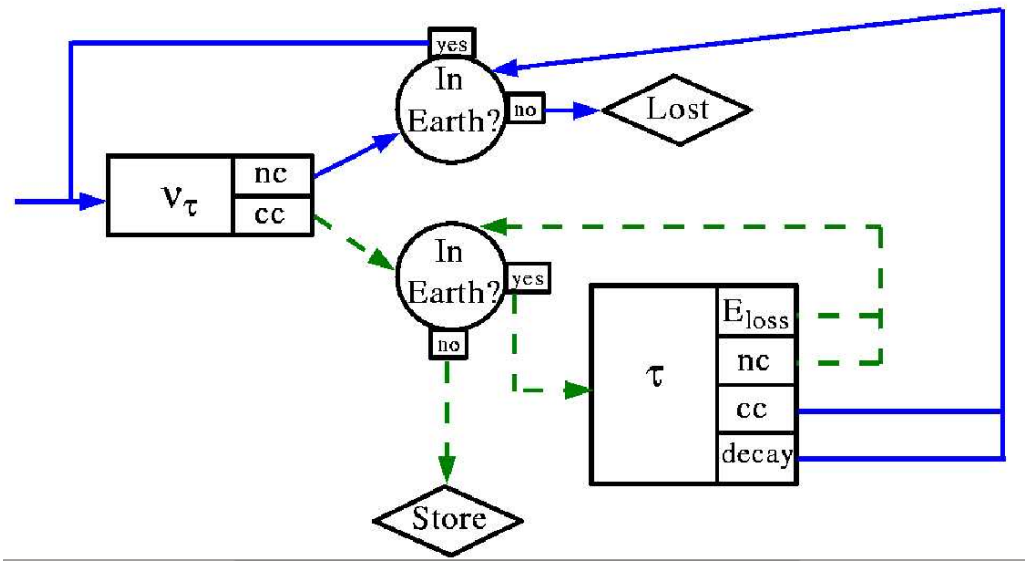

Figure 4.6 Schematic algorithm of the Monte Carlo simulation for the Earth interactions. The ν_τ (solid line) and the τ are followed until they leave the Earth. Then, if the emerging particle is a τ its energy is stored.

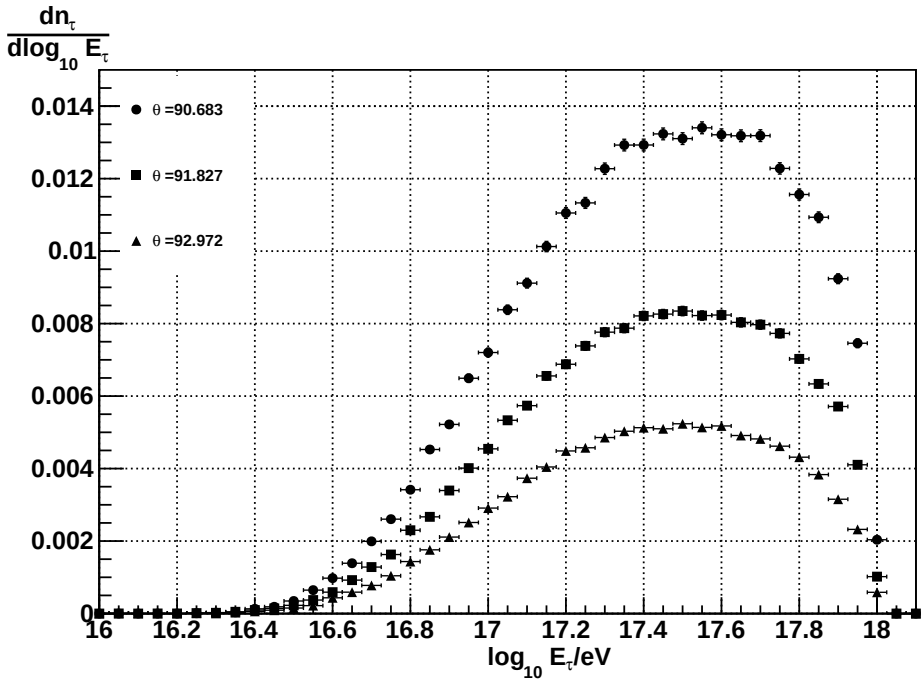

Figure 4.7 Probability density function (pdf) for an emerging tau as a function of its energy in logarithmic scale. The pdf depends on the energy of the neutrino and the zenith angle θ. In this example the energy is fixed at $E_\nu = 10^{18}$ eV. Three zenith angles are shown: $\theta = 90.683°$ (circles), $\theta = 91.827°$ (squares) and $\theta = 92.972°$ (triangles) with corresponding traveled distances in the of Earth 152, 407 and 661 km. The integral of each pdf is 1.3%, 0.8% and 0.5% respectively.

4.2 Atmospheric simulation

The simulation sequence in the atmosphere can be divided into three steps:

1. τ **decay:** Determination of the particles produced when the τ decays (Sec. 4.2.1).

2. **Atmospheric evolution of the shower:** simulation of the shower generated by the τ decay products until the shower reaches the surface of the Earth (Sec. 4.2.2).

3. **Surface detector response:** Simulation of the signals registered by the surface detector stations of the Pierre Auger Observatory from the particles that go through them (Sec. 4.2.3).

The sequence is schematically represented in Figure 4.8.

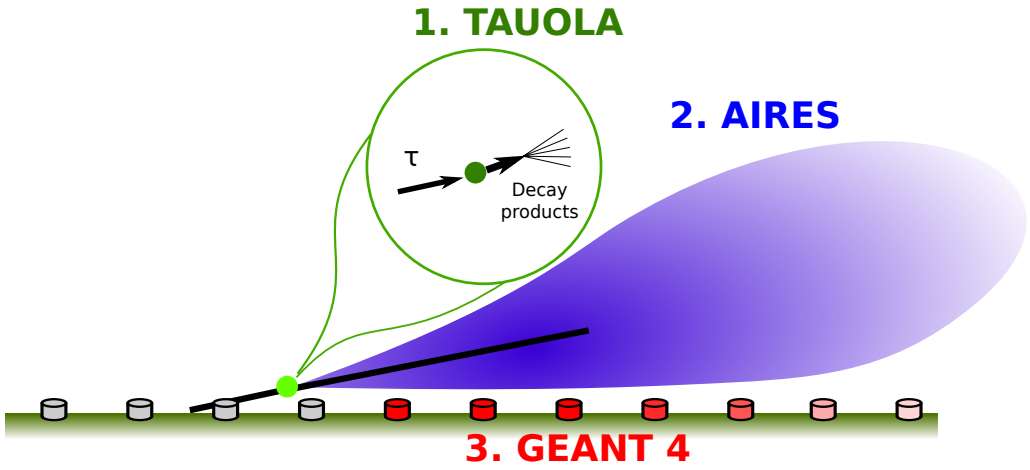

Figure 4.8 Scheme of the three different processes taken into accout for the simulation of the atmospheric and detector simulation. In green the high energy τ decay, in blue the atmospheric evolution of the shower and in red the surface detector response.

4.2.1 Simulation of τ decay

The CC interaction that gives rise to τ leptons is mediated through the W boson. The W couples only to left chirality and at ultra-relativistic energies chirality is the same as helicity. Consequently, tau neutrinos ν_τ (tau anti-neutrinos $\bar{\nu}_\tau$) will produce only τ^- with negative helicity (τ^+ with positive helicity), Figure 4.9.

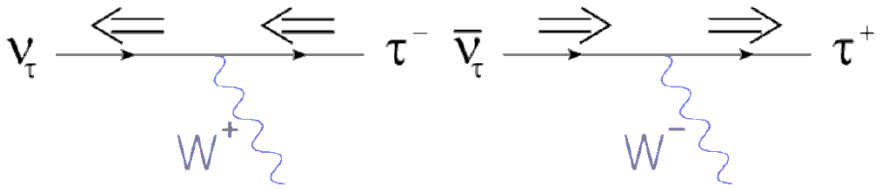

Figure 4.9 Feynman diagrams of the ν_τ and $\bar{\nu}_\tau$ interactions resulting in a tau lepton.

In order to simulate the decay of the tau we use the package TAUOLA [106] that contains all the experimental information on final states and branching ratios. In Table 4.3 we show the most important channels.

It is important to use only negative helicity for the τ^- decay. The fraction of energy that goes into the shower, i.e the sum of the energy of all particles except for neutrinos, can change considerably if one incorrectly uses positive polarization for negative taus. In order to illustrate this we can consider channel number 4 in Table 4.3, which provides a simple example.

Number	Decay	Probability (%)
1	$\tau^- \to \pi^-\pi^0\nu_\tau$	∼25.5
2	$\tau^- \to e^-\bar{\nu}_e\nu_\tau$	∼17.9
3	$\tau^- \to \mu^-\bar{\nu}_\mu\nu_\tau$	∼17.4 **Unobservable**
4	$\tau^- \to \pi^-\nu_\tau$	∼10.9
5	$\tau^- \to 2\pi^-\pi^+\nu_\tau$	∼9.3
6	$\tau^- \to \pi^-2\pi^0\nu_\tau$	∼9.3
7	$\tau^- \to 2\pi^-\pi^+\pi^0\nu_\tau$	∼4.6
8	$\tau^- \to \pi^-3\pi^0\nu_\tau$	∼1.0

Table 4.3 The eight most frequent τ decay channels. The other decay channels amount to 4.1%. τ^+ decay modes are charge conjugate of the modes shown. Channel number 3 is unobservable because the μ is unlikely to interact or decay and produce an UHE shower within the observable region of the atmosphere.

Consider the $\tau^- - \to \pi^- + \nu_\tau$ decay in the Laboratory frame choosing the z-axis parallel to the τ momentum. The energy of the particles is:

$$E_i^{Lab} = \gamma(E_i^{CM} + \beta p_{z,i}^{CM}) \tag{4.10}$$

where $i = \tau$, ν and π^-, $\gamma = (1-\beta^2)^{-1} = \frac{E_\tau^{Lab}}{m_\tau}$ and p_z is the component of the momentum parallel to the direction of the τ.

For $E_\tau^{Lab} \sim 10^{18}$eV and $m_\tau = 1.77$ GeV, $\gamma \gg 1$ so $\beta \approx 1$ and the fraction of energy that goes into the shower is:

$$x_i = \frac{E_{\pi^-}^{Lab}}{E_\tau^{Lab}} = \frac{E_{\pi^-}^{CM} + \beta p_{z,\pi^-}^{CM}}{E_\tau^{CM} + \beta p_{z,\tau}^{CM}} = \frac{1}{2}(1 + \cos\Theta) \tag{4.11}$$

where Θ is the angle between the polarization of the τ and $\vec{p}_{\pi^-}^{\,\mathrm{CM}}$.

For a τ polarized in $\hat{z}$ the distribution of the parallel component of the π^- is shown in Figure 4.10. The τ^- with negative (positive) helicity favours π^- produced in the backward (forward) direction. The result is that the fraction of energy that goes into the shower (the energy of the π^-) is less for τs with negative helicity.

The differences between using negative and positive helicity are shown in Figure 4.11 when considering all channels and the corresponding branching ratios.. Using unpolarized or positive helicity for the τ^- results in an overestimation of the exposure.

It is important to notice that the distribution shown in Figure 4.11 is the same for τ^+ with positive polarization. In this way, one can perform the simulations only with τ^- decays, which are the result of the neutrino DIS, and they will also apply to the case of antineutrinos cosmic rays.

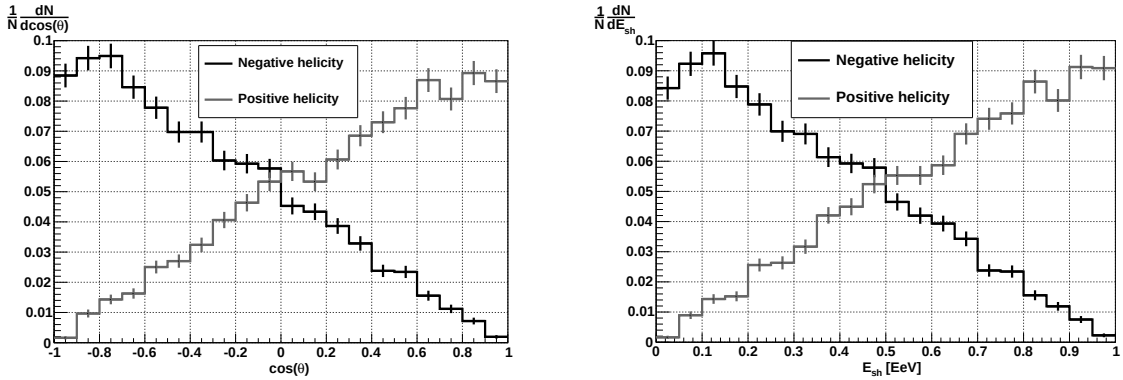

Figure 4.10 Kinematic distributions for the $\tau^- \to \pi^- \nu_\tau$ decay. *Left:* Zenith angle fraction of the π^- in the center-of-mass frame. *Right:* Energy that goes into the shower for a 10^{18} eV tau.

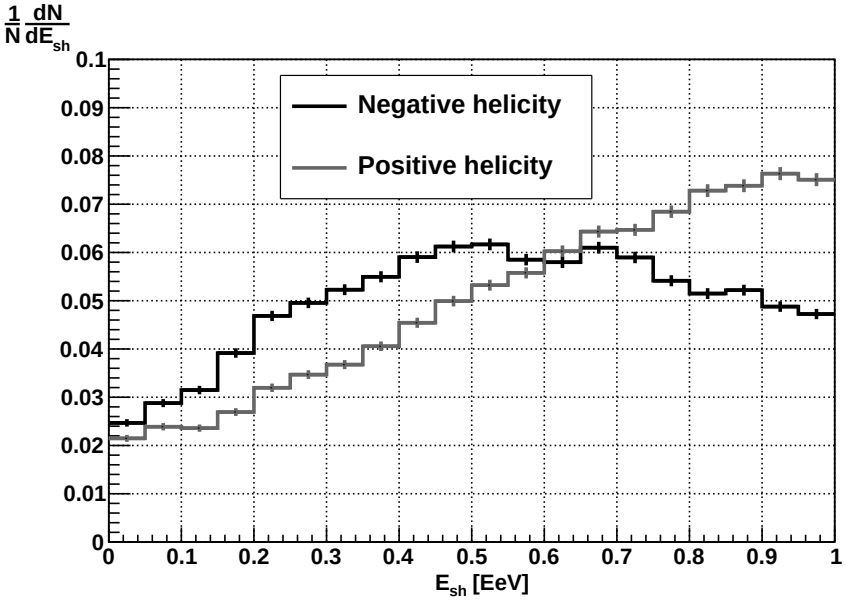

Figure 4.11 Energy of the shower produced by the decay of 10^{18}eV taus, which is defined as the sum of the energy of all particles except for neutrinos. Channel number 3 from Table 4.3 is not considered.

4.2.2 Atmospheric shower

The simulation of the tau decay provides a list of particles and their respective momenta. As discussed in Chapter 2, in an atmospheric shower these particles propagate and interact again generating a large amount of secondary particles. This multiplication process continues until the energy of the secondary particles is no longer sufficient to create a new generation.

In order to simulate this process it is necessary to count with a detailed knowledge of all possible interactions a particle may suffer during the evolution of the shower. This is a complex problem which requires the use of different tools including models of hadronic interactions and the description of the atmospheric density as a function of the altitude.

There are a variety of software packages which group these tools and allow to consider all the aspects of the simulation of an atmospheric shower. The two most common packages are CORSIKA [107] and AIRES [108] which present similar characteristics. In this work, we used AIRES as CORSIKA still has no implementation for up-going showers. A computer code was developed to interpret the TAUOLA output and incorporate the particles within the framework of AIRES. For each of the particles, this code also sets the angle, time and injection depth.

The first generation of particles can have energies four orders of magnitud higher than the ones achieved today in accelerator experiments. Consequently, the models used to simulate the interactions during the first steps of the shower are necessarily extrapolations of measurements performed at much lower energies. As the astroparticle community has not reached consensus about which is the best hadronic model, the AIRES package incorporates the most common ones: SIBYLL [109], QGSJET-I [110] and QGSJET-II [111]. In this work we decided to use the last one to have consistency with the downward-going neutrino analysis in [75]. In Section 7.2.5.2 we discuss the estimation of the uncertainty associated to this choice.

The time and computer memory required to simulate an atmospheric shower scales with the number of particles generated during its evolution. At energies of the order of the EeV this number can be superior to 10^{10} particles so the simulation of the trajectory and their individual evolution is impossible.

Instead, one uses a statistical sampling method in which only a small representative fraction of the particles is propagated. A weight is assigned to each of them to compensate for those particles that are not followed. This method is known as "thinning" [112]. During the first steps of the simulation all propagated particles have a weight of 1. When the multiplicity of the shower increases, only a small fraction of the particles is simulated in detail and their weight increases. The idea of the thinning method is ilustrated considering the following process:

$$A \rightarrow B_1,\ B_2,\ \ldots,B_n \ \text{ with } \ n \geq 1 \tag{4.12}$$

where a "primary" particle A generates a set of secondaries $B_1,\ B_2,\ \ldots,B_n$. Let us denote E_A (E_{B_i}) the energy of A (B_i), and consider a fixed thinning energy E_{th}. Before incorporating the secondaries to the simulation processes, the energy is compared with E_{th} and:

- If $E_A \geq E_{\text{th}}$, every secondary is analyzed separately. They are accepted with probability P_i given by:

$$P_i = \begin{cases} 1 & \text{if} E_{B_i} \geq E_{\text{th}} \\ \frac{E_{B_i}}{E_{\text{th}}} & \text{if} E_{B_i} \leq E_{\text{th}} \end{cases}$$

- If $E_A \leq E_{\text{th}}$, the "primary" particle comes from a previous thinning operation. In this case only one of the secondaries is conserved. The probability that the chosen secondary is B is given by:

$$P_i = \frac{E_{B_i}}{\sum_{j=1}^{n} E_{B_j}} \tag{4.13}$$

  This means that once the thinning energy is reached the number of particles does not increase any more.

In both cases the weight of the accepted secondary particle is the weight of particle A multiplied by the inverse of P_i. The fact that the statistical weights are set with the inverse of the acceptance probabilities ensures an unbiased sampling: all the averages evaluated using the weighted particles will not depend on the thinning energy. Only the fluctuations are affected by the thinning level.

In AIRES the thinning is defined relative to the energy of the primary. For example, a thinning of 10^{-6} corresponds to a simulation where the particles with energy higher than $10^{-6} \times E_{\text{primary}}$ are propagated in detail and have weight 1.

In this work all simulations were performed using a thinning parameter of 10^{-6}. This value allows to reproduce the characteristics of the shower with enough detail so that the fluctuations are negligible. In its determination it was also considered the limit imposed by the computing resources and storage memory. In Section 7.2.5.2 it is discussed the effect of this approximation by comparing these simulations to those with a smaller thinning value of 10^{-7}.

4.2.3 Surface detector response

In order to unify all efforts of the subgroups within the experiment and maintain coherence between the diverse number of analyses, the Pierre Auger Collaboration has developed a modular framework called Offline [113].

Offline provides in particular a set of official modules that allow to perform detector simulations in detail [114]. Next we summarize the most important characteristics of this process.

After the simulation of the shower, the next step is to generate the particles that go through the individual stations which compose the SD. In showers with an energy of the order of the EeV it is impossible to simulate all the individual particles

and just a representative sample is simulated (see Sec. 4.2.2). For this reason, the first step is to perform an "unthinning": a statistical regeneration of the particles to estimate which are the ones entering the SD stations. In this work a technique based on the procedure described in [115] was used, adapted so that one can treat very inclined showers.

Once that the particles that go through the stations are defined, a simulation based on GEANT4 [116] is used to describe the production and propagation of Cherenkov photons within the stations. Each of these photons is propagated until it reaches one of the PMTs or is absorbed in the water. Next, a PMT and electronic dedicated simulation is used to transform these photons into the signal registered by each station.

The simulated signals in the three PMTs are used to calculate the trigger level of each station (ToT, Thr2, Thr1 or none). Those that do not reach any of the trigger conditions are ignored. The stations with trigger level ToT or Thr2 are used in the evaluation of the central trigger T3 (see Sec. 3.1.2). If the configuration of the triggered stations does not produce a T3 trigger the event is discarded as it would in the case of a real shower not triggering the SD.

4.3 Weights

As stated at the begining of this chapter, there are no neutrino induced showers detected until now, so it is necessary to rely on simulations for the development of the identification criteria and for the calculation of the exposure of the detector.

We have simulated 150 tau-induced showers for every point in Figure 4.12. A point is defined by the tau energy E_τ, the zenith angle θ and the decay height X_d. For each of the 150 cases the azimuth angle ϕ of the tau is extracted from a uniform distribution.

Each of these points correspond to different situations which should not appear with the same frequency in the simulated data because they have different probabilities to be produced by a diffuse isotropic E^{-2} neutrino flux and to trigger the array. For this reason, it is necessary to assign to each event a weight w_i which takes into account the contribution of that point to the number of expected events. We define w_i as the number of triggered simulated events per unit time and area for a diffuse neutrino flux that decreases with energy as E_ν^{-2}.

In order to construct the weight, let us consider the ingredients needed to obtain the expected number of events per unit time and area, $\frac{\mathrm{d}N_{\mathrm{exp}}}{\mathrm{d}t\mathrm{d}A}$:

$$\frac{\mathrm{d}N_{\mathrm{exp}}}{\mathrm{d}t\mathrm{d}A} = \int dE_\nu \int dE_\tau \int d\Omega \int dX_d \, \Phi(E_\nu)\, f(E_\tau|\theta, E_\nu)\, h(X_d|E_\tau, \theta)|\cos\theta|\, \varepsilon(E_\tau, \theta, X_d) \tag{4.14}$$

where we will assume $\Phi(E_\nu) = k\, E_\nu^{-2}$, with k the unknown normalization of the flux.

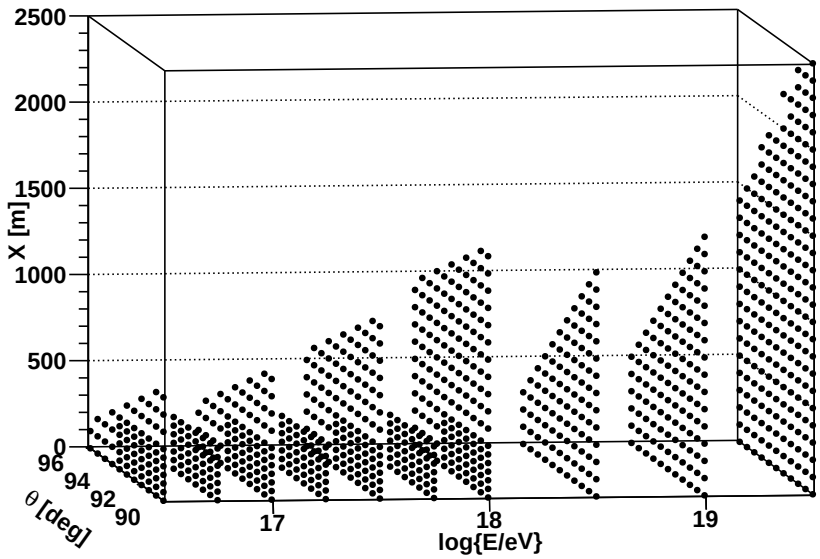

Figure 4.12 Points in the parameter space E_τ, θ and decay height X_d, that have been simulated. In general the simulated points are equidistant in logarithm of energy ($\Delta \log E_\tau = 0.5$), zenith angle ($\Delta\theta = 0.01$ rad $\approx 0.57°$) and decay height ($\Delta X_d = 100$ m). For $90° < \theta < 94°$ and $\log E_\tau < 18$ the parameter space is covered more densely simulating points at intermediate energies and decay heights.

$f(E_\tau|\theta, E_\nu)$ is the probability density function (pdf) of a tau emerging from the Earth with energy E_τ given a neutrino with energy E_ν crossing an amount of Earth determined by the zenith angle θ. These pdf are explained in Section 4.1.3.

$h(X_d|E_\tau, \theta)$ is the pdf that the τ decays at a height X_d if it has energy E_τ and direction θ. To a good approximation the energy loss of the tau in the atmophere can be neglected. As a consequence, the pdf for the tau decay in the atmosphere is an exponential, where the characteristic decay length depends on E_τ: $\lambda(E_\tau) = c\,\tau_\tau \frac{E_\tau}{m_\tau} \approx 49 \left(\frac{E_\tau}{\text{EeV}}\right)$ km. If we denote by D the distance travelled by the τ before the decay:

$$\hat{h}(D|E_\tau) = \frac{1}{\lambda(E_\tau)} \exp\left(-\frac{D}{\lambda(E_\tau)}\right) \rightarrow h(X_d|E_\tau, \theta) = \frac{1}{|\cos\theta|\,\lambda(E_\tau)} \exp\left(-\frac{X_d}{|\cos\theta|\,\lambda(E_\tau)}\right) \tag{4.15}$$

where we have used $D = \frac{X_d}{|\cos\theta|}$.

The factor $|\cos\theta|$ appears in equation 4.14 as we have to project the area onto the direction of the incoming flux.

$\varepsilon(E_\tau, \theta, X_d)$ is the trigger efficiency defined as:

$$\varepsilon(E_\tau, \theta, X_d) = \frac{N_{\text{trigger}}}{N_{\text{simulated}}} \tag{4.16}$$

where $N_{\text{simulated}}$ is the number of simulated showers and N_{trigger} is the number of these showers that triggered the array for each (E_τ, θ, X_d) point.

If we want to decompose $\frac{\mathrm{d}N_{\text{exp}}}{\mathrm{d}t\mathrm{d}A}$ as a sum of weights for the points shown in Figure 4.12 we need to integrate over the terms with a dependence on E_ν:

$$t(E_\tau, \theta) \equiv \int_{E_\tau}^{\infty} dE_\nu \, f(E_\tau|\theta, E_\nu) \, E_\nu^{-2} \tag{4.17}$$

With this definition $\frac{\mathrm{d}N_{\text{exp}}}{\mathrm{d}t\mathrm{d}A}$ results in $\frac{\mathrm{d}N_{\text{exp}}}{\mathrm{d}t\mathrm{d}A} = k \times \sum w_i$, where w_i is:

$$w_i = 2\pi \sin\theta \; h(X_d|E_\tau, \theta) \; \varepsilon(E_\tau, \theta, X_d) \; |\cos\theta| \; t(E_\tau, \theta) \; E_\tau \ln 10 \; \Delta \log E_\tau \; \Delta\theta \; \Delta X_d \tag{4.18}$$

where $\Delta \log E_\tau$, $\Delta\theta$ and ΔX_d are the distances between the points in Figure 4.12. The product of the three defines a volume that is represented by the simulations of this point. For example for $\log(E_\tau/\text{eV}) = 17.5$, $\theta = 90.7°$ and $X_d = 50$ m the corresponding distances are $\Delta \log E_\tau = 0.25$, $\Delta\theta = 0.57° \equiv 0.01$ rad and $\Delta X_d = 50$ m.

We have not included the (unknown) factor k in w_i. So, to be precise, the actual definition of w_i is $k \times w_i$ is the contribution of bin i to the number of events per unit time and area for a diffuse neutrino flux that decreases with energy as E_ν^{-2}.

In Figure 4.13 we show which are the most important bins, i.e. the bins with highest weight that will contribute most to the number of expected events.

The bins which contribute the most to the detection of ν_τ are those with small X_d. There are two reasons for this. The first one is that the probability of a τ decaying high in the atmophere is small for energies of the order of the EeV. This effect is dominant at energies below 10^{18} eV. In Section 7.1.1 we show as an example the efficiency for 10^{18} eV neutrinos entering the Earth at 0.68° below the horizon. At this angle the average decay height is $\lambda_{\text{decay}} = 580$ m. At that height there is still a fraction of showers that trigger the array. For lower energies the λ_{decay} decreases faster than the decay height range where the trigger efficiency is higher than zero. The second reason is that the higher the τ decays the smaller the chance of the particles of the shower to reach the stations of the array. This means that for a high energy τ, even if the probability of decaying high in the atmosphere is non negligible, the trigger efficiency is zero. This is the case for energies above 10^{18} eV.

The weights are concentrated at zenith angles around 91° because of the competition between two effects. As the zenith angle increases the distance travelled through the Earth is larger so the fraction of neutrinos interacting in a range where the induced-tau can emerge from the surface decreases. On the other hand, as the zenith angle decreases the subtended area decreases because of the projection given by the $\cos\theta$ term.

The weights decrease as the energy increases due to the fact that the neutrino flux is suppresed as E^{-2}.

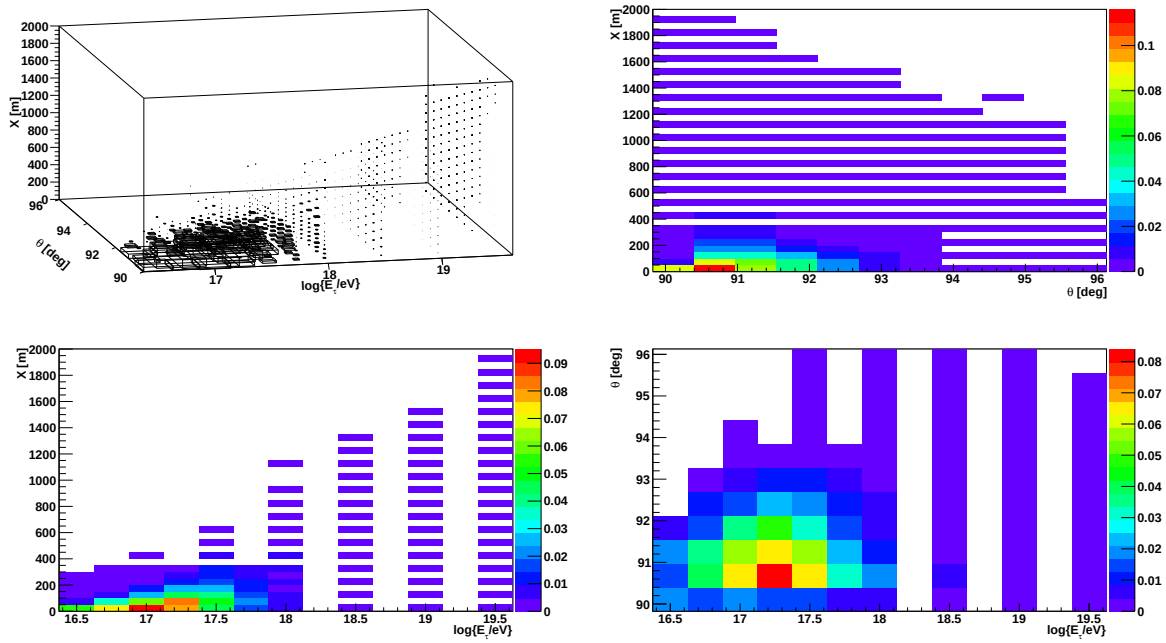

Figure 4.13 *Top left:* The distribution of weights as a function of $\log E_\tau$, θ and X_d. It can be seen that there is a concentration of weight close to $\log E_\tau \approx 17.25$, $\theta \approx 91.25°$ and small values of X_d. *Top right:* Projection of the distribution of weights along E_τ. The result is the distribution of weight as a function of θ and X_d. *Bottom left:* Projection of the distribution of weights along θ. The result is the distribution of weight as a function of $\log E_\tau$ and X_d. *Bottom left:* Projection of the distribution of weights along X_d. The result is the distribution of weight as a function of $\log E_\tau$ and θ.

5

Reconstruction and selection of inclined showers

In this chapter we describe the methodology applied to select good quality events and define a way of identifying inclined showers. Given the fact that real events induced by UHECRs and MC simulations of nearly horizontal showers initiated by τ leptons present singular characteristics, it was necessary to develop a set of algorithms capable of producing good results for both neutrino MC simulations and data samples.

The chapter is organized as follows. In Section 5.1 we present the criteria to select quality events. In Section 5.2 we define the variables to select inclined showers and in Section 5.3 use them to compare neutrino MC simulations to data. In Section 5.4 we summarize the quality and selection criteria.

5.1 Selection of quality events

The procedure starts with a set of events that satisfy the T3 trigger criteria (see Sec.3.1.2) of the surface detector (SD). Within this group, real events acquired during the periods in which the SD is working in a unstable way are discarded [117]. These are known as "Bad Periods". Next, with the aim of obtaining a sample of good quality events, the following sequence of procedures is applied:

1. PMT selection (Sec. 5.1.1).
2. Station selection (Sec. 5.1.2).
3. Preliminary Reconstruction (Sec. 5.1.3).
4. Additional cuts (Sec. 5.1.4).

These are explained in the following sections.

5.1.1 Photomultiplier tube selection

The neutrino search looks for extremely rare events. If a candidate appears it is imperative to be sure that it is not the result of a malfunctioning photomultiplier tube (PMT). We are particularly interested in PMT pathologies that induce a signal artificially extended in time, since, as it will be shown in Chapter 6, we will use the time spread of the signals in inclined showers to identify UHE neutrinos.

There are several reasons for tagging or discarding a PMT. We will separate them into two groups which are explained next.

5.1.1.1 Standard cuts

This set of cuts cuts is the result of studies [118] performed with the monitoring data (see Section3.1.2). Using this data a list of unstable PMTs is provided on a day-to-day basis. The parameters which are studied are the anode and dynode baselines and the dynode/anode ratio.

In the case of the baseline, it is required that their fluctuations should be small, placing a cut on their RMS. The dynode/anode ratio is also requested to have small fluctiantion but, more importantly, even if it is stable there are limits on its maximum and minimum values.

In Figure 5.1 we show an example of the importance of applying these cuts before the selection of neutrino candidates. PMTs 2 and 3 have a saturated anode signal so the signal of the dynode is used[1]. The signal of the dynode in PMT 3 is very different from PMTs 1 and 2. This PMT is disregarded in the analysis because of having a very low dynode/anode ratio. As it will be explained in Chapter 6, neutrinos will be selected by broad signals in time induced in the SD stations. Given that malfunctioning PMT such as the one rejected could induce a fake neutrino candidate this cut is of great importance.

5.1.1.2 Special cuts

When performing studies using not only the integrated charge of the FADC traces, but also their shape, other kind of pathologies in some PMTs become apparent. Most of the times they are the result of an excess of signal in the PMT trace after the signal induced by the shower.

The method to identify this kind of pathology is described next. For each tank, and for each dynode trace, we add up the content of bins 350 to 700. We substract from this sum (Σ_i, where i stands for each PMT) the content of the maximum bin, as well as the bin before and the bin after, to eliminate potential peaks that may be produced by accidental single muons. Then we select stations that verify:

[1] A signal is saturated when in one bin the FADC channel is higher than 1024.

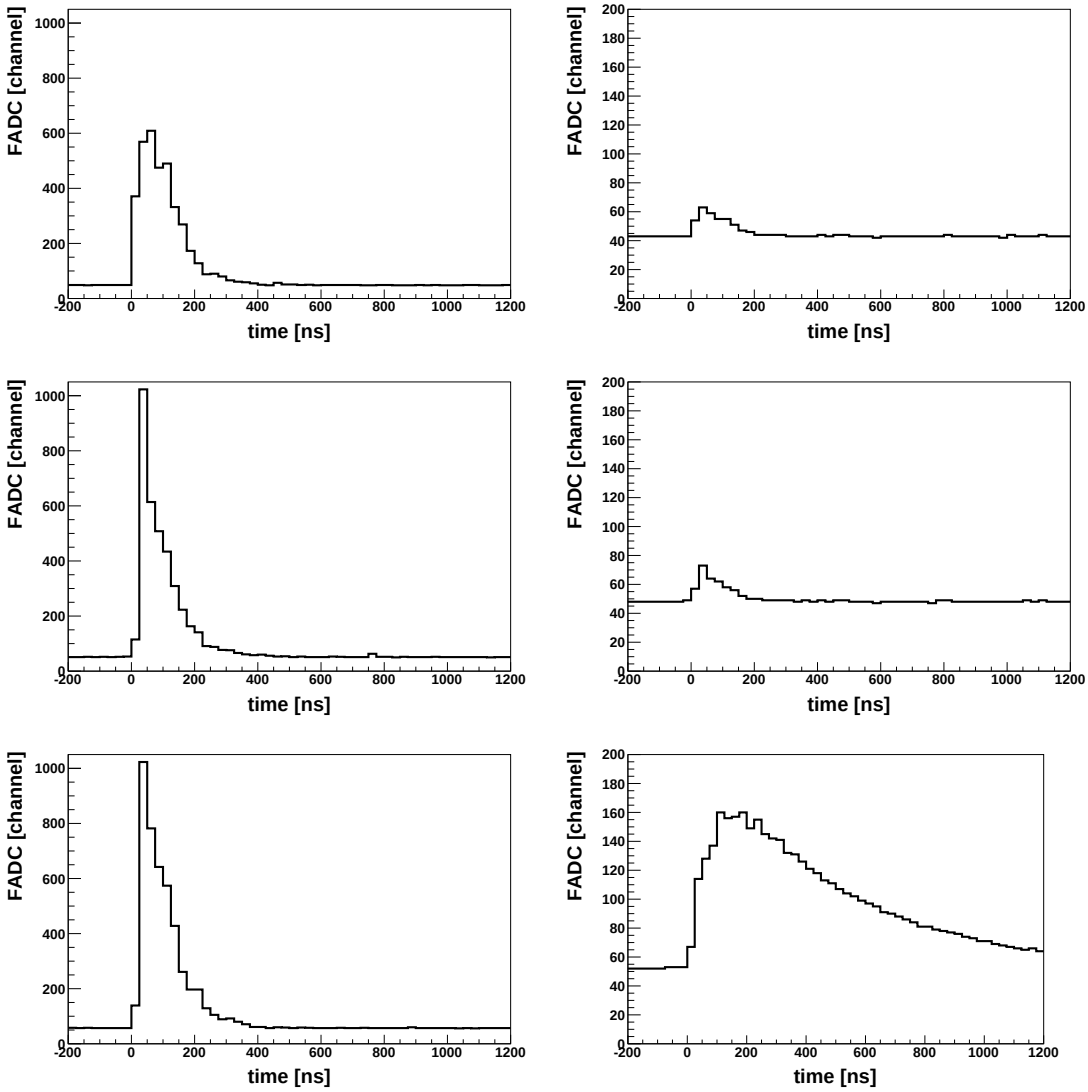

Figure 5.1 Example of a discarded photomultiplier tube. Station 717 (Bobik) from event 1634332 detected on 19 September 2005. From top to bottom PMTs 1, 2 and 3. *Left:* FADC anode signals. *Right:* FADC dynode signals. PMT 3 has a dynode problem and is rejected by the dynode/anode ratio cut (see text).

1. There are at least 2 active PMTs.
2. $\max(\Sigma_i)$ is larger than 4VEMs.
3. The largest Σ_i is at least 7 times larger than the others.

If a given PMT is systematically flagged as satisfying condition 3 over a period of time, it is an indication that it is behaving in an abnormal way. In Figure 5.2 we show an example of this kind of behaviour. This PMT is also removed from the analysis.

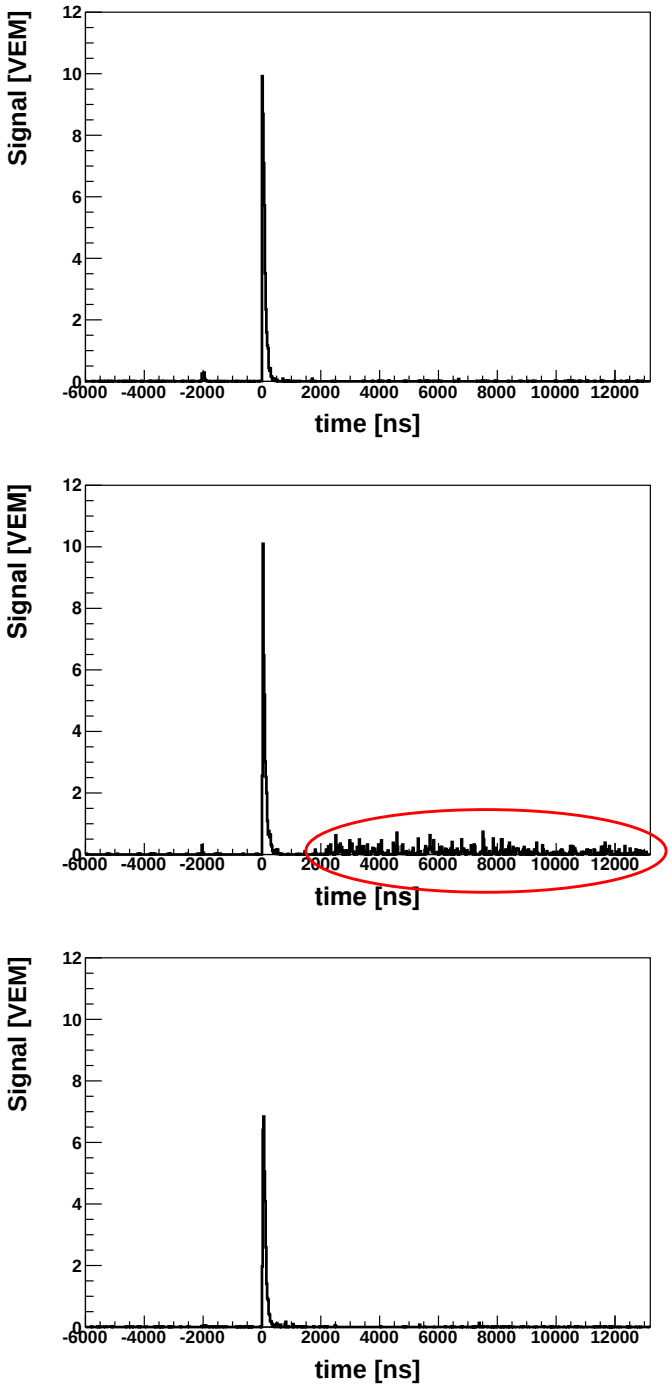

Figure 5.2 Example of a discarded photomultiplier tube after applying the special cut. Station 1440 (Nirvana) from event 3995196 detected on 28 September 2007. From top to bottom: PMTs 1, 2 and 3. PMT 2 has an extended low but significant signal at the end of the trace marked with an ellipse and is discarded during the period of time in which it behaves in that manner, January 2004 to June 2010.

In Table 5.1 we give the list of PMTs and periods when they are removed.

Station ID	PMT	Start date	Start GPS	End date	End GPS
573	2	Nov. 30 2004	785872800	June 6 2006	831319200
764	3	Jan. 1 2004	756950400	Feb 3 2009	917719200
1156	2	Jan. 1 2004	756950400	Nov 6 2008	909964800
1187	2	Jan. 1 2004	756950400	Feb 4 2009	917816400
1286	1	Jan. 1 2004	756950400	Oct 8 2008	907459200
1288	3	Jan. 1 2004	756950400	June 2 2009	917978400
1387	3	Mar 31 2010	952300800	Now	Now
1440	2	Jan. 1 2004	756950400	June 2 2010	896468400

Table 5.1 ID and period of time of discarded PMTs.

5.1.2 Station selection

There are several reasons for tagging or discarding a station. Some of them are having only one PMT, being classified as lightning station or because they are not part of the shower (accidental stations). In the following sections we summarize them.

5.1.2.1 Station with 1 PMT

Every station has 3 PMTs, however, some of these can have a temporary or permanent problem during its lifetime, or be tagged as malfunctioning as we have seen in Section 5.1.1. As the stations are spread over an extended region, some of them are located in places where the access is difficult. In those cases, the replacement can take several months.

If a neutrino candidate appears one needs to be sure that it is not the result of a malfunctioning PMT. To do this we can rely on the confirmation of the signal between PMTs. In the rare cases where there is only 1 working PMT after the quality cuts above, this cross-checking is not possible and the station is rejected.

5.1.2.2 Station with lightning

A possible source of background are lightning strikes. These events are rare and generate an electromagnetic pulse, which causes oscillating signals in the SD stations (see Figure 5.3).

The oscillations in the signal trace are used to rejected stations with lightning. Events with one or more stations classified as lightning are discarded.

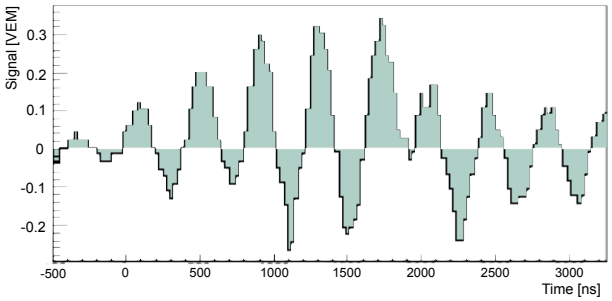

Figure 5.3 Example of a signal generated by lightning. This signal corresponds to event 3995197 (January 26 2005), station 506 and PMT 3.

5.1.2.3 Accidental stations: effects of muon background

The SD is exposed to low energy cosmic radiation much more abundant than the showers produced by UHECR. At the level of the detector (1400 meters above sea level), the radiation is fundamentally composed by low energy atmospheric muons with energies in the 1-10 GeV range. [119]. These particles, which are not part of a shower, can affect the reconstruction basically in two ways:

1. **Produce a T2 trigger in a station which is not part of the event:** the additional T2 trigger time will have a uniform distribution within the 50 μsec window of the T3 trigger. As the inclined selection procedure is based on the position and timing of the triggered stations, the extra station can result in an incorrect estimation of the geometry of the shower. This effect can be particularly important for low multiplicity events. We will see in Section 5.1.3 how these stations are removed.

2. **Add a spurious signal to one of the stations belonging to the event:** if the accidental signal ocurrs only a few μsec before or after the particles of the shower reach the stations, the result is that both signals are merged into the same trace. If the first spurious signal comes firts it fixes the T2 trigger time (see Fig. 5.4) and affects the reconstruction of the event. Even if the spurious signal comes after and does not affect the trigger, it modifies many of the trace observables, such as the AoP, risetime or falltime (see Section 6.2).

In order to minimize the impact of spurious signals produced by accidental low energy muons in stations belonging to the event, the following procedure is applied.

Trace Cleaning Algorithm:

The purpose of the algorithm is the identification and removal of fractions of the trace produced by accidental muons.

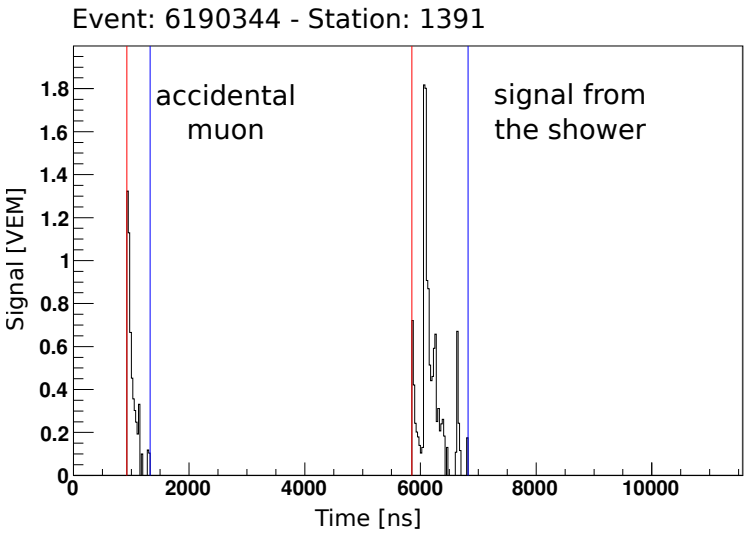

Figure 5.4 Effect of an accidental muon in the determination of the trigger time of the station.

The idea of the method is simple: the amount of energy provided by a muon is, to first order, proportional to its path length in the water inside the station. Given that the SD stations are much wider than taller (1.2 m height vs. 3.6 m diameter), inclined muons produce in average a higher signal than the vertical ones.

Accidental muons are mostly vertical (see Fig. 5.5), so they tend to leave smaller signals than the ones produced by inclined showers. This fact can be exploited to identify fractions of the trace produced by atmospheric muons.

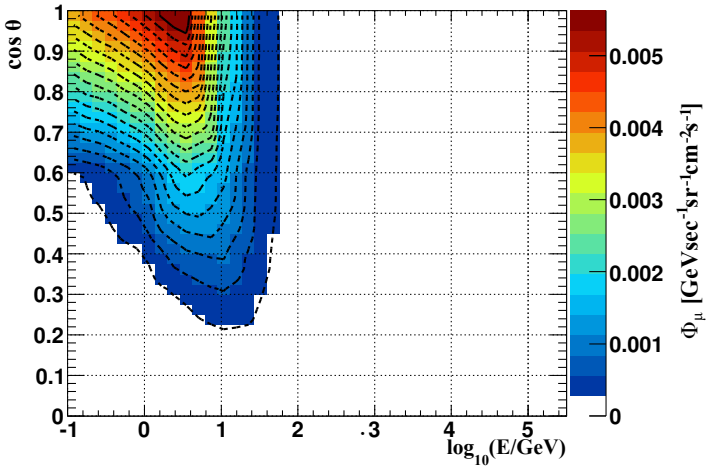

Figure 5.5 Atmospheric muonic flux according to a parametrization given in [119, 120]. It can be observed that roughly $\sim 95\%$ of the total flux arrives at $\theta \geqslant 50°$ ($\cos\theta \geqslant 0.6$).

The current trace cleaning algorithm is described in Reference [121]. It starts at the level of the individual PMTs of a station:

1. Extract signal segments from the full high gain trace of each PMT. A signal segment is defined by at least $n \geq 2$ subsequent bins, where each bin has at least 3 FADC counts above the baseline. Store the start and stop index of the segment, calculate the charge Q and peak signal P.

2. Join segments identified in the first step, for each PMT. Two segments are joined if the gap between them is smaller than 20 bins plus the length in bins of the first segment and at least one of two conditions is met:

   (a) The first segment has a signal $Q_1 > 0.3\ Q_2$, where Q_2 is the signal of the second segment.

   (b) The second segment has a peak signal P of less than 5 FADC counts above the baseline.

   The goal of these conditions is to join segments that are actually induced by the same shower.

3. Merge the signal segments of different PMTs, so that only one set of segments remains. Overlapping pieces between different PMTs are merged by enlarging the time window of the segment and averaging the traces of the overlapping pieces.

4. The start time of the merged trace of the station is determined from the merged segment with the largest integrated signal.

As an example, in Figure 5.4 the algorithm finds two distinct segments. In principle, the segment with the largest integrated signal is kept while the others are rejected.

However, it can happen that two (or more) segments have similar integrated signals. In these cases it is not clear which segment is part of the shower and which has been induced by an accidental muon. For this purpose we apply a second algorithm which selects signals with similar multiple peaks.

The PMT averaged trace is segmented in a similar way as the reported for the individual PMTs. A segment is defined by:

1. The signal starts with the first bin with signal higher than 0.02 VEM.

2. In the next 10 bins (250 ns) the integrated charge Q must be higher than 3 VEM. If not, the beginning of the trace is moved one bin forward until the condition is met.

3. The end of the signal is defined when the next 15 bins all have a signal lower than 0.02 VEM/bin.

4. Two relevant parameters calculated over the segment are:
   (a) $nBoT$: number of bins with signal higher than 0.02 VEM.
   (b) Q_T: sum of the signal over the bins with signal higher than 0.02 VEM.

Every segment has a score defined by $s = nBoT \times Q_T$. The segments induced by atmospheric muons tend to have small values of s compared to the ones with larger values of s, either because they are induced by inclined muons (more intense) or by the electromagnetic component (more extended in time). If there are more than one segment fullfilling that $s > 0.15\, s_{\max}$, with $s_{\max}$ the maximum score, the station is rejected because it cannot be unambiguously decided which of the segments is due to an accidental muon. If not, all segments except the one with $s_{\max}$ are rejected, and the station is kept.

In Figure 5.6 we show an example of a station presenting 3 similar segments. A station like this is removed from the event before applying the inclined reconstruction.

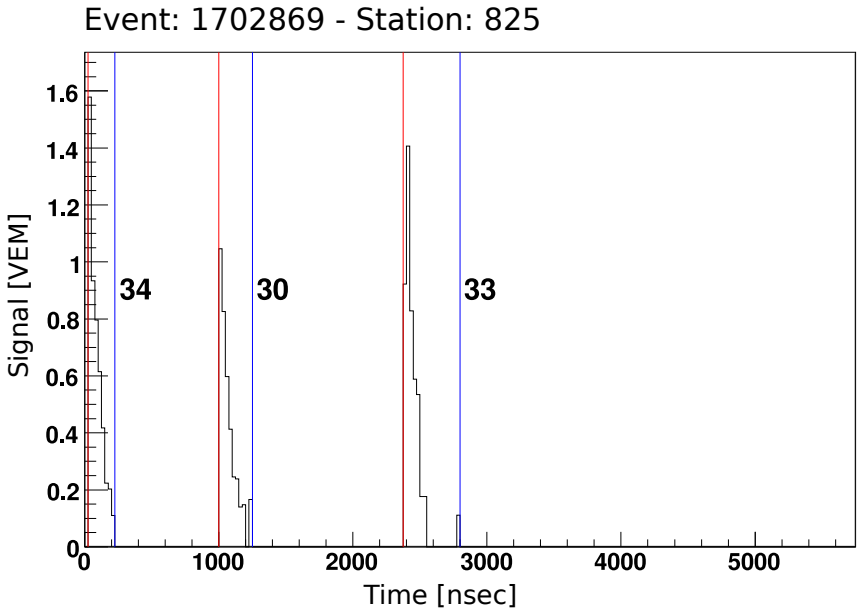

Figure 5.6 Trace presenting multiple signal segments with similar characteristics in which it is not possible to determine the trigger time. The numbers next to each segment indicate the score s assigned to every segment according to the procedure described in the text.

5.1.3 Preliminary reconstruction with accidental station removal

Once the procedure in the previous section is applied, the events are composed by stations with well-defined trigger times. However, events can still contain accidental stations produced by an atmospheric muon or by an independent low energy shower. In order to identify the genuine stations belonging to an event, a selection of stations is carried out based on temporal and spatial compatibility, as explained below. This procedure removes stations based on the global event and not on their individual characteristics.

Isolated Station removal

The first step is to remove isolated stations. Stations are kept only if they satisfy these two conditions:

1. Standard Isolated
   (a) It has at least one station at a distance closer than $d_1 = 4700$ m (third crown) and the difference in trigger times between both stations is compatible with the speed of light ($t_1 < \frac{d_1}{c} \approx 15700$ ns).
   (b) It has a second station at a distance closer than $d_2 = 6200$ m (fourth crown) and the difference in trigger times between both stations is compatible with the speed of light ($t_2 < \frac{d_2}{c} \approx 20700$ ns).
2. Muonic signal: for stations having signals whose $AoP \equiv \frac{S}{S_{peak}} < 1.4$ the criterion is more demanding: at least one neighbour station at a distance closer than $d = 2700$ m is required.

Top-Down Selection

The second step consists in the selection of stations based on spatial and time compatibility. The algorithm for this purpose is an extension of the method known as "top-down" [122]. In this method, the compatibility of a set of N stations with a shower front is analyzed. If this test fails, the compatibility is tried with subsets of $N-1$, $N-2$, .., stations successively until finding a compatible configuration. If 5 or more stations are discarded, the event is discarded because it is considered of bad quality and it could enhance the probability of a bad reconstruction.

The details of the top-down algorithm are presented next.

1. A simple reconstruction of the zenith angle of the event θ_{rec} is performed assuming a plane shower front and an arrival time t_0 defined by the average trigger times of the stations weighted by the signal (barytime). This procedure can be done analytically and does not require a numerical minimization (see Appendix A).

2. The temporal compatibility is evaluated for individual stations and for the whole event:

   - $\Delta t_i < (N-2) \cdot 250\text{ns} \cdot \max(\cos\theta_{rec}, 0.2)$
   - $(\sum \Delta t_i^2)^{1/2} < (N-2) \cdot 200\text{ns} \cdot \max(\cos\theta_{rec}, 0.2)$

   where Δt_i is the difference between the actual trigger time of the station and the time obtained in the plane fit.

   The cuts depend on the multiplicity N and on the reconstructed zenith angle. Due to the curvature of the front, the most distant stations from the axis of the shower present a larger time difference with the reconstructed plane fit (see Fig. 5.7). To take this into account the tolerance grows with the multiplicity of the event.

   The dependence on the zenith angle is introduced for a similar reason: inclined showers go through more matter before reaching the detector. The dependance of the shower front radius with the zenith angle is typically considered to be $R \propto \sec\theta$ [123]. Consequently, high zenith angle shower fronts present a small curvature. For $\cos\theta < 0.2$, which corresponds to $\theta > 80°$, it is assumed that the shower front reaches a minimum curvature and, in this way, Δt reaches a minimum $(N-2)50$ ns.

3. It is also required that the event is spatially compact. The total number of stations projected along the plane of the shower needs to be contained in a circle of radius

$$r_{\max} = \left(\frac{1300}{\text{m}}\right)^2 \times (N-2)$$

   where N is the multiplicity of the event.

4. The T3 trigger condition is satisfied.

5. If the event does not satisfy all of the above conditions, the algorithm is applied to subsets of $N-1$, $N-2$, .., stations successively until a configuration is found satisfying the above conditions. The order in which the configurations are evaluated is determined first by the multiplicity (one tries to remove the minimum number of stations) and second, within a fixed number of stations, by the signal size, attempting to remove first the ones with lowest signal.

When all stations in an event are aligned it is not possible to perform the mentioned reconstruction. Instead, the apparent velocity of the signal V_{ij} is calculated between all pair of stations (i, j) with a T2 trigger:

$$V_{ij} = \frac{d_{ij}}{\Delta t_{ij}} \tag{5.1}$$

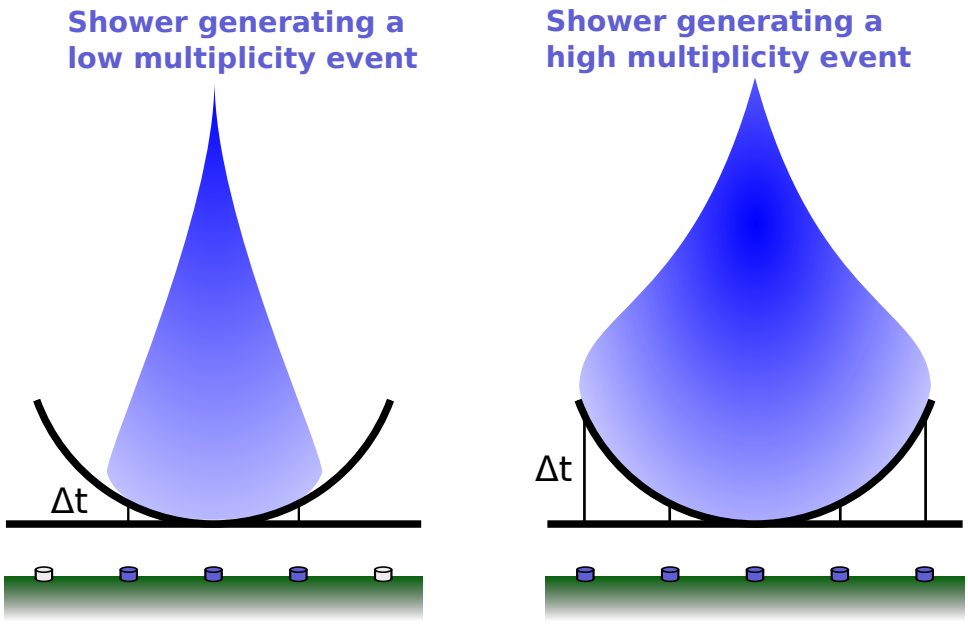

Figure 5.7 Scheme of the time difference between a curved front and the plane front approximation. In showers with large number of triggered stations (right panel) the time difference between the actual trigger time and the time obtained in the plane fit tends to be larger than in small multiplicity events (left panel), particularly for stations far from the shower core.

where d_{ij} is the distance between the two of stations and Δt_{ij} their time difference. From the values of V_{ij} the average velocity is computed $\langle V \rangle$ and the following timing compatibility condition is imposed between all pair of stations:

$$\frac{V_{ij} - \langle V \rangle}{\langle V \rangle} < 0.1 \tag{5.2}$$

Aligned events are of great importance in the search for UHEνs as they consititute $\sim$60% of the events in the MC simulations.

5.1.4 Additional selection

Once the stations belonging to an event are defined we perform two additional tests to select good quality events.

1. `IsContained`: The barycenter of the event is calculated weighting the stations with their signals and the station closer to it is selected. If that station has less than 5 active stations around it the event is rejected. This criterion is only applied to events with less than 6 stations. The purpose is to avoid small multiplicity events close to the borders of the array. These could be part of

a higher multiplicity event where the core fell outside the array, and hence a large fraction of the event is missing.

2. `hottestHasNeighbour`: It is required that the station with the highest signal has at least one station with signal in the surrounding crown of stations. If the condition is not met the event is rejected.

5.2 Variables for selection of inclined showers

In this section we define the two variables used to select inclined events: the length over width of the footprint, L/W, and the velocity at ground, $\langle V \rangle$.

5.2.1 Event footprint

The pattern of stations with signal in inclined events produces elongated footprints on the SD. This property can be characterized by constructing a "signal moment tensor":

$$\begin{aligned} S = \sum_i s_i, \quad \langle X \rangle = \sum_i s_i x_i / S, \quad \langle Y \rangle = \sum_i s_i y_i / S \\ I_{xx} = \sum_i s_i (x_i - \langle X \rangle)^2 / S, \quad I_{yy} = \sum_i s_i (y_i - \langle Y \rangle)^2 / S \\ I_{xy} = I_{yx} = \sum_i s_i (x_i - \langle X \rangle)(y_i - \langle Y \rangle) / S \end{aligned} \tag{5.3}$$

This object describes the spatial distribution of signal in the same way as the inertia tensor does with the mass. Following the analogy (see Fig. 5.8)[2] one can obtain the size of the principal axis of the elliptically-shaped footprint as:

$$\begin{aligned} L^2 = \frac{I_{xx} + I_{yy} + \sqrt{(I_{xx} - I_{yy})^2 + I_{xy}^2}}{2} \\ W^2 = \frac{I_{xx} + I_{yy} - \sqrt{(I_{xx} - I_{yy})^2 + I_{xy}^2}}{2} \end{aligned} \tag{5.4}$$

where L (Length) and W (Width) correspond respectively to the size of the major and minor axes.

It is possible that a vertical shower together with an accidental station gives a $\langle V \rangle$ consistent with an inclined shower. However, these events don't have an elongated footprint. In this way, the ratio L/W can be used as a quality criterion to select inclined events.

[2] To calculate the ellipse, W and L we use all T1 stations.

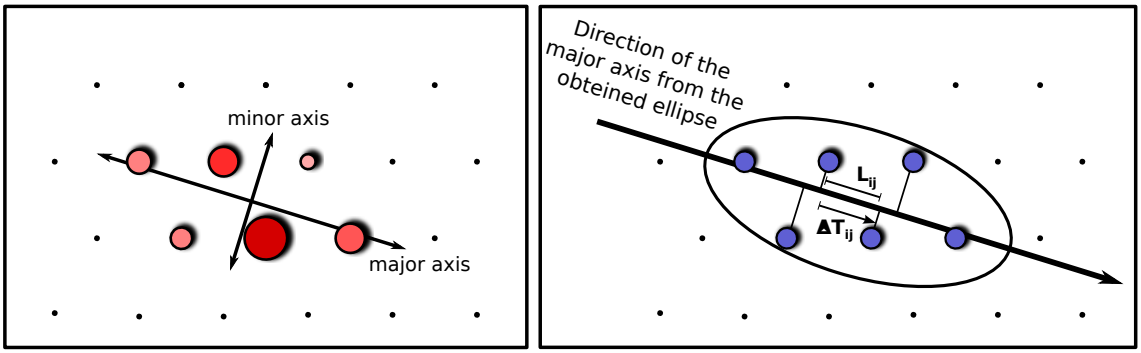

Figure 5.8 Left: Sketch of the elliptically-shaped footprint of the shower that represents the spatial configuration of an inclined event. **Right:** Sketch showing the calculation of the apparent signal speed V_{ij} between stations i and j.

5.2.2 Ground speed

In an inclined event, the axis of the shower is almost parallel to the direction of the major axis of the ellipse. In this way the signal speed at the ground (V) along this direction gives a good approximation to the zenith angle.

$$\sin\theta \simeq \frac{\langle V \rangle}{c} \tag{5.5}$$

In order to estimate $\langle V \rangle$ for an event, one averages the pairs of velocities $V_{ij} \equiv L_{ij}/\Delta T_{ij}$ between stations whose relative distance, projected along the major axis, L_{ij}, is larger than 1000 m (see right panel of Fig. 5.8)[3]. One does not consider pairs of stations with distances $L_{ij} < 1000$ m to avoid V_{ij} values with large uncertainty due to the fluctuations in the trigger time of the stations.

5.3 Performance of the inclined shower selection

In this section we compare the ν MC sample with the data sample. The purpose is to analize the variables described in the previous Section for both samples. Then we define the selection cuts and, finally, we evaluate the performance and efficiency of the inclined shower selection. The procedure will treat 3 stations events separately from the rest.

For reference, the sum of weights, defined in Section 4.3, for events with 4 stations or more, amounts to $\sim 70\%$, while events with 3 stations account for $\sim 30\%$.

[3]To calculate the ground speed velocity we use only T2 stations.

5.3.1 Events with 4 stations or more

The inclined selection criteria for events with 4 stations or more are:

- $\frac{L}{W} > 5$
- $0.29 \frac{\text{m}}{\text{ns}} < \langle V \rangle < 0.31 \frac{\text{m}}{\text{ns}}$
- $\text{RMS}(V) < 0.08 \frac{\text{m}}{\text{ns}}$

In Figures 5.9, 5.10 and 5.11 we respectively show the distributions of W/L, $\langle V \rangle$ and $\text{RMS}(V)$ for data from 1 January 2004 up to 31 October 2007 as well as for the simulated neutrino events. We also show the values of the cuts and the region selected. The plots illustrate that the Inclined Shower Selection above keeps most of the MC events.

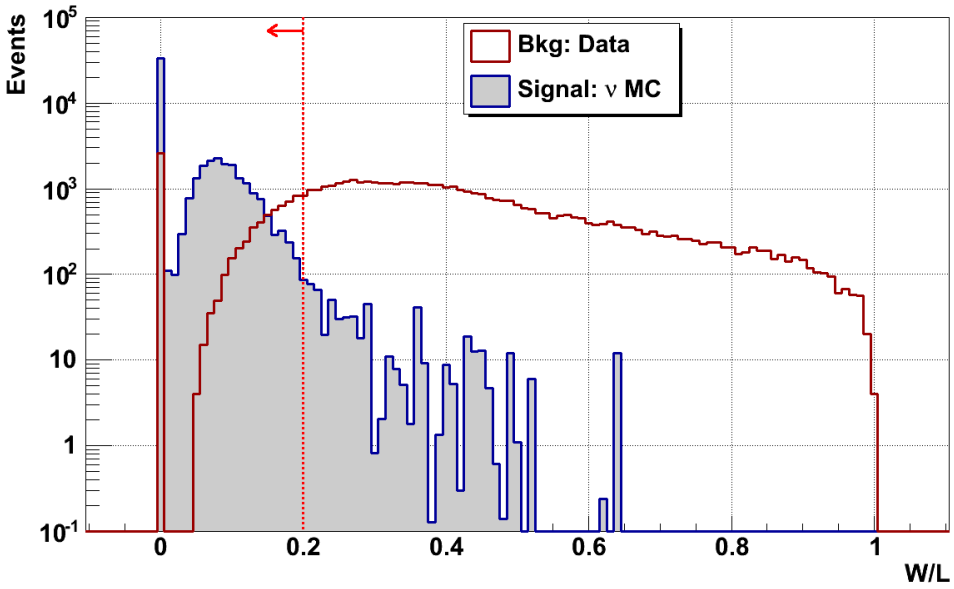

Figure 5.9 Distribution of W/L in data and in MC simulations of ES ν_τ-induced events. The vertical dotted line corresponds to the cut applied in the Inclined Selection at $W/L < 0.2$ (or equivalently $L/W > 5$). We have applied a relaxed cut on $\langle V \rangle < 0.35 \frac{\text{m}}{\text{ns}}$. Notice that we have plotted W/L instead of L/W because aligned events have an infinite value of L/W (zero value of W/L).

5.3.2 Events with 3 stations

The sum of the weights, defined in Section 4.3, for 3-station events is ∼30%. This non-negligible contribution to the expected yield makes it important to design a criterion to efficiently select these events.

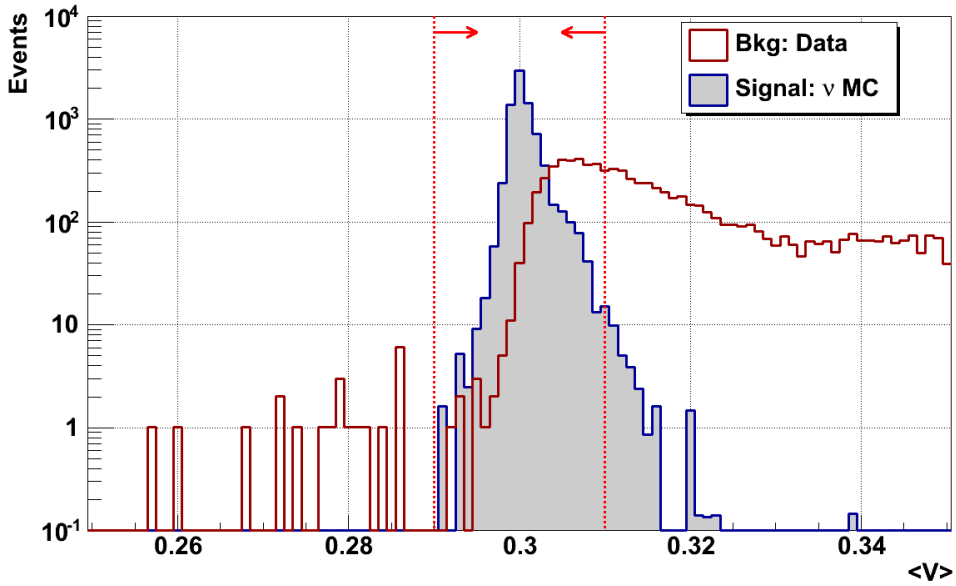

Figure 5.10 Distribution of $\langle V \rangle$ in data and in MC simulations of ES ν_τ-induced events. A cut $W/L < 0.2$ is applied to both data and simulations. The vertical dotted lines correspond to the Inclined Selection cuts at $0.29 < \langle V \rangle < 0.31$ m/ns.

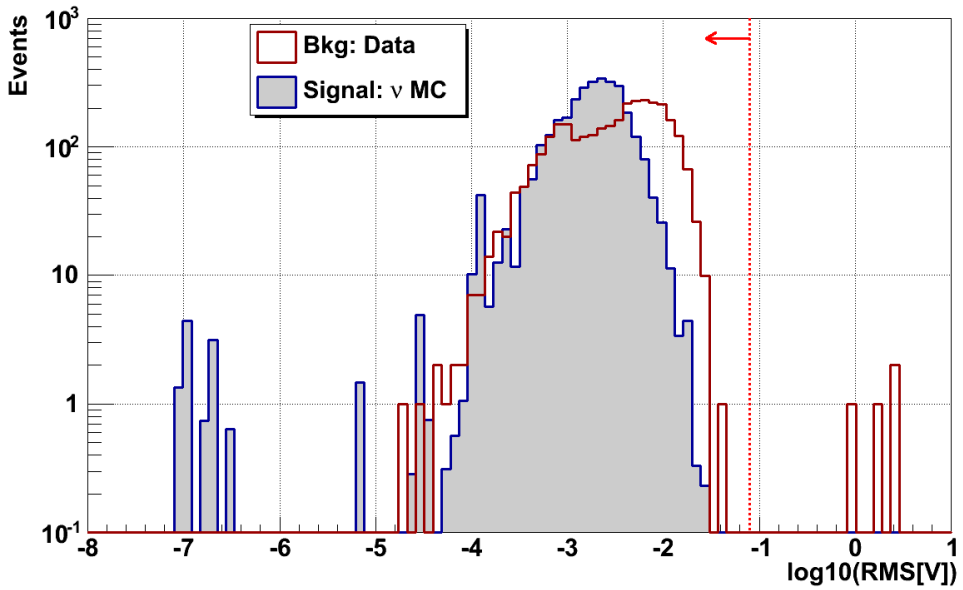

Figure 5.11 Distribution of $\log_{10} RMS(V)$ in data and in MC simulations of ES ν_τ-induced events. The cuts $W/L < 0.2$ and $0.29 \leq V \leq 0.31$ are applied to both data and simulations. The vertical dotted line represents the cut at RMS$(V)< 0.08$ m/ns.

The number of possible 3-station configurations that can satisfy the geometrical requirement of a T3 trigger is only 7. In Fig. 5.12 we show a sketch of these 7 configurations. In this Section we study the effects of replacing the cut on L/W for 3-station events with a selection of only certain configurations among the 7 possible ones. Ideally, one would like to keep those configurations that contribute most to the total yield but at the same time to eliminate those that are prone to induce fake neutrino candidates in data.

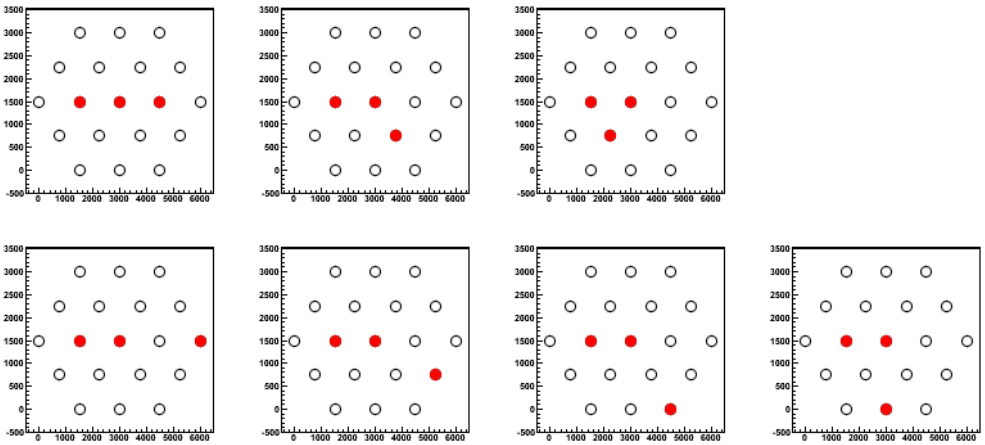

Figure 5.12 Sketches of the 7 possible T3 configurations for 3-station events. Full circles indicate the triggered stations. **Top:** From left to right: configurations number 1 to 3. **Bottom:** From left to right: configurations number 4 to 7.

In Table 5.2 we show the frequency of appearance in the MC neutrino sample at trigger level, of the configurations shown in Fig. 5.12. At trigger level the dominant configurations turn out to be numbers 1 and 5.

After applying the quality selection criteria defined in Section 5.1 the number of events belonging to each one of the 3-station configurations can change mainly for two reasons. Firstly, there are 3-station events that do not pass the criteria. Secondly, events with more than 3 stations can lose some of them and become 3-station events. Note, in fact, that the number od 3-station events increases after applying the quality ctus. In Table 5.3 we show the frequency of appearance of the configurations in Fig. 5.12 after the quality selection criteria are applied.

Tables 5.2 and 5.3 show similar results. In both cases, the two dominant configurations are numbers 1 and 5. The reasons why the other configurations do not appear in simulations as frequently as these are:

- Configurations 2 and 3 are too compact and wide. ES neutrinos typically have very elongated footprints so if the event is wide enough to trigger these stations, it will most probably trigger also more stations along the direction of the shower.

Config. number	Triggered MC Events	Percent	Percent in weight
Total	3258	100%	100%
1	1753	53.8%	70.2%
2	104	3.2%	0.6%
3	5	0.2%	<0.1%
4	191	5.9%	3.1%
5	1181	36.2%	26.0%
6	17	0.5%	<0.1%
7	7	0.2%	<0.1%

Table 5.2 The frequency of appearance at trigger level of each of the 7 possible 3-station configurations in the MC sample of simulated ES tau neutrinos. The first column shows the configuration number. In the second we give the number of Monte Carlo events in each configuration. In the third we show the fraction of MC events and in the fourth the percentage contribution to the expected yield.

Config. number	Selected MC Events	Percent	Percent in weight	DATA 1 Jan 04 - 31 Oct 07
Total	3562	100%	100%	10329
1	1993	56.0%	70.8%	1378
2	132	3.7%	0.5%	1895
3	3	<0.1%	<0.1%	6358
4	142	4.0%	1.8%	82
5	1278	35.9%	26.9%	378
6	8	0.2%	<0.1%	38
7	9	0.2%	<0.1%	200

Table 5.3 The frequency of appearance of the configurations shown in Figure 5.12 in the MC sample of simulated ES τ neutrinos after the quality selection criteria are applied. The number of MC events in each configuration, their frequency of appearance, and their contribution to the expected yield, are show in columns 2-4. In the fifth we show the number of events in data belonging to each configuration after the same cuts applied to MC simulations.

- Configurations 6 and 7 are not present mainly because it is not very likely to have a missing station within the triangle defined by the three stations.

- Configuration 4 is the third one in abundance. This is reasonable given the fact that it is an aligned configuration, as typical in ES neutrino events, but also suppressed by the fact that there is a missing station in the middle.

Now we concentrate on MC neutrino events inducing configurations 1 and 5. In the left panel of Figure 5.13 one can see the distribution of the azimuthal angles of the events that belong to configuration 1. There are 6 clear peaks in the distribution,

as expected, at azimuths -120°, -60°,- 0°, 60°, 120° and 180°. For each peak one can also see a clear 2-peak substructure. The reason for this is that the more aligned the event, the larger the probability of triggering more stations and hence the event would no longer contribute to the distribution of 3-station events. This is confirmed when plotting in the right panel of Fig. 5.13 the distribution of azimuth angle for aligned events regardless of their number of stations. In this case there are events very close to $\phi = \phi_0$, as expected.

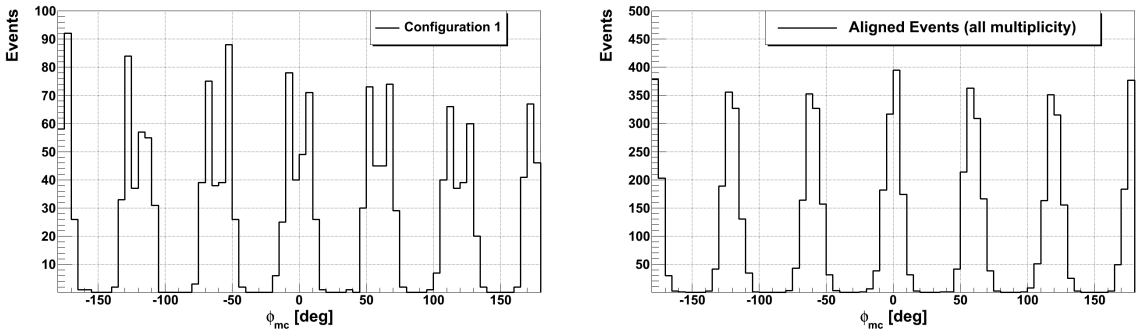

Figure 5.13 Left: Azimuth distribution of simulated 3-station MC neutrino events belonging to configuration 1. There are 6 clear peaks at -120°, -60°,- 0°, 60°, 120° and 180° with a lack of events close to the central values (see text for explanation of this effect). **Right:** Distribution of azimuthal angles for aligned MC neutrino events regardless of the number of stations in the events.

A similar effect can be seen for the case of configuration 5. Before looking at the azimuthal distribution let us consider the 12 possibilities. These are sketched in Fig. 5.14. and denoted 5.1 to 5.12. One can see that realizations with odd decimal numbers (1, 3, 5, 7, 9, 11) are rotations by 60° of realization 5.1. Similarly realizations with even decimal numbers are 60° rotations of realization 5.2.

In Figure 5.15 we plot the distribution of azimuthal angles for MC neutrino events that belong to configuration 5. There are 12 clear peaks at azimuthal angles ϕ_0 =-160°,-140°,-100°,-80°,-40°,-20°, 20°, 40°, 80°, 100°, 140° and 160° as expected from inspection of Figure 5.14.

Selection of 3-station event topologies

Clearly from the point of view of maintaining a large efficiency, while at the same time eliminating possible 3-station background events, it is not worth keeping configurations 2, 3, 4, 6 and 7 since they contribute very little to the efficiency (see Table 5.3). Moreover, configurations 2 and 3 are very frequent in background.

Configuration 1, on the other hand, clearly has to be selected as it is the dominant topology. The dilemma is whether to choose also configuration 5.

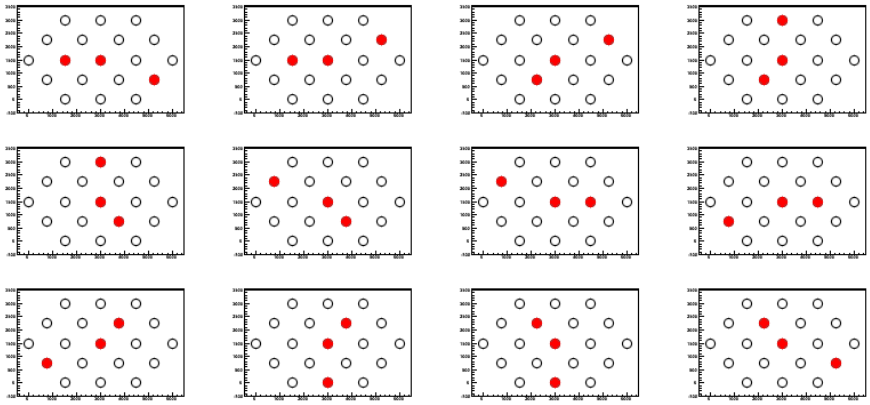

Figure 5.14 Sketches showing the 12 possible realizations of configuration 5. The full circles indicate the triggered stations. **Top:** From left to right: realizations 5.1 to 5.4. **Middle:** From left to right: realizations 5.5 to 5.8. **Bottom:** From left to right: realizations 5.9 to 5.12.

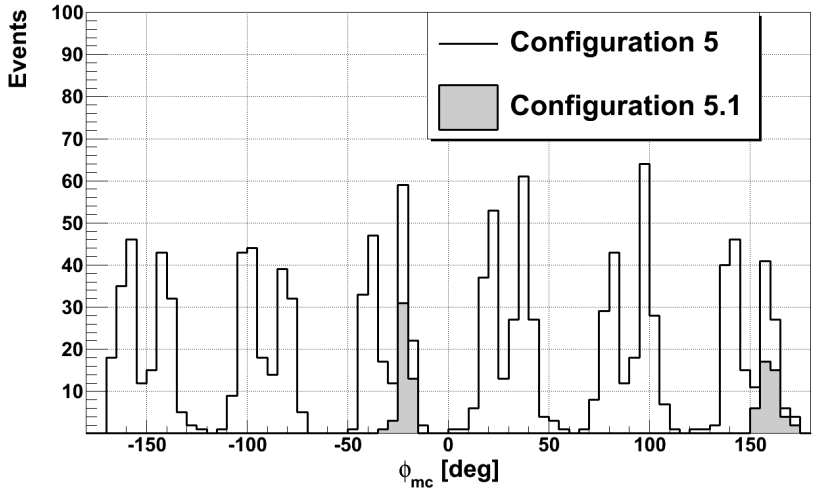

Figure 5.15 Distribution of azimuthal angles for MC neutrino events belonging to configuration 5 (blue histogram). Red histogram: same as blue histogram but only for the configuration 5.1 (see Fig. 5.14). One can see that configuration 5.1 only contributes to angles around -20° and 160°. The other configuration contributing to these peaks is configuration 5.7, which is a 180° rotation of 5.1.

The first neutrino event at this high energies should be convincing enough to the astroparticle community. Since a non-aligned 3-station event does not have angle reconstruction redundancy, non-connected candidate events, such as configuration 5, would be met with skepticism. Moreover, since the gain in efficiency by including configuration 5 is not decisive (8%) in this work we decided not to use this topology, at least in the discovery phase.

5.4 Summary

In Table 5.4 we display the quality and inclined selection criteria used in the analysis.

	`nStation` ≥ 4	`nStation` $= 3$
Quality Cuts	Remove: ◦ Bad PMTs ◦ Stations with only 1 active PMT ◦ Lightning events ◦ Stations with multiple peaks of similar signal ◦ Stations not satisfying preliminary reconstruction ◦ Events not passing `IsContained` requirement ◦ Events not passing `hottestHasNeighbour` requirement	
Inclined Showers	$L/W > 5$	Geom. config. 1
	0.29 m ns$^{-1} < \langle V \rangle < 0.31$ m ns^{-1} RMS$(V) < 0.08$ m ns^{-1}	

Table 5.4 Observables and numerical values of cuts applied to select good quality and inclined showers.

In Table 5.5 we report the MC efficiency and the number of events remaining in data after applying the selection criteria.

	`nStation` ≥ 4		`nStation` $= 3$		`Total`	
	MC Eff.	Data	MC Eff.	Data	MC Eff.	Data
Quality Cuts	65.9%	42103	28.3%	10329	94.2%	52432
$L/W > 5$ || Config. 1	65.5%	6442	20.0%	1378	85.5%	7820
$0.29 \frac{\text{m}}{\text{ns}} < \langle V \rangle < 0.31 \frac{\text{m}}{\text{ns}}$ RMS$(\langle V \rangle) < 0.08$ m ns^{-1}	65.5%	3207	19.7%	23	85.2%	3230

Table 5.5 The first column gives the selection criteria applied. We divide the samples according to the number of stations. In the case of neutrino MC showers, we show the efficiency with respect to the total T3 trigger events. For data the number of events is shown.

6

Neutrino identification

In the previous chapter we have discussed the selection of good quality inclined showers. In this chapter we analyze the identification of showers generated by τ leptons emerging from the Earth in the presence of the dominant background of hadronic showers.

In order to avoid biases in the analysis, this work adopted a "blind search" scheme. Roodman [124] defines a blind search as one whose methodology and tools are developed before performing the measurement. Within this framework the analysis reduces the possible biases coming from the prejudices a researcher may have due to theoretical reasons or results from previous experiments.

The development of identification algorithms requires the knowledge of the features that distinguish signal from background showers. Since until now no neutrinos have been found, we have to rely on MC simulations to characterize signal events.

For background, on the other hand, we have the choice of using actual data or a simulation of hadronic showers. There are several reasons to choose the former. In the first place, since the cosmic ray spectrum falls as E^{-3}, the background will be mainly composed of hadronic showers at the lowest energies than trigger the array. The trigger efficiency itself decreases at low energies, with $\varepsilon_{\text{trig}} < 1\%$ at energies below $10^{18.5}$ eV and zenith angles higher than 80°. The simulation of the background would thus require the generation of more than 100 events for each shower accepted in the final sample. In the second place, even if the generation of such a huge number of showers were feasible, the hadronic showers most likely to be confused with neutrinos are those with extreme or abnormal behaviour of the detector, characteristics that are most probably not included in the simulation.

The data themselves, on the other hand, are an excellent model for the background. They are overwhelmingly (if not totally) constituted by hadronic events,

and they contain, of course, the most capricious behaviours of the detector components. The only concern is that they might contain an actual neutrino event. This is not a problem, however, as a few events will not alter the distributions of the observables needed for the characterization. And if a particularly suspicious event is found, it can eventually be removed from the sample used to define the identification criteria.

This Chapter is organized as follows. Section 6.1 discusses the subdivision of the Observatory data to accomplish the dual role of ingredient in the identification criteria and search sample for neutrino events. Section 6.2 presents the variables with discrimination potential, Section 6.3 reviews the previous earth-skimming analysis, and in Section 6.4 the new selection scheme is developped. The estimation of the background and the testing of the selection criteria are the subjects of Sections 6.5 and 6.6.2, respectively.

6.1 Subdivision of the data sample

The procedure for defining a neutrino selection requires independent data samples that will play different roles in the analysis. We divide the data into three samples defined by the time in which they were acquired as it can be seen in Figure 6.1. The purpose of each sample is defined next.

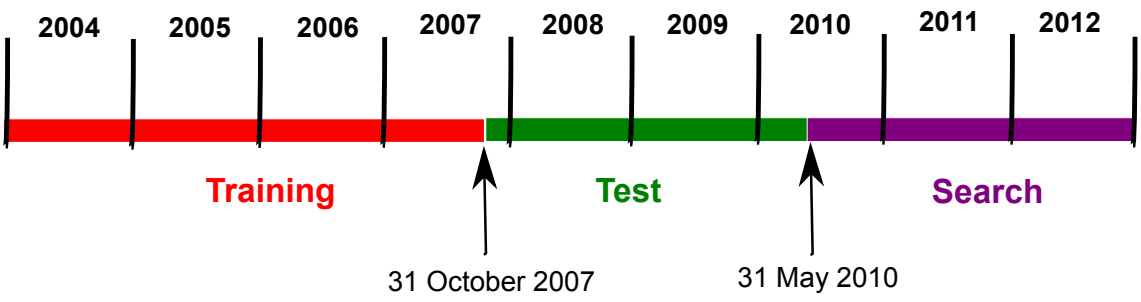

Figure 6.1 Scheme of the *Training*, *Test* and *Search* data periods used in this analysis. See text for definitions.

- **Training data sample**

  It is used to establish and optimize the neutrino identification criteria. Selection algorithms can be tuned as many times as needed exploiting the training data in order to remove all events in this sample. It also allows to characterize the detector effects that are not contemplated in the MC simulations.

  This should be a sufficiently large sample so that it represents the bulk of data to be analyzed.

The Pierre Auger Collaboration has already used data from January 2004 to May 2010 to search for ν candidates [77]. This period is now used to define new selection criteria. The old selection criteria used for the unblinding of this period is discussed in Section 6.3.

For historical reasons (same training sample as in the analysis of down-going neutrinos interacting deep in the atmosphere [75]) we use data from 1 January 2004 up to 31 October 07 as training. This sample is equivalent to the exposure that the complete SD would have accumulated if it had been working continuously for ∼1.4 years without disruption.

- **Test data sample**

  A standard procedure is to define an independent data sample which is not used for training of the algorithms, but can serve as a control of the performance of the selection. In particular, it can test for overtraining. Ideally with this "test data sample" one can verify if the distributions of the variables used for young shower identification behave as in the training data sample. With the test sample one can further tune the selection in case there appear candidates or anomalies in the tail of the distributions of the young shower selection variables that cannot be attributed to neutrino events. However, unlike the case of the training sample, the retuning of the selection can only be done once, if not the test sample would become a new training sample.

  The period of data from 1 November 2007 up to 31 May 2010 is ideal to be used as test data sample. This data period has already been unblinded with the previous ES selection [77] and cannot be used to perform a blind search of neutrino candidates, however it is still useful to perform an independent test of the selection procedure.

  This sample is equivalent to the exposure that the complete SD would have accumulated in ∼2 years without disruption.

- **Search data sample**

  Finally, for the "search data sample" where the ES selection algorithms defined in this work are applied blindly, we use the data period from 1 June 2010 up to 31 December 2012. This set of events is not processed until the identification criteria are fully designed and the procedure is fixed.

  This sample is equivalent to the exposure that the complete SD would have accumulated if it had been working continuously for ∼2.3 years without any disruption.

6.2 Selection: Idea and potential variables

In Chapter 2 we discussed that inclined hadronic showers are dominated by the muonic component while inclined neutrino induced showers present a significant amount of electromagnetic (EM) component at the level of the surface detector stations (young showers). In the case of DG neutrinos the EM component is concentrated in the region of the ground where the event hits first (the so-called early region). On the other hand, Earth-skimming neutrinos which are expected to be observed through the decay of an emerging τ have an EM component in all stations. This is ilustrated on Figure 6.2 and is supported with MC simulations, as it will be shown in Section 6.4.

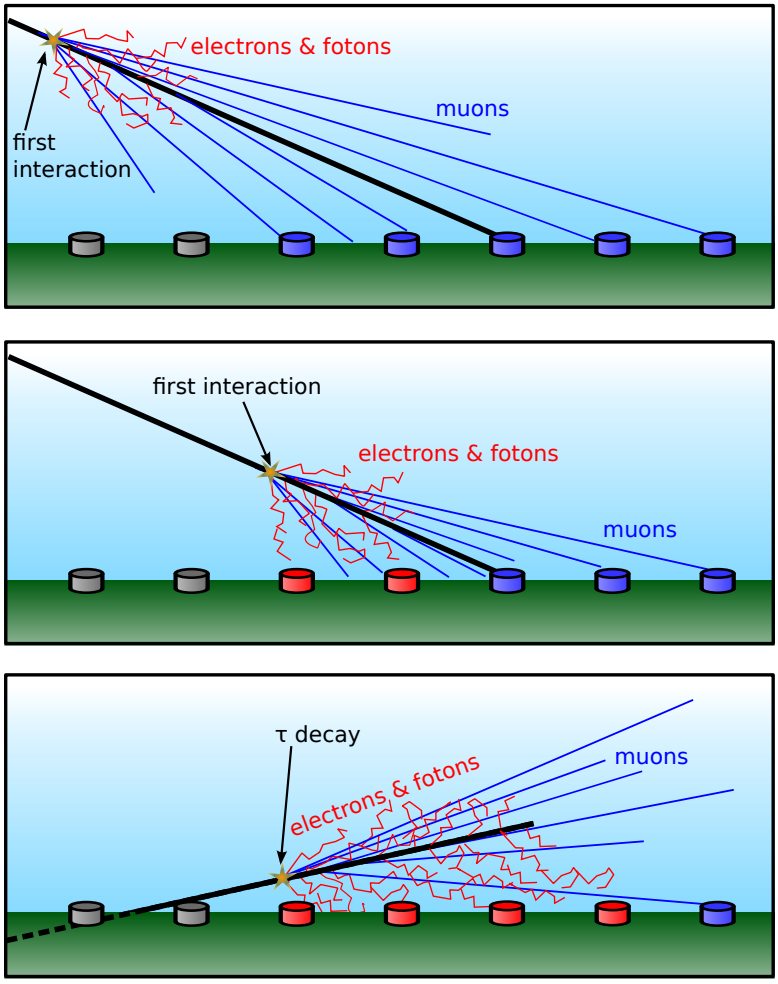

Figure 6.2 *Top:* Scheme of an inclined shower initiated by a hadron which interacts high in the atmosphere. *Middle:* Deep shower initiated by a DG neutrino. The early region presents a significant EM component when reaching the detector. *Bottom* Shower generated by the decay of a τ emerging from the Earth. The EM component is present along all stations.

Consequently, the idea of detecting neutrinos is to look for inclined showers with EM component at ground. We have already defined the inclined selection in Chapter 5 so now we proceed to select events with high electromagnetic component within this sample.

The stations having EM component typically have signals with a duration of the order of few hundred of nanoseconds. On the contrary, stations that are only reached by muons exhibit signals that extend for tens of nanoseconds.

The basic idea to identify stations hit by a significant electromagnetic component is simple. We use the trace of the FADC to construct observables correlated with the time structure of the signal. Several variables related to the time structure of the signal are expected to show differences between EM and muonic traces (see Fig. 3.6). Next, we summarize some of the observables which were studied.

- **Number of ToT station:** In Section 3.1.2 we have discussed that typically short (extended) signals have a T2 (ToT) trigger. Consequently, a very simple idea to identify neutrinos is to count the number of ToT stations or use the ratio between the number of T2 and ToT. The disadvantage of this variable is that their distributions are very difficult to use when trying to estimate the expected background.
- **RT/FT:** The risetime and falltime are defined as the time it takes a signal to go from 10% to 50% and from 50% to 90% of the total value. They have as an evident advantage the fact that they are directly correlated with the physical magnitude that we want to measure (duration of the signal). Both variables show discrimination between hadronic and neutrino showers. On the other hand, their distributions present long non-exponential tails which make them unsuitable for ν searches because background showers induced by UHECRs can be missidentified as ν candidates (see Figure 6.3). Moreover, we have seen in Section 5.1.1.2 that there are PMTs showing anomalies after a physical signal. This anomalies would result in an overestimation of the fall time if, by chance, the PMT is not rejected.
- **AoP:** the area divided by the peak of the signal is denoted AoP. This magnitude is defined as the ratio between the integral of the FADC trace and the maximum value (see Fig. 6.4). It is calibrated so that a vertical muon has AoP=1. EM signals, extended over time, have higher values of AoP than the ones produced by muon fronts, of short duration. As shown in Figure 6.5 there is a rather good separation between the training data and the ν simulations, and, more importantly, the distribution in data does not present very long tails extended towards the region where the ν simulations are concentrated. The same is true for the AoP of other stations in the events. The possibility to missidentify an UHECR-induced shower as a ν candidate is smaller than in the case of RT and FT. Also in Figure 6.5 we show that the variable AoP is very correlated to FT. The same happens with RT.

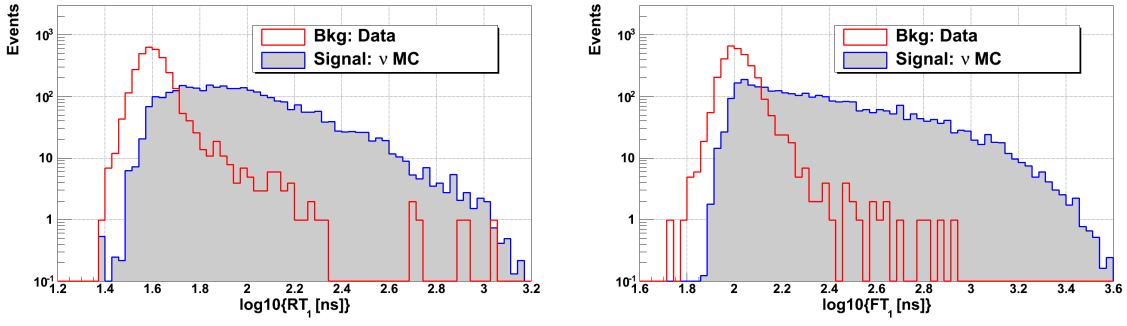

Figure 6.3 Distributions of $\log_{10}$ RT (risetime) and $\log_{10}$ FT (falltime) of the first station for training data and neutrino MC induced showers.

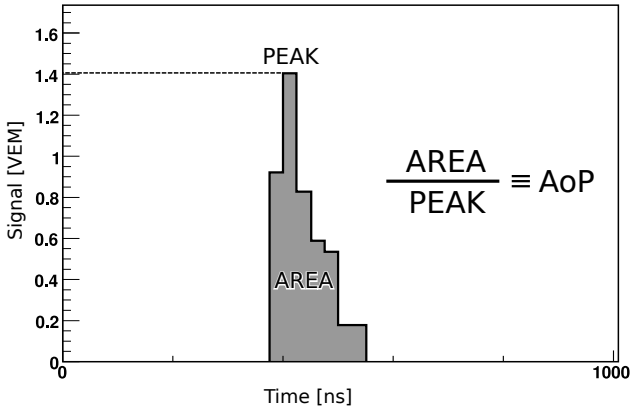

Figure 6.4 Definition of the discriminating variable AoP.

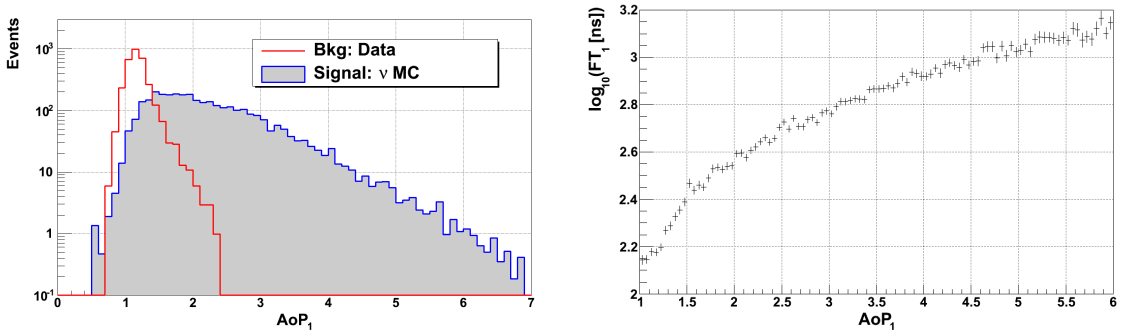

Figure 6.5 *Left:* Distribution of area over peak of the first station. *Right:* Profile distribution of the correlation between AoP and $\log_{10}$ FT.

- **ToTF:** It is possible to combine some of the previous variables. For example, the TOTF (ToT fraction) is the ratio between ToT stations having AoP≥1.4 over the total number of T2 stations. Although, this variable is very powerful, it still has the disadvantage of having a distribution which is difficult to use when trying to estimate the expected background, as it will be seen in Section 6.3.

6.3 Selection of young showers: previous analysis

In this section we review the ES selection of young showers applied in the previous analysis (Section 1.3.3) to data up to 31 May 2010 (Old ES selection). It must be noticed that the inclined selection is basically the same with one main difference: it applies the L/W criterion also for 3-station events instead of selecting only configuration 1. The young shower selection variables and cuts used are the following.

- Number of stations with ToT trigger and AoP>1.4: `nOfflineToT`≥ 3
- `IsT4Nu`: true if there are 3 stations with AoP>1.4 in the event and at least 3 velocities between pairs of stations satisfying $0.285\ \frac{\mathrm{m}}{\mathrm{ns}} < V_{ij} < 0.31\ \frac{\mathrm{m}}{\mathrm{ns}}$. This actually is a combination of young and inclined selection together.
- ToTF > 0.6

Throughout this section we use data from 1 Jan 04 up to 31 Oct 07 to illustrate the performance of the Old ES selection by studying the discrimination power of these variables.

In the left panel of Fig. 6.6 we show the distribution of the ToTF variable. If the cut over TOTF would have been the only one applied we would have found 4 neutrino candidates in data up to 31 October 2007. On the other hand, if we had only applied the cut on `nOfflineToT`≥ 3, we would have found 17 candidate events. This is shown in the right panel of Fig. 6.6.

In Fig. 6.7 we show again the distribution of ToTF, but this time applying also the cut on the number of stations having `nOfflineToT`≥ 3. In this case we would still have found 1 candidate event. It must be noticed that we have not applied the `IsT4Nu` condition yet.

Finally, the `IsT4Nu` requirement removes the only candidate event left after all other cuts are applied. This is a boolean variable (true/false). In the left panel of Fig. 6.8 we show its distribution showing that by itself it leaves 10 candidate events. In the right panel of Fig. 6.8 we show the distribution of the ToTF applying first `nOfflineToT` and `IsT4Nu`.

In Table 6.1 we show the decrease of the selection efficiency of simulated neutrino events.

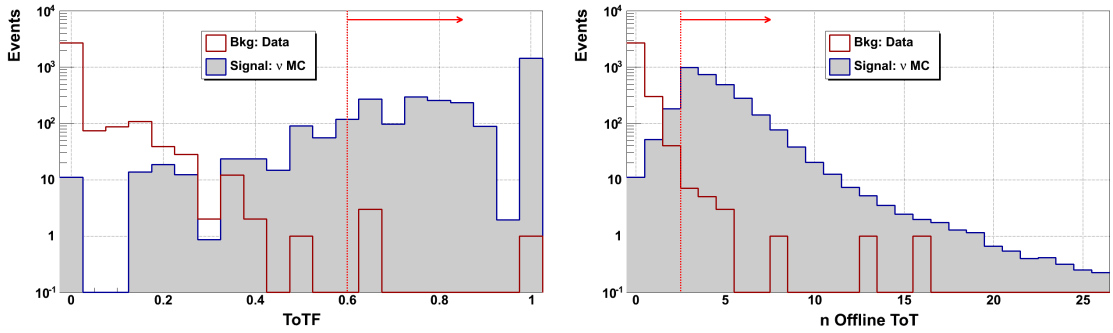

Figure 6.6 Distributions after the quality and inclined selection. The vertical line and arrow indicate the accepted regions. **Left panel:** Distribution of ToTF. **Right panel:** Distribution of `nOfflineToT`.

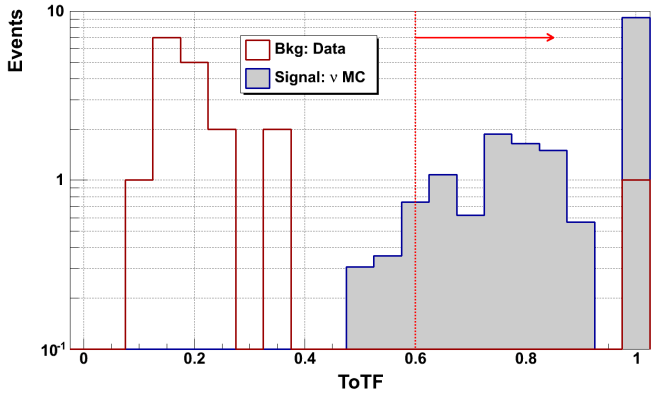

Figure 6.7 Distribution of ToTF when the cut in `nOfflineToT`≥ 3 is applied. One background event is present with TOTF=1.

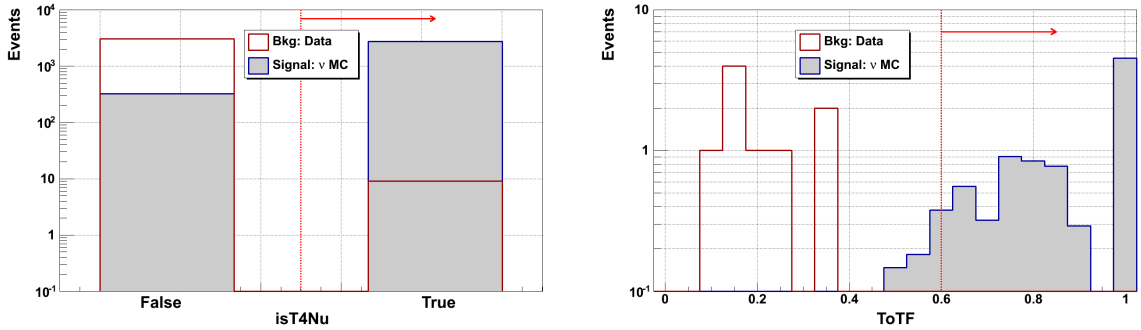

Figure 6.8 **Left panel:** Distribution of the boolean condition `IsT4Nu`. **Right panel:** Distribution of TOTF when when the cuts in `nOfflineToT`≥ 3 and `IsT4Nu` = `True` are applied. No candidates survive ToTF $>$ 0.6.

Selection	Efficiency
Quality and Inclined	95.1%
`nOfflineToT`	87.4%
`IsT4Nu`	85.0%
TOTF	84.1%

Table 6.1 Fraction of remaining yield after each selection cut.

The Old ES selection has advantages and disadvantages that are worth emphasizing here:

1. **Advantages:** The efficiency of selected neutrino Monte Carlo neutrino events is high ($\sim 84.1\%$).

2. **Disadvantages:** No background estimation is possible using the young selection variables. In particular, the requirement of 3 stations having ToT with AoP>1.4 kills almost all events in the data sample so that no events are left to extrapolate the behavior of the data sample distributions. Moreover, due to the boolean nature of `IsT4Nu`, an extrapolation is complicated and unreliable.

We thus developed a new ES selection with efficiency similar to the Old ES, but which allows an estimation of the background.

6.4 New Selection Strategy

As we have seen in Section 6.2 the variable area over peak AoP is a good discriminant between showers induced by a τ decay and the hadronic background. In Figure 6.9 we show how the AoP for 6-stations events changes as a function of the station number ordered in time. It can be seen that for Earth-skimming neutrinos the AoP is higher than for data in all stations. In the case of down-going neutrinos, the AoP is also higher in general but there is a signicant difference between the early and late part of the event. The reason for this was discussed and illustrated in Figure 6.2.

In the bottom left panel of Figure 6.5 we have shown the distribution of the AoP for the earliest station of every event. However we can exploit the fact that events have multiple stations and average over them. It is worth noticing that we have performed multiple tests using Fisher multivariate analysis combining different

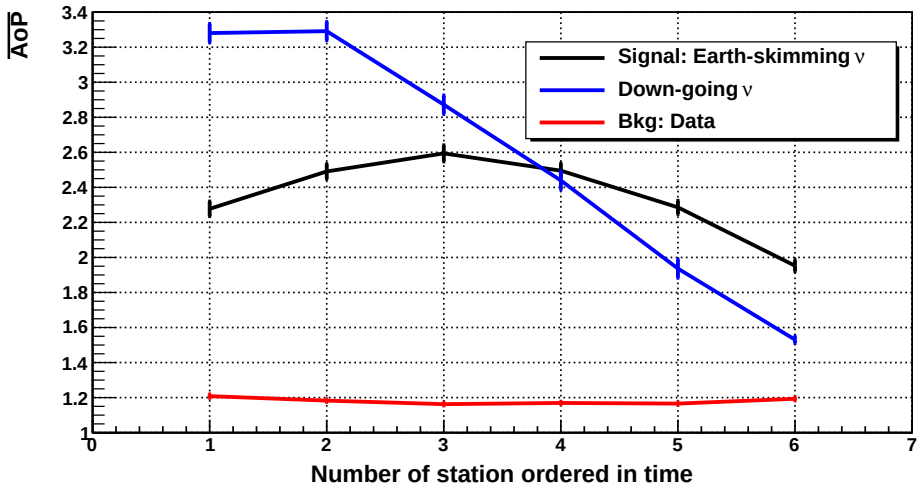

Figure 6.9 AoP as a function of the station number ordered in time.

variables. None of them results in a significant improvement over the average AoP which is chosen for its simplicity.

When averaging we can decide to exclude certain stations. There are two clear reasons to do this.

1. The dynode of one of the PMTs is saturated: in this case the signal from the dynode is used. However, it could happen that also the dynode is saturated. A saturated signal will artificially increase the AoP so we reject these stations.

2. The station has a Threshold 1 trigger (see Section 3.1.2): these stations have a small signal and are more prone to introduce noise to the average.

Another very important reason to exclude a station is when there are multiple peaks close in time in the trace. In Section 5.1.2.3 we have seen that if there are stations with two peaks the one with less signal is removed or the whole station is rejected if the signal of the peaks is similar before performing the inclined reconstruction. However, there are cases when two peaks can be close enough so they don't affect the reconstruction but they increase the AoP of that station. The presence of multiple peaks in a trace inducing a large value of AoP is specially dangerous in low multiplicity events, where even a single station with large AoP can significantly increase the average value $\langle \text{AoP} \rangle$.

As an example, we show in Figure 6.10 an event which has 4 T2 trigger stations. Station 882 has a double peak which results in an AoP=1.91 which is clearly the result of two muons being close in time.

A stricter algorithm developed to idetify traces with multiple peaks close in time is explained next.

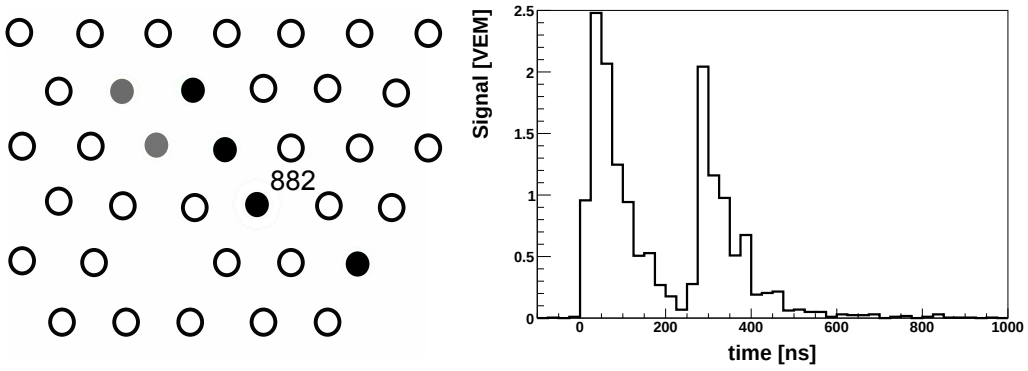

Figure 6.10 Event 2629688. **Left:** Footprint of the event. It is a 4-station event (black circles). The grey circles are stations with T1 trigger. **Right:** The calibrated averaged signal over the 3 PMTs for station 844, showing a typical 2-peak structure.

Close-by Multiple Peak Tagger

1. **Find peaks above 0.6 VEM$_{peak}$:** For each active PMT in the stations of the event, we split the trace in windows of 8 bins. Within each window we find the bin with the maximum signal and define it as a peak if the signal is above 0.6 VEM$_{\text{peak}}$.
2. **Find "blocks" of signal:** If there are more than 1 peak we scan the bins that are located between the peaks found in step 1. We count the number of consecutive bins having signal below 0.3 of the minimum peak found. If there are 6 bins or more we look for the bin between the two peaks being considered that has the minimum signal, and we split the trace at this bin. On the contrary, if there are less than 6 bins, the trace is not split. In Figure 6.11 we show the two peaks found for PMT 1 in station 822 of event 3310521. In this case there are more than 6 bins under the 30% threshold.
3. **Calculate AoP of blocks:** If there are more than 1 block of signal after step 2, we calculate the area (charge) of each block by integrating the first 8 bins or until the signal drops below 0.2 VEM$_{\text{peak}}$. To calculate the AoP we divide the area by the peak value of the block of signal.
4. **Select traces dominated by peaks:** If the sum of the block charges is lower than 90% of the total charge of the trace we consider that the trace is not entirely dominated by individual blocks and we do not flag the PMT.
5. **Count Blocks with AoP<1.5 :** Regardless of the number of particles, muon fronts have AoP $\approx$ 1. If there are several blocks with AoP<1.5 we flag the PMT.
6. **Flag station:** If a station has 2 flagged PMTs, then we flag the station and reject it.

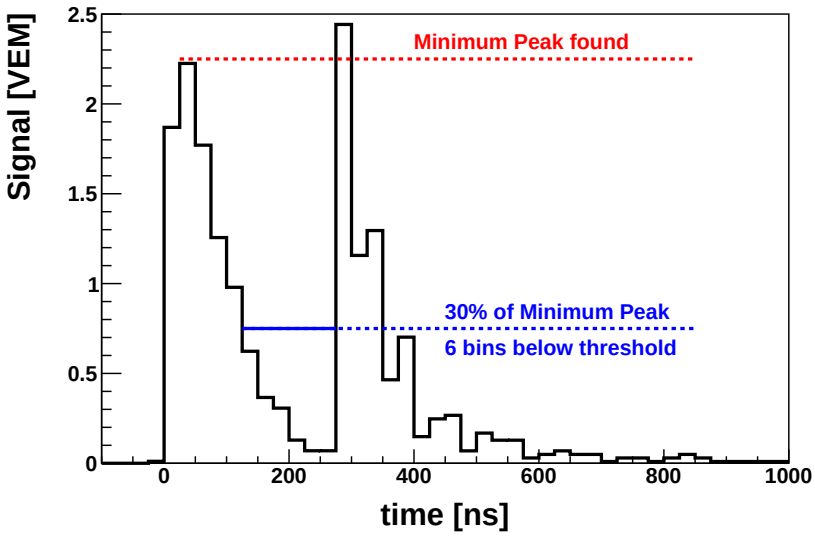

Figure 6.11 Calibrated signal of the event 2629688, station 882 and PMT 1. Two clear peaks are present with 6 contiguous bins below threshold in between.

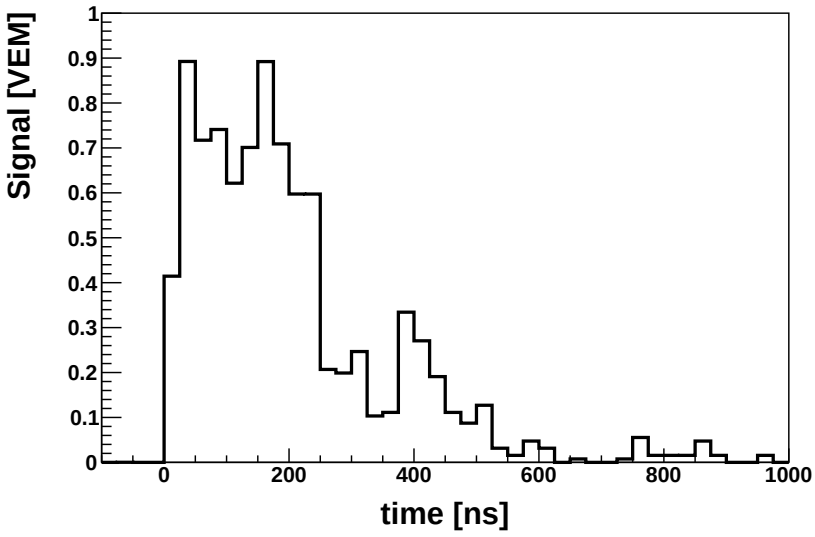

Figure 6.12 Calibrated PMT trace in a station of a simulated emerging tau lepton-induced shower of energy $10^{16.75}$ eV produced in a tau neutrino ES interaction.

It is important to notice that the large values of AoP in simulated neutrino events do not arise from two peaks. A typical trace looks like the one shown in Fig. 6.12 with an AoP=3.29. Comparing this trace with the one shown in Figure 6.11 we can see that the trace is not dominated by two or more separated peaks but, instead, the signal is extended with no gaps in between. Thus, the impact of this tagger on the MC simulated neutrino events is small. In Table 6.2 we show the fraction of stations

tagged by the `Close Multiple Peak Tagger` as a function of E_τ, the energy of the emerging tau lepton induced in tau neutrino ES interactions. It can be seen that the fraction of stations rejected by the tagger is rather small, as expected, particulary for low energy showers. At trigger level the fraction of simulated events rejected after application of the `Multiple Peak Tagger` is only $\sim$0.7%, or 1.2% when the events are weighted according to their energy, zenith and decay height distributions.

$\log_{10} E[eV]$	Fraction of rejected stations
16.5	0.4%
16.75	0.8%
17.0	0.9%
17.25	1.2%
17.5	1.3%
17.75	1.3%
18.0	1.8%
18.5	2.6%
19	3.2%

Table 6.2 Fraction of stations tagged as having multiple peaks in events at trigger level, as a function of the energy of the emerging tau lepton.

Once we remove saturated, T1, and clear multiple peak stations we proceed to calculate the average AoP over all the remaining stations in the event $\langle$AoP$\rangle$. In Figure 6.13 one can see that this variable is a very good discriminator between the data and the simulations of showers induced by the decay of a τ. It is also important to emphasize that the data do not present long tails extended towards the region where the ν simulations are concentrated.

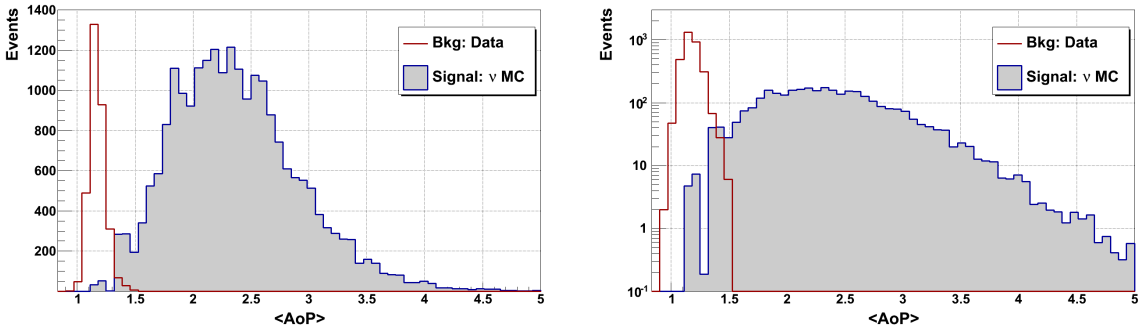

Figure 6.13 Distribution of $\langle$AoP$\rangle$ for training data and MC simulations. *Left:* Linear scale in the y-axis. The MC simulations are normalized to 7 times the data so that both distributions are easily compared. *Right:* Logarithmic scale in the y-axis. The MC simulations are normalized to the data.

6.5 Neutrino event selection and background estimation

Once we have built the discriminant variable we proceed to consider the value of the cut which will classify a shower as a neutrino event. The neutrino signal that we intend to measure is expected to be very small so the sensitivity of the analysis is basically limited by the magnitude of the expected background. In this context it is fundamental to control the contamination of hadronic events which can be missclassified as neutrinos.

In this work we set the value of the cut in $\langle \text{AoP} \rangle$ in such a way that the expected background is less than one event in 50 years. As the exposure of the training period is equivalent to only 1.4 years of the full array, it was necessary to design a strategy that would allow the extrapolation of the number of expected events to a period of 50 years. In particular, we are concerned with the tail of the distribution towards the high values of $\langle \text{AoP} \rangle$. The strategy consists in modelling the tail of the background distribution and normalizing it to the value expected after 50 years (see Fig. 6.14).

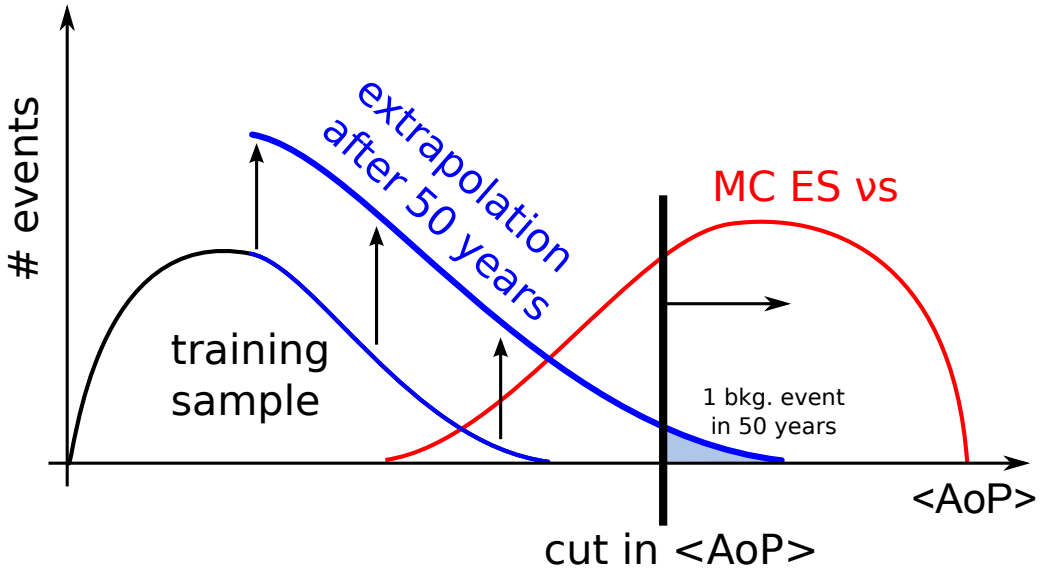

Figure 6.14 Sketch of the strategy designed to fix the value of the cut on the discriminating variable $\langle \text{AoP} \rangle$ (see text for explanation).

In order to adopt a model we can start by considering that the average AoP is the sum of several variables. According to the Central Limit Theorem (CLT), the sum of random variables will tend to a gaussian distribution. However, in our case

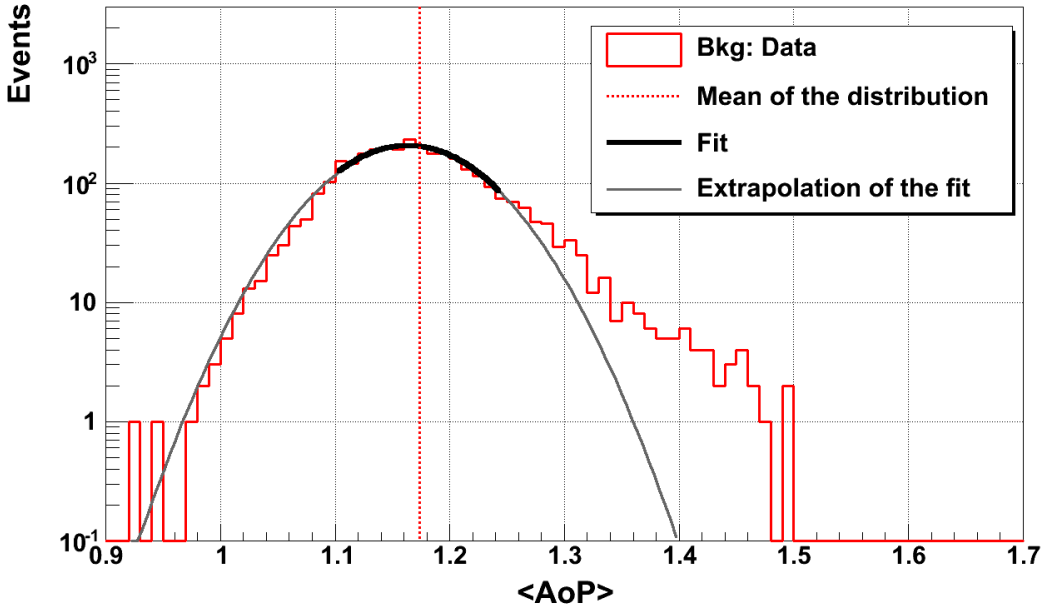

Figure 6.15 Distribution of the average Area over Peak in the Training data for events with 4 stations or more. The mean $\overline{\langle \text{AoP} \rangle}$ of the distribution is indicated with a vertical line. A gaussian fit between $[\overline{\langle \text{AoP} \rangle} - \text{RMS}, \overline{\langle \text{AoP} \rangle} + \text{RMS}]$ is performed and shown in thick black. In grey we show the extrapolation of the fit. Towards the right the distribution falls slower than predicted by the gaussian fit.

the sum is done over a small number of stations and this number is not enough to obtain a gaussian distribution. As can be seen in Figure 6.15 the tail of the distribution falls slower than predicted by a gaussian fit. It is interesting to note that the gaussian prediction works well (poorly) for fluctuations towards low (high) values of $\langle \text{AoP} \rangle$. This is somewhat expected, as the tail towards high $\langle \text{AoP} \rangle$ can be driven by fluctuations in only one station, where the CLT does not apply, while the tail towards low $\langle \text{AoP} \rangle$ arises from the combined effect of all stations.

For the reasons above we adopted an exponential model which falls slower than the gaussian, and describes well the data.

$$N(\langle \text{AoP} \rangle) = e^{A - B\langle \text{AoP} \rangle} \tag{6.1}$$

where $N(\langle \text{AoP} \rangle)$ is the number of events in a bin of width $\Delta\langle \text{AoP} \rangle$. Using logarithmic scale for the y-axis this model is a line where B is the slope.

Using this functional form we fit over the tail of the distribution in the $[1\sigma, 3\sigma]$ region [1]. The result is shown in Figure 6.16.

We test the fit quality in two ways. First, we calculate the statistics χ^2 divided

[1] This notation denominates the region in the interval $[\overline{\langle \text{AoP} \rangle} + 1\text{RMS}, \overline{\langle \text{AoP} \rangle} + 3\text{RMS}]$.

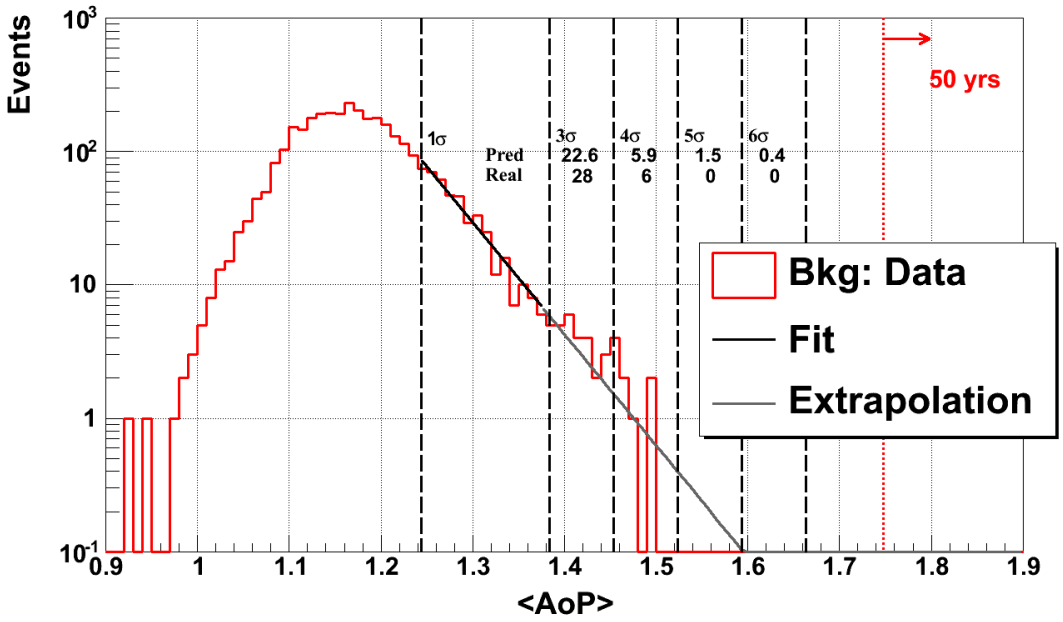

Figure 6.16 Distribution of $\langle \mathrm{AoP} \rangle$ in the training sample for events with 4 stations or more. An exponential fit is peformed in the tail of the distribution, i.e. between $[1\sigma, 3\sigma]$ (see text), which is shown in black. The extrapolation of the fit is shown in grey. The regions $[3\sigma, 4\sigma]$, $[4\sigma, 5\sigma]$, $[5\sigma, 6\sigma]$ and $[6\sigma, 7\sigma]$ are thus not part of the fit. The expected number of events according to the fit (Pred.) and actually measured (Real) is shown for each region. The dotted vertical line shows the value of the cut which is fixed such that the number of expected events is less than one in 50 years.

by the degrees of freedom, ie the number of bins involved in the fit (n=14) minus the two fit parameters.

Secondly, the regions $[3\sigma, 4\sigma]$, $[4\sigma, 5\sigma]$, $[5\sigma, 6\sigma]$ and $[6\sigma, 7\sigma]$ are used to test the extrapolation of the exponential model by comparing the measured number of events with the number of expected events:

$$N = \frac{1}{\Delta\langle \mathrm{AoP} \rangle} \int_{\mu+X\sigma}^{\mu+(X+1)\sigma} d\langle \mathrm{AoP} \rangle \; e^{A-B\langle \mathrm{AoP} \rangle} \tag{6.2}$$

where X is a number between 3 and 6 according to the region, It can observed that the actual number of events from the training sample in each of the four regions is in agreement with the prediction of the exponential model.

As we mentioned, the cut (L_{50}) is set normalizing the distribution to 50 years. The data in the Training sample corresponds to 1.38 years of a complete SD working continuously, so the 50 year distribution would become:

$$N^{50\mathrm{yr}}(\langle \mathrm{AoP} \rangle) = \frac{50}{1.38} e^{A-B\langle \mathrm{AoP} \rangle} \tag{6.3}$$

The cut L_{50} is obtained by requiring one event above L_{50} for $N^{50\text{yr}}$:

$$\frac{1}{\Delta\langle\text{AoP}\rangle}\int_{L_{50}}^{\infty} d\langle\text{AoP}\rangle\ N^{50\text{yr}}(\langle\text{AoP}\rangle) = 1 \rightarrow L_{50} = \frac{\ln\left(1.38 \times B\Delta\langle\text{AoP}\rangle/50\right) - A}{B} \tag{6.4}$$

The statistical uncertainty of L_{50} is obtained using the covariance matrix of parameters A and B. In Table 6.3 we show some important parameters characterizing the distribution (total number of events, mean and RMS), the fit results and its corresponding χ^2, the L_{50} and the efficiency (Eff: fraction of τ simulations with $\langle AoP\rangle$ above the cut L_{50}).

N	3207
$\overline{\langle\text{AoP}\rangle}$	1.1736±0.0012
RMS	0.0700±0.0009
A	28.4 ± 1.9
B	19.2 ± 1.5
$\frac{\chi^2}{N-2}$	$\frac{9.63}{14-2} = 0.80$
L_{50}	1.75±0.04
Eff	75.0%

Table 6.3 Parameters characterizing the distribution of ⟨AoP⟩ and its right tail for the Training sample.

6.5.1 Events with 3 stations

We have seen in Section 5.4 that the number of inclined events with 3 triggered stations in the training data sample is very small (there are only 23 events). However, we mentioned that keeping three station events with configuration 1 is important as it accounts for 19.7% of the efficiency at the inclined selection level (see Table 5.5). In Figure 6.17 we show the distribution of the ⟨AoP⟩ for these events along with those with more than 3 stations.

Events with only 3 triggered stations are more prone to be incorrectly classified as neutrino candidates because an AoP fluctuation in just one station can induce a large value of ⟨AoP⟩. As there are too few events in the data sample we cannot rely only on the AoP distribution for an extrapolation, as done for ≥4 station events. Consequently, for these events we place another selection cut. As we want to be sure that the ⟨AoP⟩ is not driven only by the highest AoP we demand that the lowest AoP of a 3-station event (AoP_{min}) is at least 1.4. The value of the cut is based on the old analysis selection which defined an offline station as one with a ToT trigger

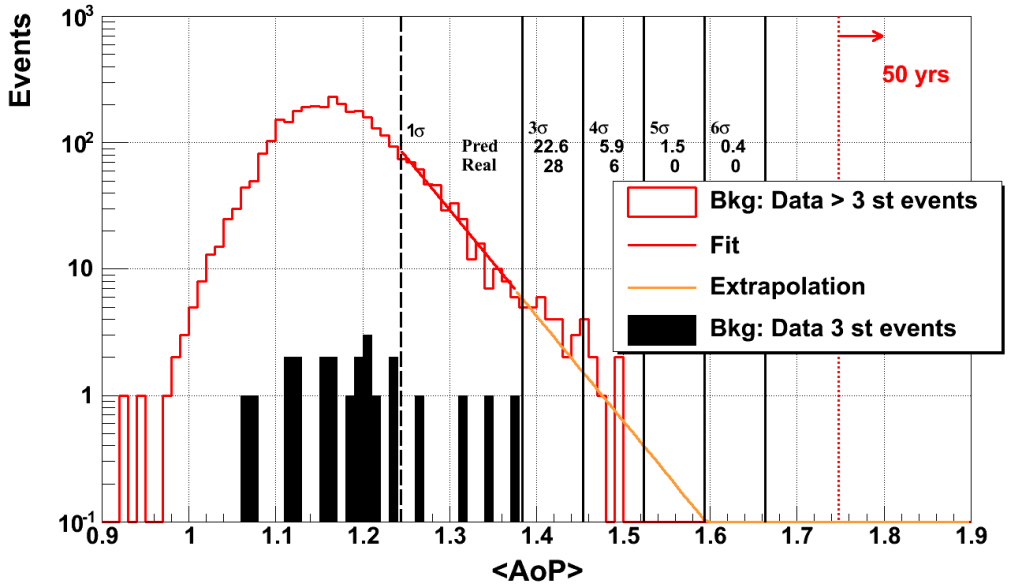

Figure 6.17 Distribution of ⟨AoP⟩ of the data events in the Training sample discriminating events with 3 stations from events with 4 stations or more.

and AoP higher than 1.4. In Fig. 6.18 we show the distribution of AoP_min in 3-station events. This cut reduces the total (3-station) selection efficiency of Monte Carlo simulated events in $\sim 1.3\%$ (8%).

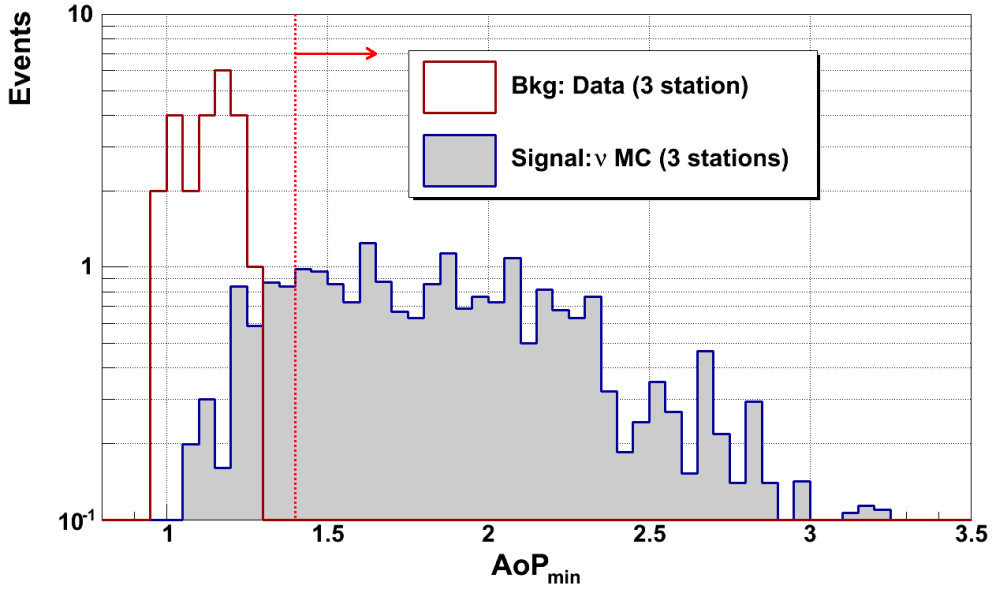

Figure 6.18 Distribution of $\mathrm{AoP_{min}}$ in 3-station events. The cut at $\mathrm{AoP_{min}} > 1.4$ is shown with a vertical dotted line.

In Figure 6.19 we show the final distribution of the average value of AoP in training data and simulations.

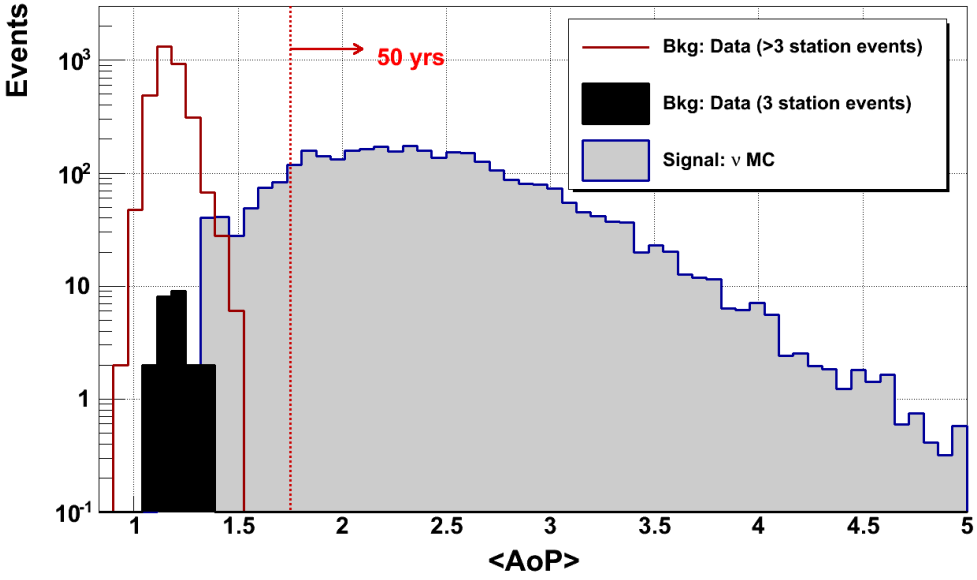

Figure 6.19 Distribution of ⟨AoP⟩ for training data and MC simulations. The vertical dotted line corresponds to the cut in ⟨AoP⟩. Events above this cut are classified as neutrino candidates.

6.6 Training and Test data samples comparison

As mentioned at the beginning of the chapter, the purpose of the "Test sample" is to control the performance of the selection with an independent data sample. One can further tune the selection in case there appear candidates or anomalies in the tail of the distributions of the young shower selection variables that cannot be attributed to neutrino events.

In this section we apply the selection criteria to the "Test sample" and study its compatibility with the training sample.

In Figure 6.20 we show the distributions of ⟨AoP⟩ for the events in both samples. It can be observed that there is a small displacement of the Test sample distribution towards higher ⟨AoP⟩ values. The magnitude of the displacement of the mean value of the ⟨AoP⟩ distribution is small. The relative difference is $\frac{2(\overline{\langle \mathrm{AoP} \rangle}_{\mathrm{test}} - \overline{\langle \mathrm{AoP} \rangle}_{\mathrm{training}})}{(\overline{\langle \mathrm{AoP} \rangle}_{\mathrm{test}} + \overline{\langle \mathrm{AoP} \rangle}_{\mathrm{training}})} =$ 1.1%.

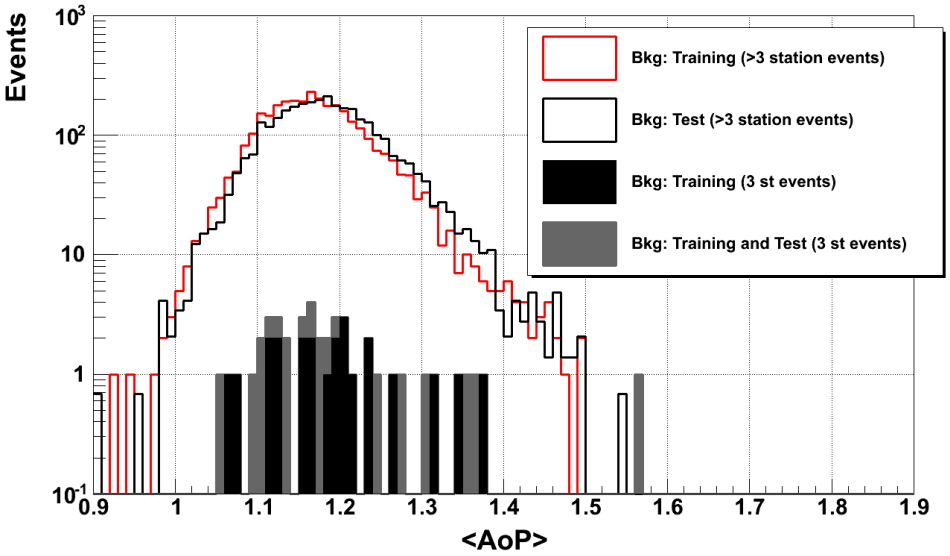

Figure 6.20 Distribution of average Area over Peak in the Training and Test samples. The Test sample for events of 4 or more stations (black) has been normalized to the Training sample (red). In filled black (grey) we show the distribution of data for 3-station events for the training (training plus test) sample.

6.6.1 Time evolution of the mean ⟨AoP⟩ distribution

It is worth studying in more detail the small shift in the mean value of the distribution of ⟨AoP⟩ between the training and test data samples, and in particular if this is an effect of a possible evolution of ⟨AoP⟩ with time. For this purpose in Figure 6.21 we show the evolution with time of the mean value of the distribution of ⟨AoP⟩.

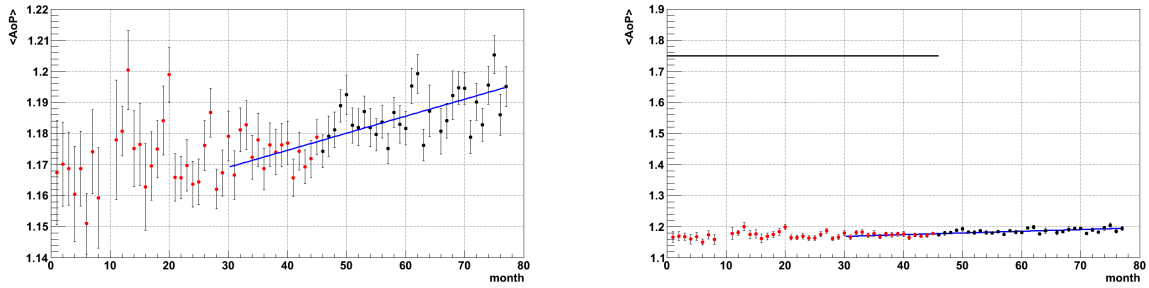

Figure 6.21 Mean value of the distribution of ⟨AoP⟩ per month, from January 2004 (month 0) to May 2010 (month 78). In black (red) dots we show the Training (Test) sample. In solid blue a linear fit to the points between June 2006 and May 2010. *Left:* The scale in the y-axis has been set so that the increase of ⟨AoP⟩ is more apparent. *Right:* The scale in the y-axis has been extended to compare the size of the time dependence with respect to the neutrino selection cut ⟨AoP⟩ ≥1.75.

Performing a fit between June 2006 and May 2010 we find that the $\langle \text{AoP} \rangle$ increases with a slope of $\sim (0.65 \pm 0.15)\frac{\%}{\text{yr}}$. We should however emphasize that the increase is small when compared to the position of the neutrino selection cut, $\langle \text{AoP} \rangle \geq 1.75$ (see Fig. 6.21).

We have tested whether this increase also happens for showers with smaller zenith angles. This was achieved by placing a different cut on the velocity of the signal at ground, namely $0.31\frac{\text{nm}}{\text{s}} < \langle V \rangle < 0.32\frac{\text{nm}}{\text{s}}$ (similar to $70° < \theta < 75°$) instead of the nominal $0.29\frac{\text{nm}}{\text{s}} < \langle V \rangle < 0.31\frac{\text{nm}}{\text{s}}$. The slope of $\langle \text{AoP} \rangle$ is compatible with 0 in this case.

6.6.2 Compatibility of the tails of the distributions in the Training and Test samples

An important test is the compatibility between the tails of the distributions of $\langle \text{AoP} \rangle$ in both samples. In Figure 6.22 we show the distribution of the Test sample along with the corresponding fit to the tail (see Figure 6.17 to compare with the training sample). In Table 6.4 we show the slope of the fit along with the other parameters characterizing the distribution (see Table 6.3 to compare with Training sample).

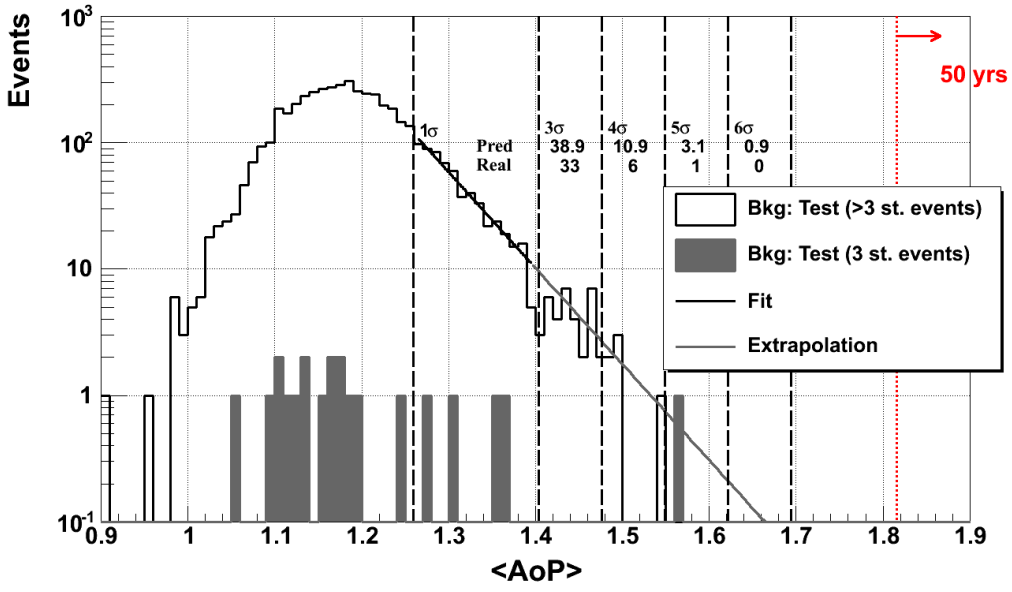

Figure 6.22 Distribution of average Area over Peak for the Test sample.

The distribution of $\langle \text{AoP} \rangle$ in the Test sample differs from the Training sample both in the mean value and in the slope of the linear fit to the tail. The shift in

N	4660
$\overline{\langle \text{AoP} \rangle}$	1.1866±0.0011
RMS	0.0725±0.0008
A	26.8 ± 1.6
B	17.5 ± 1.2
$\frac{\chi^2}{N-2}$	$\frac{9.43}{14-2} = 0.79$
L_{50}	1.82±0.04
Eff	71.3%

Table 6.4 Parameters of the distribution of $\langle \text{AoP} \rangle$ for the Test sample.

mean value of $\langle \text{AoP} \rangle$ is small (+1.1%), but significant (8σ) [2]. The change in slope is larger (9.3%), but compatible within uncertainties (0.9 std).

The value of the cut L_{50} is based on the extrapolation of the linear fit to the tail of the distribution of $\langle \text{AoP} \rangle$. The uncertainty on the A and B propagates to an uncertainty of 0.04 (2%) on L_{50}.

The change in L_{50} due to the shift in mean value is small, it amounts to $\sim$ 0.013 (0.7%). The total change in L_{50} is 0.07 (4%). This means that the dominant effect is not the shift in mean value, but the large uncertainty in the fit.

We have performed an extra check to confirm that the uncertainties on the slopes are reasonable. We have constructed two "clone" samples dividing the total sample (Training + Test) in events with even and odd event numbers. With this construction the two samples are equally influenced by the time evolution of $\langle \text{AoP} \rangle$ shown in Fig. 6.21. Performing a fit to the tails of the cloned distributions, the slopes are 17.8 ± 1.2 and 19.1 ± 1.2 respectively, showing again a rather large difference (7%) but again compatible within uncertainties.

6.6.3 Remarks and Conclusions

1. The distribution of the young shower identification variable $\langle \text{AoP} \rangle$ in the Test sample shows a small displacement of +1.1% with respect to the Training sample.

2. The tails of the Training and Test distributions are compatible within the statistical uncertainties of their corresponding exponential fits. The difference in slopes translates into a difference on the cut on $\langle \text{AoP} \rangle$ of +0.07 (+4%).

[2] The disagreement masured in standard deviations (σ) between two variables $v_1 \pm \sigma_{v_1}$ and $v_2 \pm \sigma_{v_2}$ is calculated as $\frac{v_1 - v_2}{\sqrt{\sigma_{v_1}^2 + \sigma_{v_2}^2}}$, In the case of the $\overline{\langle \text{AoP} \rangle}$ the uncertainty is $\sigma(\overline{\langle \text{AoP} \rangle}) \equiv \frac{RMS(\langle \text{AoP} \rangle)}{\sqrt{N_i}}$.

3. Since the purpose of the Test sample was to allow us to refine the cuts if needed, we use as the final cut on $\langle AoP \rangle$ the one that results from the Test sample, namely $\langle AoP \rangle \geq 1.82$ instead of $\langle AoP \rangle \geq 1.75$. The reasons to do this is that this sample is closer in time to the search sample and the cut is higher (more conservative) that the one derived with the Training sample.

6.7 Summary

In Table 6.5 we display the criteria used to classify an event as a neutrino once it has passed the quality and inclined selections.

	nStation $\geq$ 4	nStation = 3
Young	$\langle AoP \rangle \geq 1.82$	
Showers	-	AoP_min>1.4

Table 6.5 Observables and numerical values of cuts applied to select young showers.

In Table 6.6 we display the efficiency after applying the selection criteria.

	nStation $\geq$ 4	nStation = 3	Total
Quality and Inclined	65.5%	19.7%	85.2%
$\langle AoP \rangle \geq 1.82$	55.4%	15.9%	71.3%
AoP_min>1.4	-	14.6%	70.0%

Table 6.6 Selection efficiency. In the first column we give the selection criteria applied. We divide the samples according to the number of stations.

In Table 6.7 we compare the Training and Test samples when applying the quality and inclined selection. None of the events pass the young selection criteria.

	nStation $\geq$ 4	nStation = 3	Total
Training	3207	23	3230
Test	4660	21	4681

Table 6.7 Number of data events after the quality and inclined selection.

7

Detector efficiency and exposure

In this chapter we study in detail the neutrino identification efficiency using the algorithms presented in the previous two sections. In Section 7.1 we present the detector efficiency and introduce the concept of effective area. In Section 7.2 we discuss the procedure to calculate, given a diffuse flux, the expected number of events at the surface detector. This derivation allow us to define the exposure which is the physical magnitude that summarizes the potential for discovery of the experiment. Finally, we examine and quantify the systematic uncertainties associated with the exposure determination.

7.1 Detector efficiency

In order to develop some intuition about the behaviour and performance of the neutrino identification method, it is useful first to consider the idealized case of an infinite array. In practice, an "infinite array" means an array large enough so that all simulated showers are completely contained. In Sec. 7.1.2, the case of the real detector with finite size is discussed, where it is important to consider the contribution of events that fall in the border and are only partially contained.

7.1.1 Infinite detector efficiency

The MC generated showers initiated by τ decays (Section 4.2.2) were simulated in the central region of a detector composed of 50×50 stations disposed in a perfectly hexagonal array with 1500 m of separation, very similar to the real SD array (although this one is not perfectly regular and its size is smaller).

In this section the neutrino identification efficiency is discussed as a function of the following parameters of the simulated showers:

- Tau energy (E_τ).
- Zenith angle (θ).
- Decay height (X_d).

The efficiency ϵ can be obtained from the MC simulations as:

$$\epsilon(E_\nu, \theta, X_d) = \frac{N_{\rm id}(E_\nu, \theta, X_d)}{N_{\rm sim}(E_\nu, \theta, X_d)} \tag{7.1}$$

where $N_{\rm sim}$ is the number of simulated events for the bin (E_ν, θ, X_d) and $N_{\rm id}$ is the number of identified events. It is important to notice that this definition of $\epsilon(E_\nu, \theta, X_d)$ implies an averaging over the parameters that are not included in the bin specification (azimuthal angle ϕ, τ decay channel, etc.).

In Figure 7.1 it is shown, as an example, the trigger and identificaton efficiency as a function of the decay height X_d for 10^{18} eV τs with zenith angle 90.68°.

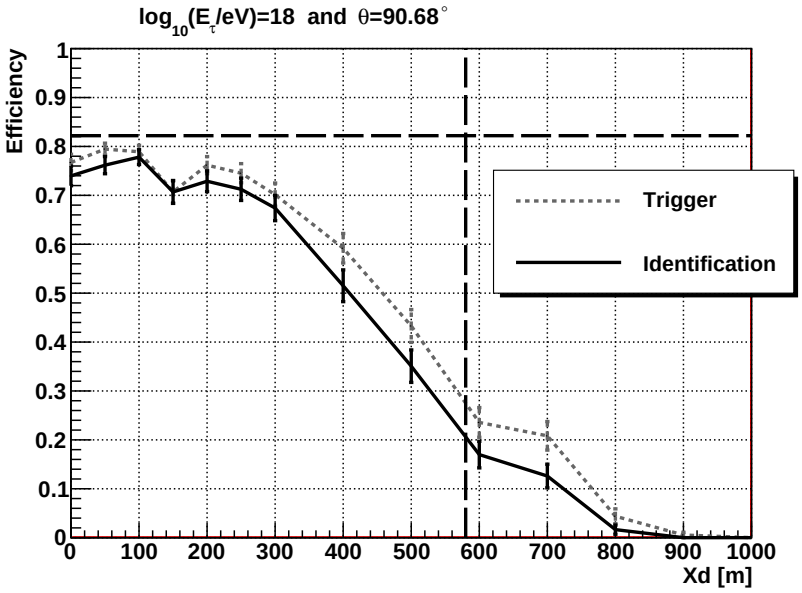

Figure 7.1 Trigger and identification efficiency as a function of the decay height for a τ with energy of 10^{18} eV and $\theta = 90.68°$. The horizontal dashed line corresponds to the trigger efficiency limit imposed by the fact that the τ can decay to $\mu^- + \bar{\nu}_\mu + \nu_\tau$, in which case there is no shower produced (see Section 4.2.1). The vertical dashed line shows the characteristic height at which the τ decays for this kinematic point, $\cos(\pi - \theta)\lambda(E_\tau)$, where $\lambda(E_\tau)$ is the decay length of the τ.

It can be observed that the identification criteria selects most of the triggered events and that below 300 m both the trigger and identification efficiencies are close

to the maximum allowed value which cannot exceed 0.822 as the τ can decay to $\mu^- + \bar{\nu}_\mu + \nu_\tau$, in which case there is no shower produced. At decay heights above 300 m the efficiency falls as the higher the shower starts in the atmosphere, the fewer the particles that reach the ground. However, the characteristic height at which a 10^{18} eV τ coming with zenith angle 90.68° decays is $\lambda_h = \lambda_D \times \cos(\pi - \theta) = 4.9\text{km} \times 0.0119 = 580$ m. This means that 75% of the τs will decay at heights for which the trigger efficiency is higher than zero.

In Figure 7.2 the identification efficiency is shown for three different energies. The efficiency increases because the higher the energy, the more extended the shower footprint, and the larger the number of triggered stations. This increase happens in two ways:

1. At low decay heights, where the efficiency is highest, the efficiency grows until saturating at 0.822.

2. The range of decay heights with efficiency higher than 0 gets larger.

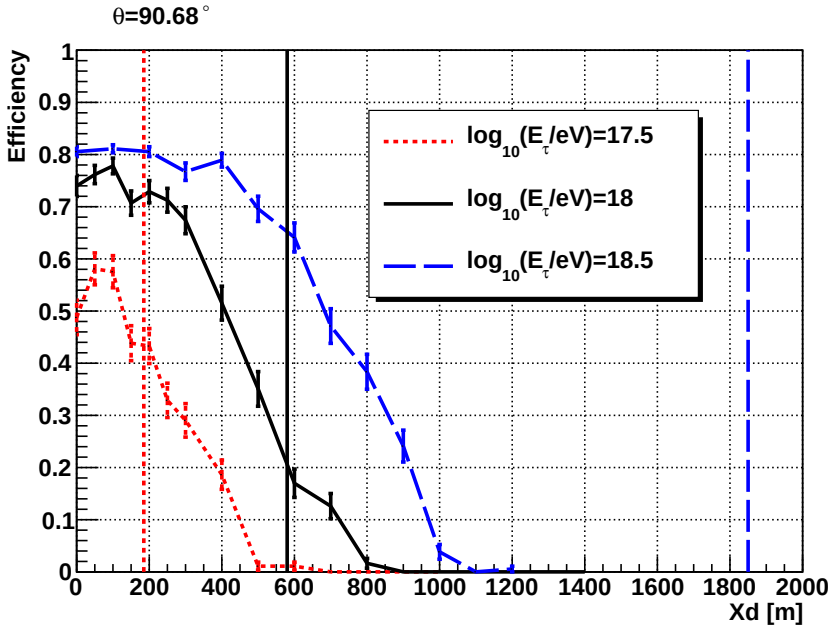

Figure 7.2 Identification efficiency as a function of the decay height for a τ with $\theta = 90.68°$ for three different energies. The vertical lines correspond to the characteristic heights at which the τ decays: 185 ($E_\tau = 10^{17.5}$ eV), 580 ($E_\tau = 10^{18.0}$ eV) and 1850 ($E_\tau = 10^{18.5}$ eV)m.

Although, the efficiency as a function of X_d increases with energy, if one considers the characteristic decay height, it is clear that for higher energies the fraction of τs that decay too high in the atmosphere to be detected increases. As an example,

for a $10^{18.5}$ eV τ coming with zenith angle 90.68° the characteristic decay height is 1.85 km so the majority of the τs decay at heights where the efficiency is 0 (see Figure 7.2):

$$\int_{1000\ \mathrm{m}}^{\infty} \frac{\exp\left(-X_d/1850\ \mathrm{m}\right) dX_d}{1850\ \mathrm{m}} = 0.58 \tag{7.2}$$

It is also interesting to study the dependance with the zenith angle. As it can be seen in the left panel of Figure 7.3 the efficiency falls as the τ comes out of the Earth more vertically. This is evident as the particles in the shower front will also be on average more vertical and fewer of them will reach the ground. Moreover, at higher zenith angles the characteristic decay height increases $\lambda_h = \lambda_D \times \cos\left(\pi - \theta\right)$ so the number of τs decaying in the range where there is identification efficiency is also reduced. For example, for the three zenith angles shown in Figure 7.3 the fraction of τs decaying where the efficiency is 0 are 0.21 (90.68°), 0.68 (91.83°) and 0.85 (92.98°).

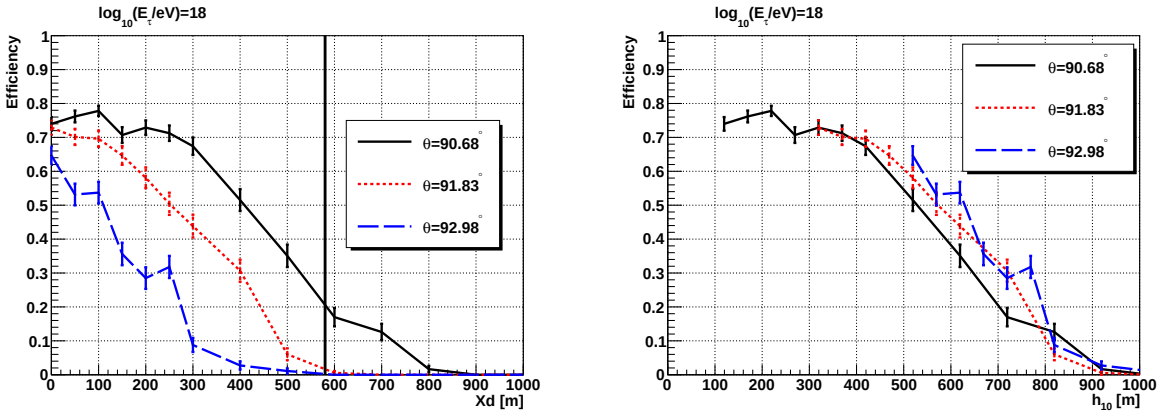

Figure 7.3 *Left:* Identification efficiency as a function of the decay height for a τ with energy of 10^{18} eV for three different zenith angles. The vertical black line at 580 m corresponds to the characteristic height for $\theta = 90.68°$. For $\theta = 91.83°$ and $\theta = 92.98°$ the characteristic heights are 1560 and 2540 m, beyond the scale. *Right:* The same shower efficiencies, but as a function of h_{10}.

It is instructive to introduce the variable $h_{10} \equiv X_d + 10\ \mathrm{km} \times \cos\left(\pi - \theta\right)$, which corresponds to the altitude reached after the shower has travelled 10 km. In the right panel of Figure 7.3 the efficiency is shown as a function of h_{10}. It can be seen that the efficiencies are similar for the different zenith angles, i.e. to first order the efficiency does not vary independently with θ and X_d, but depends only on their combination h_{10}. This is because the probability to detect a quasi-horizontal shower with a given energy depends essentially on the altitude at which it has the

largest lateral extension and is thus capable of producing the largest footprint at ground [125]. For the shower energies relevant in this analysis, h_{10} is very close to this altitude. In particular, this figure shows that, independently of the zenith angle, if the shower maximum is reached at heights larger than 1 km, a neutrino of 10^{18} eV will not be identified.

7.1.2 Finite detector efficiency

In the case of a finite detector, the identification efficiency is a function of the point where the τ emerges from the Earth. The emerging point can be far from (in the middle of) the detector and still the shower develops over (far from) it.

Moreover, inclined showers are characterized by having an elongated footprint that can extend over tens of kilometers, and trigger the SD and be identified even if only part of the footprint is contained in the instrumented area (see Fig. 7.4).

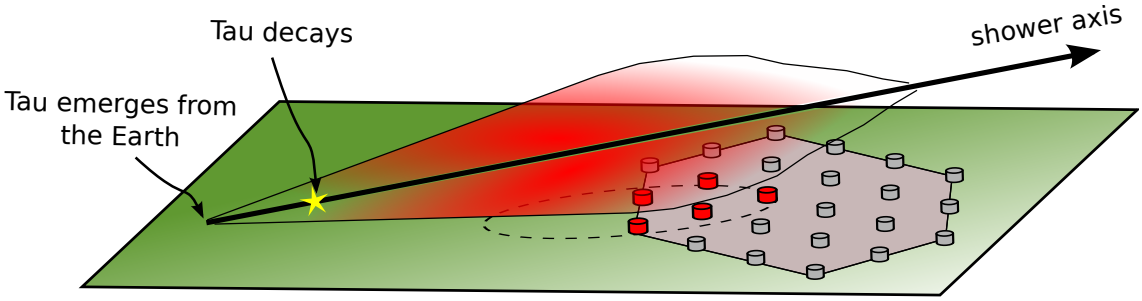

Figure 7.4 In an inclined event the shower particles may partially miss the instrumented area and still produce a T3 trigger on the SD.

Within this context, an extended circular area is defined containing the actual detector and large enough so that it can encompass the showers whose footprint partially miss the detector. In other words, the size of the circle is selected so that the showers falling outside still have chances of triggering the detector (see Figure 7.5).

The relevant magnitude for the analysis is the average identification efficiency over the extended circular area A:

$$\langle \epsilon(\vec{r}, E_\tau, \theta, X_d) \rangle_{\mathrm{A}} = \epsilon(E_\tau, \theta, X_d) = \frac{\int \epsilon(\vec{r}, E_\tau, \theta, X_d)\, \mathrm{d}A}{A} \tag{7.3}$$

This efficiency varies with time as it depends on the number and spatial distribution (configuration) of the working stations at the time of the shower.

It is important to notice that even if $\epsilon(E_\tau, \theta, X_d)$ depends on the choice of the extended area A (it falls when A increases), the product of $\epsilon(E_\tau, \theta, X_d) \times A$ is a

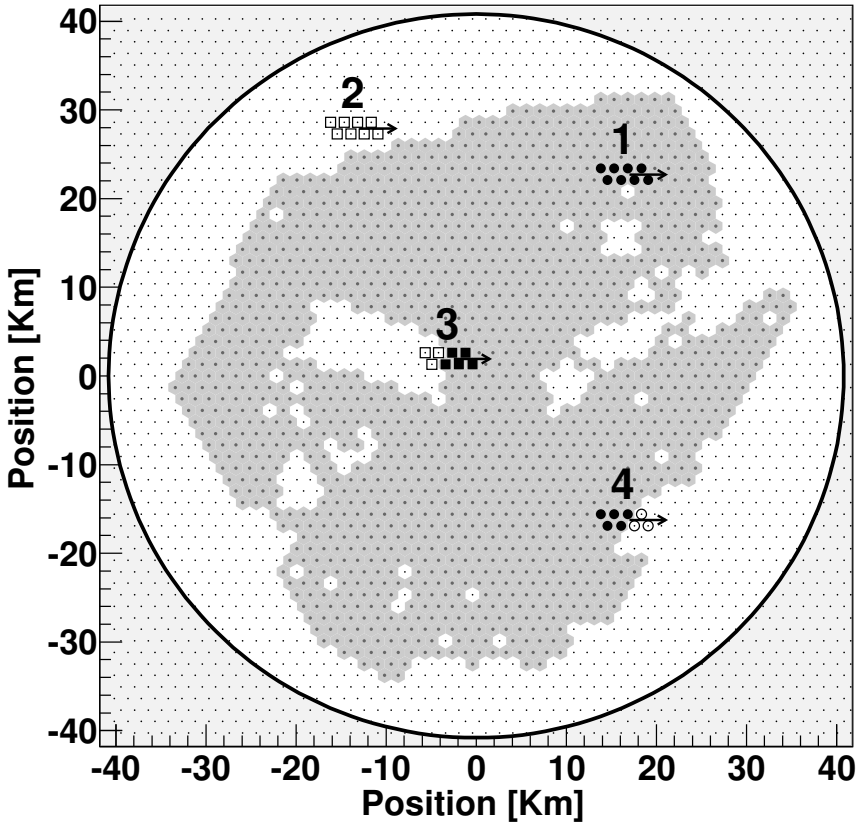

Figure 7.5 Example of a simulated shower, initiated by the decay of a τ, in four different positions over a finite detector (shadowed area) corresponding to 1 November 2007. The arrows indicate the direction of the shower, the points represent the ideal and infinite array of stations and the circunference the extended area (see text). Solid (open) symbols correspond to stations of the simulated shower which have a T2 local trigger and which are (not) active in the reference configuration. Round symbols indicate showers which are identified as neutrinos and square symbols those which are not. In case 1 the shower is fully contained and identified as a neutrino. In case 2 the shower is completely out and, consequently, does not trigger the real detector. In case 3 (4) the shower is partially contained and triggers the SD, however it is (not) identified as a neutrino because, by chance, the stations with higher area over peak fall inside (outside) the real detector.

constant which defines an intrinsic property called effective area $\mathcal{A}_{\text{eff}}$:

$$\mathcal{A}_{\text{eff}}(E_\tau, \theta, X_d) = \int_A \epsilon(\vec{r}, E_\tau, \theta, X_d)\, \mathrm{d}A \tag{7.4}$$

This area represents the equivalent surface of a 100% efficient detector. In princi-

ple, to calculate this magnitude, one should perform the complete set of simulations from the decay to the response of the detector for every configuration. However, this is impractical and it would require a number of simulations impossible to be carried out. For this reason, it was decided to follow a different approach in which the simulations produced in the infinite array are reused to calculate the identification efficiencies in all possible configurations of the real SD. The barycenter of each shower simulated over the ideal array is randomly located over the extended circular area. The stations of the simulated events that do not match an active station of the finite array are discarded (see Fig. 7.5). In this way one has the event that would be obtained if the simulation would have been performed over the actual detector. Using only the selected stations, the trigger conditions are reevaluated and, if satisfied, the global variables are recomputed and the inclined and young selection cuts are applied. In Fig. 7.5 it is summarized, as an example, the results of possible reevaluations of a single event which is identified as a neutrino in the case of an infinite array.

The ratio of identified events over the total events defines the identification efficiency $\epsilon(E_\nu, \theta, X_d, t)$ of the configuration:

$$\epsilon(E_\tau, \theta, X_d, t) = \frac{N_{\text{id}}(E_\tau, \theta, X_d, t)}{N_{\text{sim}}(E_\tau, \theta, X_d)} \tag{7.5}$$

where the dependence on t reminds that the efficiency varies from configuration to configuration.

$\mathcal{A}_{\text{eff}}(E_\tau, \theta, X_d, t)$ is obtained by multiplying by the surface of the extended area A:

$$\mathcal{A}_{\text{eff}}(E_\nu, \theta, X_d, t) = \epsilon(E_\tau, \theta, X_d, t) \times A \tag{7.6}$$

7.2 Exposure

7.2.1 Exposure definition

We define the diffuse exposure $\mathcal{E}$ as the magnitude that when convoluted with the diffuse ν flux results in the number of expected events.

$$N_{\text{exp}} = \int_{E_{\text{min}}}^{E_{\text{max}}} \Phi(E_\nu)\, \mathcal{E}(E_\nu)\, \mathrm{d}E_\nu \tag{7.7}$$

It is, in a way, the magnitude that shows how good an experiment is, as it determines which are the fluxes one could be able to measure and which are not. Inverting the problem, if one observes a number of events n, one has to divide by the exposure in order to derive the incident flux at Earth.

In Section 4.3 it has been discussed that the number of expected events per unit

of time and area is:

$$\frac{\mathrm{d}N_{\mathrm{exp}}}{\mathrm{d}t\mathrm{d}\mathrm{A}} = \int dE_\nu \int dE_\tau \int d\Omega \int dX_d \, \Phi(E_\nu) \, f(E_\tau|\theta, E_\nu) \, h(X_d|E_\tau, \theta) \, |\cos(\theta)| \, \varepsilon(E_\tau, \theta, X_d) \tag{7.8}$$

where $f(E_\tau|\theta, E_\nu)$ and $h(X_d|E_\tau, \theta)$ are the probability density functions defined in Section 4.3.

The number of expected events per unit of time is obtained by considering the effective area $\mathcal{A}_{\mathrm{eff}}(E_\tau, \theta, X_d, t)$, defined in equation 7.6:

$$\frac{\mathrm{d}N_{\mathrm{exp}}}{\mathrm{d}t} = \int dE_\nu \int dE_\tau \int d\Omega \int dX_d \, \Phi(E_\nu) \, f(E_\tau|\theta, E_\nu) \, h(X_d|E_\tau, \theta) \, |\cos(\theta)| \, \mathcal{A}_{\mathrm{eff}}(E_\tau, \theta, X_d, t) \tag{7.9}$$

where we have included the time dependence of $\mathcal{A}_{\mathrm{eff}}$ (equation 7.6).

Consequently, considering equations 7.7 and 7.9 we have that the exposure is:

$$\mathcal{E}(E_\nu) = \int dt \int dE_\tau \int d\Omega \int dX_d \, f(E_\tau|\theta, E_\nu) \, h(X_d|E_\tau, \theta) \, |\cos\theta| \, \mathcal{A}_{\mathrm{eff}}(E_\tau, \theta, X_d, t) \tag{7.10}$$

Integrating in ϕ we obtain:

$$\mathcal{E}(E_\nu) = 2\pi \int dt \int dE_\tau \int d\cos\theta \int dX_d \, f(E_\tau|\theta, E_\nu) \, h(X_d|E_\tau, \theta) \, |\cos\theta| \, \mathcal{A}_{\mathrm{eff}}(E_\tau, \theta, X_d, t) \tag{7.11}$$

7.2.2 Temporal evolution of the SD

Calculating the time integrated exposure of a real detector is not simple. The SD was in construction until the end of 2008. Moreover, the number of active stations changed not only while it was being constructed but also because of temporal failures or maintenance periods. Therefore, it was necessary to develop a method capable of contemplating the temporal evolution.

The state of the detector is monitored every second via the trigger T2 frequency of all stations that indicates which are working correctly. This information is translated into files which register all configurations (set of active stations) of the SD with a time resolution of 1 second. Ideally, the exposure would have to be evaluated over all configurations and integrated over the lapse of time corresponding to each one. As it is not possible to consider individually this huge number of configurations, the period from January 2004 to December 2012 (3287 days) is divided into 1095 sub-periods of 3 days and for each sub-period a reference configuration is selected. The live time assigned to each of these configurations corresponds to the duration the array has a number of stations higher or equal than the reference one.

For each period, it is not obvious which of the many configurations is to be chosen as the representative one. In order to deal with this problem we make

the approximation that within the 3 day period the exposure is only a function of the number of active stations, regardless of their spatial distribution. Although it is clear that this approximation is not true in general (for example, 6 stations in an hexagonal configuration do not clearly have the same exposure as 6 alligned stations), it is nevertheless a very good one when we consider short periods of time in which there are many active stations and the configurations are similar.

Figure 7.6 shows, as an example, the number of active stations as a function of time for a period corresponding to the "Test sample" (from 3 January 2008 to 5 January 2008). The crossed region corresponds to a time lapse which is classified as "bad period" (see Section 5.1) in which the detector was particularly unstable and is removed from the analysis. As it can be seen, the number of active stations is essentially constant over most of the time with the exception of brief periods where the number drops abruptly. During these intervals the configuration can be significantly different [1] and the approximation of an exposure depending only on the number of station is no longer valid. Therefore, these intervals are eliminated and are substracted from the total time the reference configuration is considered active.

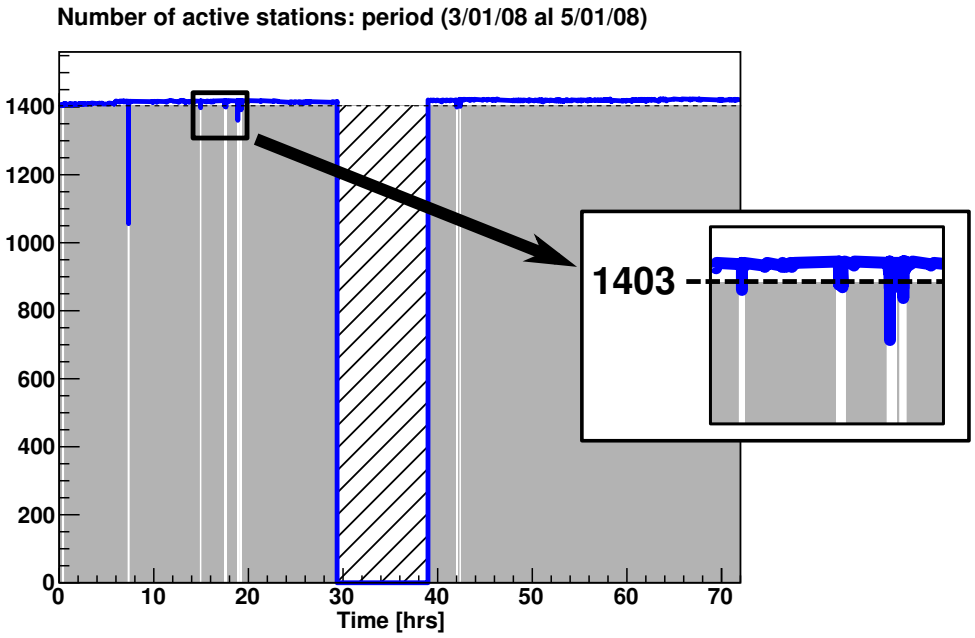

Figure 7.6 Number of active stations as a function of time for the period 488 (from 3 January 2008 to 5 January 2008). The crossed region corresponds to a "bad period" (see Section 5.1). The chosen reference configuration has 1403 active stations. The shadowed region corresponds to the time ranges actually used in this 3-day period.

[1] These are typically due to communication problems and not to local failures at the stations.

The representative configuration is chosen so that the product $N \times T$ is maximum, where N is a given number of active stations and T is the time in which the detector has a number of stations equal or higher than N. In this way, each 3-day period is analysed, and a configuration selected maximizing the mentioned criterion. If there is more than one configuration satisfying the criterion, one keeps the earliest. There is no difference between using this configuration or the next one under the approximation we are working with.

This method allows to obtain a lower limit to the exposure of the detector as the number of active stations is underestimated. The systematic uncertainty of this approach is studied by analysing the differences produced when selecting a reference configuration for different number of days. The result is that the effect is of the order of 1%, much lower that other uncertainties discussed in Sec. 7.2.5.

7.2.3 Exposure calculation

In this section we explain how the calculation of the exposure is done. In the previous section we have explained how to obtain a reference configuration for a 3-day period and in Section 7.1.2 we have explained how to obtain the effective area, $\mathcal{A}_{\rm eff}$. We will use the effective areas corresponding to configuration 488 (from 3 January 2008 to 5 January 2008) to illustrate the procedure.

In order to perform an integration over the parameter space of E_τ, θ and X_d, the first step is to complete the cubic grid defined in Section 4.3. We have mentioned that there are regions in the parameter space that contribute more to the event rate than others so we have sampled them with a smaller step. For energies below 10^{18} eV and $\theta < 94^\circ$ we have simulated showers with a separation of $\Delta X_d = 50$ m while higher energies or higher zenith angles the parameter space is sampled with $\Delta X_d = 100$ m. When the step is $\Delta X_d = 100$ m, the $\Delta X_d = 50$ m point is obtained by a linear interpolation. For example:

$$A_{\rm eff}(50\ {\rm m}) = \frac{A_{\rm eff}(0\ {\rm m}) + A_{\rm eff}(100\ {\rm m})}{2} \quad \text{for } \log_{10}(E_\tau/{\rm eV}) = 18.5 \text{ and } \theta = 90.68^\circ \tag{7.12}$$

Also, for energies below 10^{18} eV we have sampled the parameter space with $\Delta \log_{10}(E_\tau/{\rm eV}) = 0.25$ while for higher energies the separation is $\Delta \log_{10}(E_\tau/{\rm eV}) = 0.5$. When not available, the $\Delta \log_{10}(E_\tau/{\rm eV}) = 0.25$ point is obtained by a linear interpolation in log scale. For example:

$$A_{\rm eff}(10^{18.25}\ {\rm eV}) = \frac{A_{\rm eff}(10^{18}\ {\rm eV}) + A_{\rm eff}(10^{18.5}{\rm eV})}{2} \quad \text{for } \theta = 90.68^\circ \text{ and } X_d = 50\ {\rm m} \tag{7.13}$$

Once that we have a cubic grid the effective area at any point (E_τ, θ, X_d) is obtained by a trilinear interpolation where the 8 vertices around the point are

weighted according to the distance in each of the 3 dimensions. This is:

$$\begin{aligned} A_{\text{eff}}(\hat{E}_\tau, \hat{\theta}, \hat{X}_d) = \frac{1}{0.25 \times 0.01 \text{ rad} \times 50 \text{ m}} \Big[& A_{\text{eff}}(m,m,m)(1-\Delta\log\hat{E}_\tau)(1-\Delta\hat{\theta})(1-\Delta\hat{X}_d) \\ & + A_{\text{eff}}(M,m,m)(\Delta\log\hat{E}_\tau)(1-\Delta\hat{\theta})(1-\Delta\hat{X}_d) \\ & + A_{\text{eff}}(m,M,m)(1-\Delta\log\hat{E}_\tau)(\Delta\hat{\theta})(1-\Delta\hat{X}_d) \\ & + A_{\text{eff}}(m,m,M)(1-\Delta\log\hat{E}_\tau)(1-\Delta\hat{\theta})(\Delta\hat{X}_d) \\ & + A_{\text{eff}}(M,M,m)(\Delta\log\hat{E}_\tau)(\Delta\hat{\theta})(1-\Delta\hat{X}_d) \\ & + A_{\text{eff}}(M,m,M)(\Delta\log\hat{E}_\tau)(1-\Delta\hat{\theta})(\Delta\hat{X}_d) \\ & + A_{\text{eff}}(m,M,M)(1-\Delta\log\hat{E}_\tau)(\Delta\hat{\theta})(\Delta\hat{X}_d) \\ & + A_{\text{eff}}(M,M,M)(\Delta\log\hat{E}_\tau)(\Delta\hat{\theta})(\Delta\hat{X}_d) \Big] \end{aligned} \tag{7.14}$$

where $\Delta\log\hat{E}_\tau$, $\Delta\hat{\theta}$ and $\Delta\hat{X}_d$ are the distances from the interpolation point to the lower $(m,\, m,\, m)$ vertex.

In order to calculate the exposure we also need $f(E_\tau|\theta, E_\nu)\, h(X|E_\tau, \theta)|\cos\theta|$. $h(X|E_\tau,\theta)\cos\theta$ can be obtained analytically, while for $f(E_\tau|\theta, E_\nu)$ we perform a bilinear interpolation similar to the one for A_{eff} in equation 7.14, but in E_τ and θ.

In the left panel of Figure 7.7 we show the effective areas as a function of θ and X_d for four different values of E_τ, which are the ones relevant for the computation of the exposure at $E_\nu = 10^{17.5}$ eV. The effective areas increase with E_τ and decrease with X_d and θ. This is a direct consequence of how the efficiency changes as a function of these three variables, as we have seen in Section 7.1.1.

The right panel of Figure 7.7 shows the effective areas convoluted with the probability density that a $10^{17.5}$ eV neutrino populates these points:

$$f(E_\tau|\theta, 10^{17.5}\text{eV})\, h(X_d|E_\tau,\theta)\, \mathcal{A}_{\text{eff}}(E_\tau,\theta,X_d)\, \cos(\pi-\theta)$$

The most important region when calculating the exposure at $10^{17.5}$ eV is at $E_\tau \sim 10^{17.25}$ eV. This is because $f(E_\tau|\theta, 10^{17.5}$ eV) peaks around this energy. This is shown by comparing the first and second row panels. Even though the effective areas are higher at $10^{17.5}$ eV than at $10^{17.25}$ eV, there are very few $10^{17.5}$ eV neutrinos that produce a τ that emerges from the Earth with an energy close to $10^{17.5}$ eV, but there are many which have an energy around $10^{17.25}$ eV.

The decrease in X_d is enhanced by $h(X_d|E_\tau,\theta)$ and the sharp supression at $\theta = 90°$ is the result of the $\cos(\pi-\theta)$ term in the pdf.

In order to establish the relevant range of zenith angles we integrate the area convoluted with the pdf in E_τ and X_d and we obtain the differential exposure over solid angle and time which depends only on θ:

$$\frac{d\mathcal{E}(E_\nu,\theta)}{d\Omega dt} = \iint dE_\tau dX_d f(E_\tau|\theta,E_\nu)\, h(X_d|E_\tau,\theta)\, |\cos\theta|\, \mathcal{A}_{\text{eff}}(E_\tau,\theta,X_d) \tag{7.15}$$

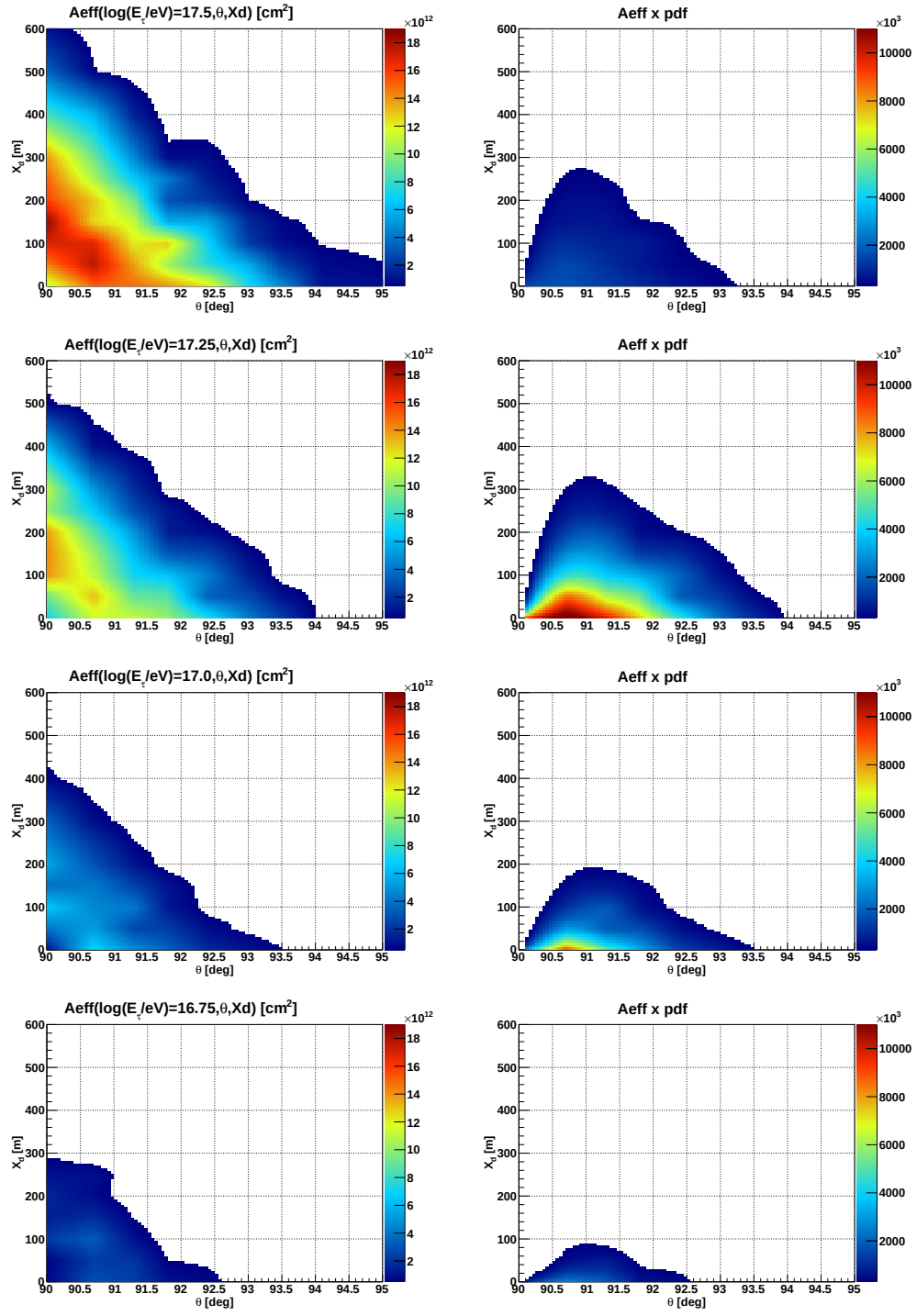

Figure 7.7 *Left:* Effective areas as a function of θ and X_d for the four values of E_τ relevant for the calculation of the exposure at $E_\nu = 10^{17.5}$ eV. *Right:* Effective areas convoluted with the probability density that the point is populated by a $10^{17.5}$ eV neutrino.

In Figure 7.8 we show this magnitude as a function of the zenith angle for several neutrino energies. For $E_\nu = 10^{17.5}$ eV the relevant range of zenith angles is between 90° and 93°. In the right panel of Figure 7.8 it can be seen that as the energy of the neutrino increases the relevant angular range decreases. This behaviour can be understood from the plots in Figure 7.9, which show with shaded area the probability that a neutrino will give rise to an emerging tau lepton, for two neutrino energies ($10^{17.5}$ and $10^{19.5}$ eV) and zenith angles (90.5° and 91.5°). It can be observed that, due to the higher interaction cross-section, this probability decreases faster with θ the higher the neutrino energy.

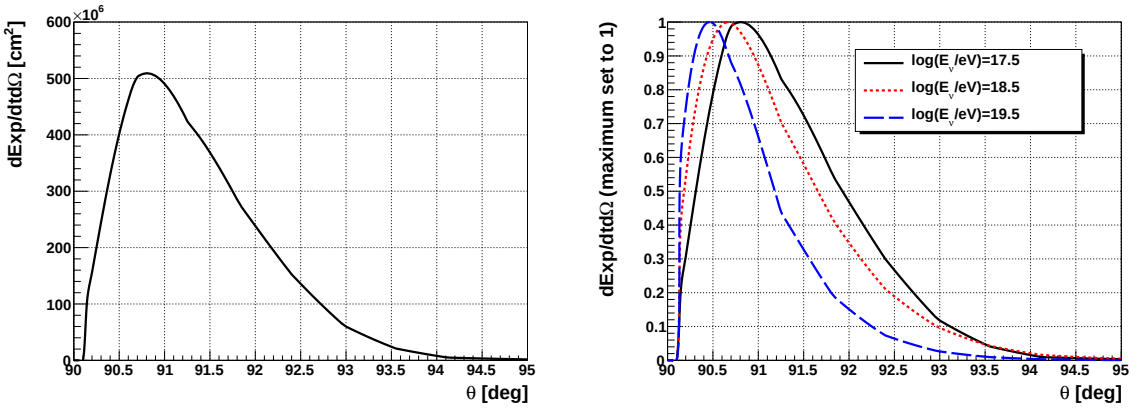

Figure 7.8 *Left:* Differential exposure as a function of the neutrino zenith angle for $E_\nu = 10^{17}$ eV. *Right:* The same for three different values of E_ν, normalized so that their maxima are set to 1.

Now if we integrate the left panel of Figure 7.8 in solid angle we obtain 8.4×10^7 cm^2 sr. The integration in time is only a factor which considers the period in which the configuration is considered to be active as explained in Section 7.2.2. For this case, the total amount of time is 224443 s, which are the 3 days minus the $\sim$ 9 hours of deadtime that are shown in Figure 7.6. Finally, the exposure at $10^{17.5}$eV is $\mathcal{E}(10^{17.5}\text{eV}) = 1.9 \times 10^{13}$ s cm^2 sr. We proceed in the same way for all neutrino energies and array configurations.

Each simulated shower is laid down only once within the circular area. To assess the statistical uncertainty associated with this procedure, for one particular 3-day period we reuse each shower 20 times, obtaining thus 20 different values for the effective area A_{eff} and for the exposure, eq. 7.10. We calculate the average and RMS of the resulting exposures and estimate the relative uncertainty by plotting the ratio $RMS(\mathcal{E})/\langle\mathcal{E}\rangle$ as a function of neutrino energy, see Fig 7.10.

The uncertainty decreases as a function of energy because the fraction of selected showers increases with energy. In general, this uncertainty is negligible when comparing it to the systematic theoretical uncertainties resulting from the tau energy

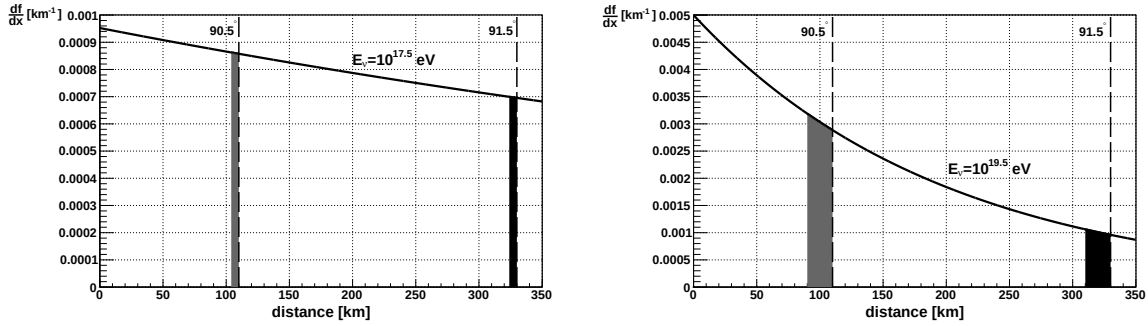

Figure 7.9 Interaction probability density of a neutrino traversing the Earth. The length of matter that needs to be crossed at 90.5° and 91.5° is 110 and 330 km, denoted with vertical dashed lines. The range where a neutrino must interact to give rise to an emerging τ is shown with black (90.5°) and grey (91.5°) areas. *Left:* $10^{17.5}$ eV neutrino with $\sigma_{CC} = 6 \times 10^{-32}$ cm^2, $\lambda_{int} = 1000$ km. The range for a τ with energy $0.8 \times 10^{17.5}$ eV is 6 km. *Right:* $10^{19.5}$ eV neutrino with $\sigma_{CC} = 3 \times 10^{-31}$ cm^2, $\lambda_{int} = 200$ km. The range for a τ with energy $0.8 \times 10^{19.5}$ eV is 20 km.

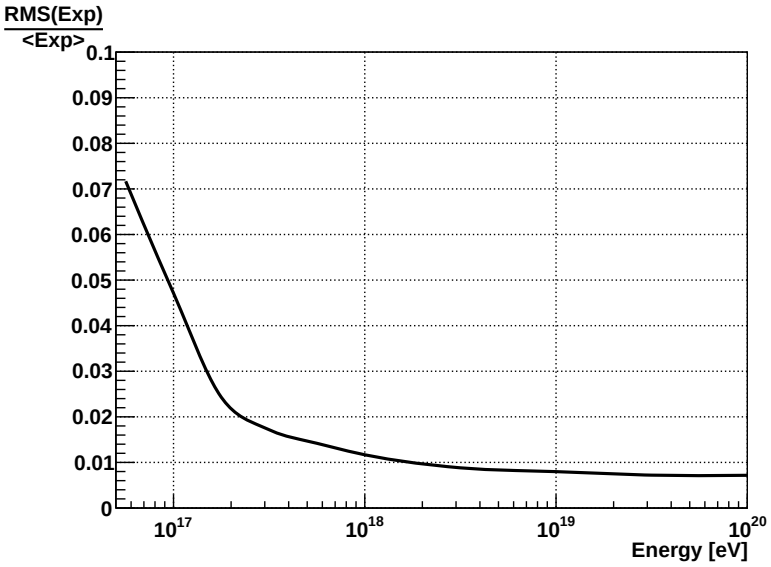

Figure 7.10 Relative statistical uncertainty in the exposure as a function of the neutrino energy.

losses (see Section 7.2.5.1). Moreover, this uncertainty is further reduced as the total exposure is the sum over $N \sim 1000$ configuration and, consequently, it is divided by a factor $\sqrt{N} \approx 30$, assuming all configurations have similar effective areas.

7.2.4 Exposure results

In the previous section we explained the procedure to calculate the exposure. In this section we present the results obtained.

In Chapter 6 we explained that there are two different selections applied to the data. The first one is applied until May 2010[2], while the second one is applied from June 2010 to December 2012. In Figure 7.11 we show the exposure for equal periods of time for the case of the new and old criteria together with their ratio.

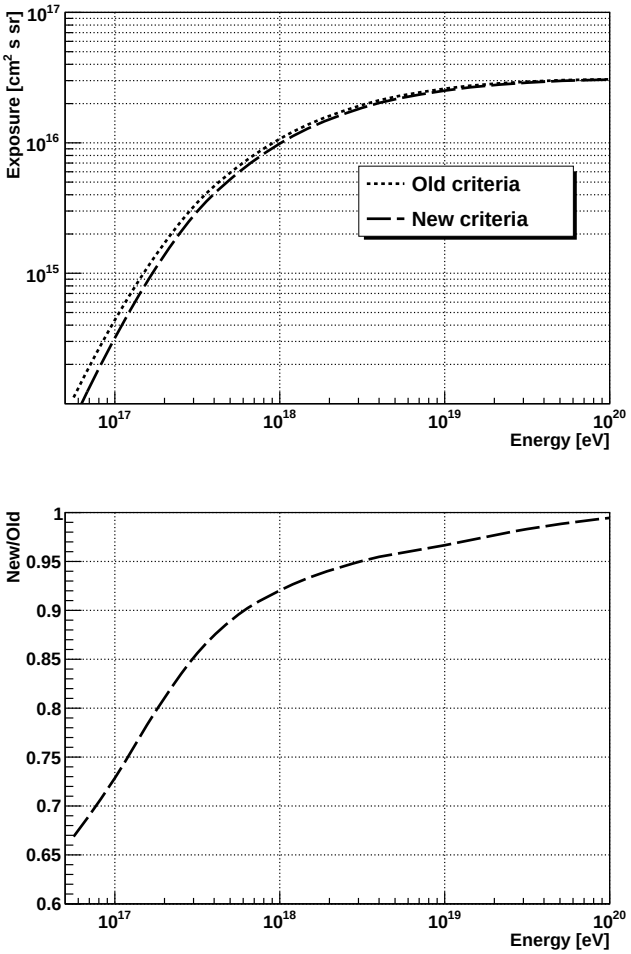

Figure 7.11 *Top:* Exposure of the SD corresponding to 1 year of a complete array when applying the old and new criteria. *Bottom:* Ratio between the new and old criteria.

As expected the new criteria are less efficient than the old ones, a price to pay for the stricter control of the background. The most important reason is that in the new analysis 3-station events are only selected if they belong to configuration 1 (see Section 5.3.2). This is why the difference is largest towards lower neutrino

[2]Excluding November and December 2004.

energies. The number of expected events is proportional to the integral of the exposure convoluted with the flux. If we assume a E^{-2} dependence and we integrate between $10^{16.75}$ and 10^{20} eV:

$$\mathcal{N} \propto \int \mathrm{d}E_\nu \, \mathcal{E}(E_\nu) E_\nu^{-2} \tag{7.16}$$

we obtain $\frac{\mathcal{N}_{new}}{\mathcal{N}_{old}} = 0.89$.

The complete exposure is shown in Figure 7.12 where we use the new and old criteria for the corresponding periods which are equivalent to 3.4 and 2.3 years of a full SD array respectively.

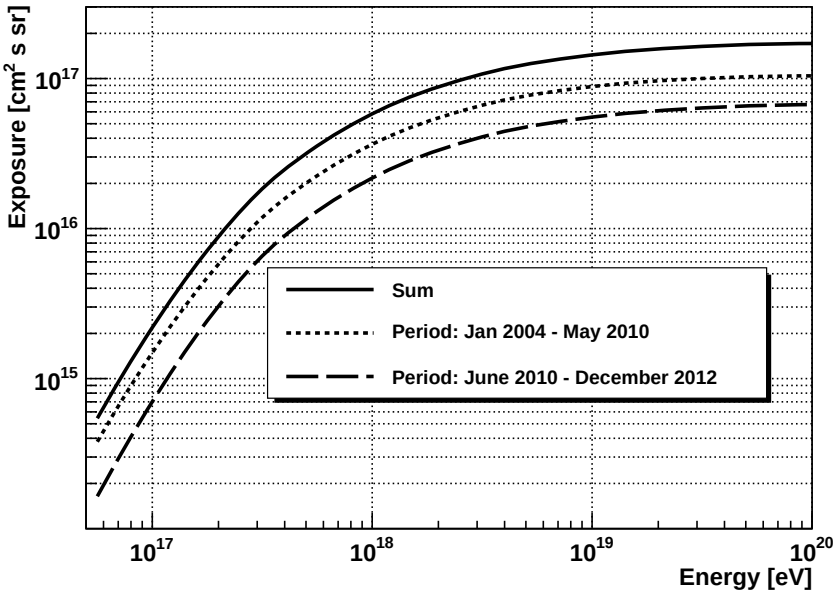

Figure 7.12 Exposure of the SD corresponding to the Search period, 1 June 2010 to 31 December 2012 (dashed) and Training and Test periods, 1 January 2004 - 31 May 2010 (dotted). These correspond to 3.4 and 2.3 years of a full SD array. The total exposure is shown in solid line.

It is useful to define the range of energies where we expect 90% of the events to be observed. In Figure 7.13 we show the expected energy distribution function under the assumption $\Phi(E_\nu) \propto E_\nu^{-2}$:

$$F(\hat{E}_\nu) = \frac{\int_0^{\hat{E}_\nu} E_\nu^{-2} \, \mathcal{E}(E_\nu) \, \mathrm{d}E_\nu}{\int_0^{\infty} E_\nu^{-2} \, \mathcal{E}(E_\nu) \, \mathrm{d}E_\nu} \tag{7.17}$$

We define the range of energies containing 90% of expected events in a symmetrical way:

$$[E_m, E_M] \text{ with } F(E_m) = 0.05 \text{ and } F(E_M) = 0.95 \tag{7.18}$$

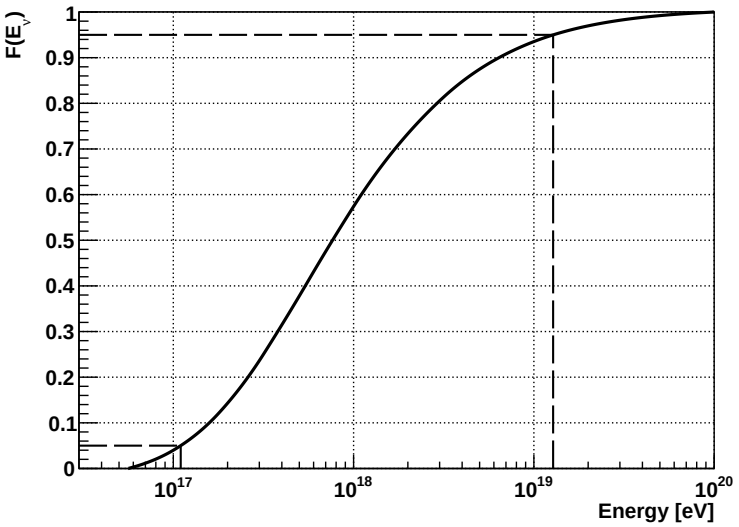

Figure 7.13 Expected energy distribution function $F(E_\nu)$ under the assumption of a flux with an energy dependence of E_ν^{-2}. In dashed we show the region which concentrates 90% of the expected events: $[10^{17}, 10^{19.1}]$ eV.

7.2.5 Systematic Uncertainties

The exposure calculation involves several factors. Some of them, such as the cross-section, the tau energy loss and the hadronic model, are not known with precision as they involve the extrapolation of measurements to uncharted kinematic regions. In this context, it is useful to classify the choices made in the exposure calculation into the following categories, as done in Chapter 4:

- Interactions in the Earth
- Interactions in the atmosphere

The purpose of this section is to describe the strategies used to estimate the uncertainty associated to these two groups and discuss the final result.

7.2.5.1 Interactions in the Earth

The probability density functions $f(E_\tau|\theta, E_\nu)$ used in the calculation of the exposure (see equation 7.11) depend on the adopted parametrizations for the cross-section and tau energy losses. A higher (lower) cross section for the neutrino charged interaction $\nu_\tau + N \to \tau + X$ (σ_{CC}) increases (decreases) the expected tau yield, so we refer to them as the optimistic (pessimistic) case. On the other hand, a higher

(lower) photonuclear interaction cross section, $\tau + N \to \tau + X$ (σ_γ), increases (decreases) the tau energy loss and diminishes (increases) the probability that it will emerge from the Earth and give rise to an atmospheric shower. We, thus, denote this as the pessimistic (optimistic) scenario.

Both the neutrino cross section and the tau photonuclear energy loss are calculated from theory using structure functions which carry the information of the nucleon and nucleus structure. In order to study the uncertainties in the calculation of Earth-skimming neutrinos the same structure functions should be consistently used for both processes due to their strong correlation in the resulting tau flux. Unfortunately this is not possible since the kinematical Q^2 (minus the squared momentum transfer) and Bjorken-x ranges that contribute to these processes are quite different, especially at EeV energies, and the available parametrizations are not entirely adequate to describe both ranges simultaneously.

The Q^2 scale that contributes to the tau energy loss, dominated by photon exchange, is low to moderate Q^2 at very low x, where nonperturbative QCD effects prevail. The CC neutrino cross section, on the other hand, is produced by W-boson exchange that sets the relevant scale of Q^2 to values up to M_W^2 at low x, a region where perturbative QCD is expected to work. In both cases the relevant x range lies well outside the regions where the structure functions are measured, so one has to rely on extrapolations which contain significant uncertainties.

We estimate their effect by choosing parametrizations for the cross-section and for the tau energy loss which correspond to extreme variations with respect to the reference case (see Section 4.1.3).

Model	Cross-section	Tau energy loss
Reference	Sarkar [97, 98]	ALLM [99, 104]
Pessimistic	ASW [99, 100]	PT [99, 105]
Optimistic	Armesto Sat. $\lambda = 0.4$ [99]	ASW [99, 100]

Table 7.1 Models considered to study the uncertainties for the processes that take place in the Earth.

In Figure 7.14 we show as an example how the energy distribution of the emerging taus changes according to the different choices, for the case of incident neutrinos with $E_\nu = 10^{18}$ eV and $\theta = 90.68°$. The integral of the three pdf, i.e. the total probability of a τ emerging from the Earth, are 1.3%, 0.5% and 1.7% for the reference, pessimistic and optimistic combinations, respectively. Moreover, there is a change in the shape. In the case of the pessimistic scenario, where the tau energy losses are high, it can clearly be seen that the peak of the distribution is shifted towards lower energies.

In order to take into account these changes we recalculate the exposure with the pessimistic and optimistic parametrizations of the cross-section and tau energy

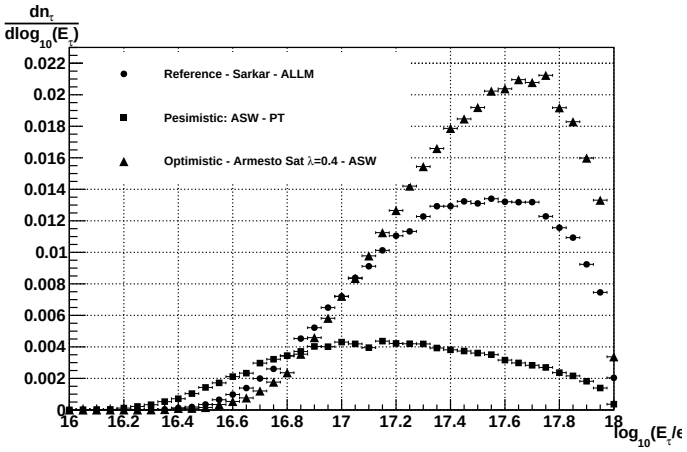

Figure 7.14 Energy probability density for an emerging tau. The function depends on the parametrizations of the cross-section and tau energy loss. In this example the energy is fixed at $E_\nu = 10^{18}$ eV and the zenith angle at $\theta = 90.68°$.

losses. The result is shown in Figure 7.15 where it can be seen that the optimistic scenario is higher than the reference by ∼15% at the lowest energies and it reaches a maximum of ∼50% at 10^{19} eV. On the other hand, the pessimistic scenario is lower by -45% at the lowest energies and it reaches -70% at 10^{18} eV. A calculation of the average differences weighted with a E^{-2} flux factor over the region where we expect 90% of the events yields a $[-65\%, +37\%]$.

In Figure 7.15 we also show the relative differences changing separately the cross-section or the tau energy losses. It is clear that tau energy losses are dominant over the entire energy range.

The dependence of the exposure on the neutrino cross section decreases due to the competition between two effects: the tau yield over the complete distance travelled through the Earth increases with the cross-section, while the fraction of τs produced in the range where they can emerge to the surface decreases.

7.2.5.2 Interactions in the atmosphere

The simulation of MC events initiated by a τ lepton involves two sources of systematic uncertainty:

1. The hadronic interaction model at high energy (QGSJETII).

2. The atmospheric shower evolution (AIRES 2.8 with a relative thinning of 10^{-6}).

where the actual option chosen to generate the MC sample of showers induced by a τ decay is indicated in parenthesis. To estimate the systematic uncertainty, we

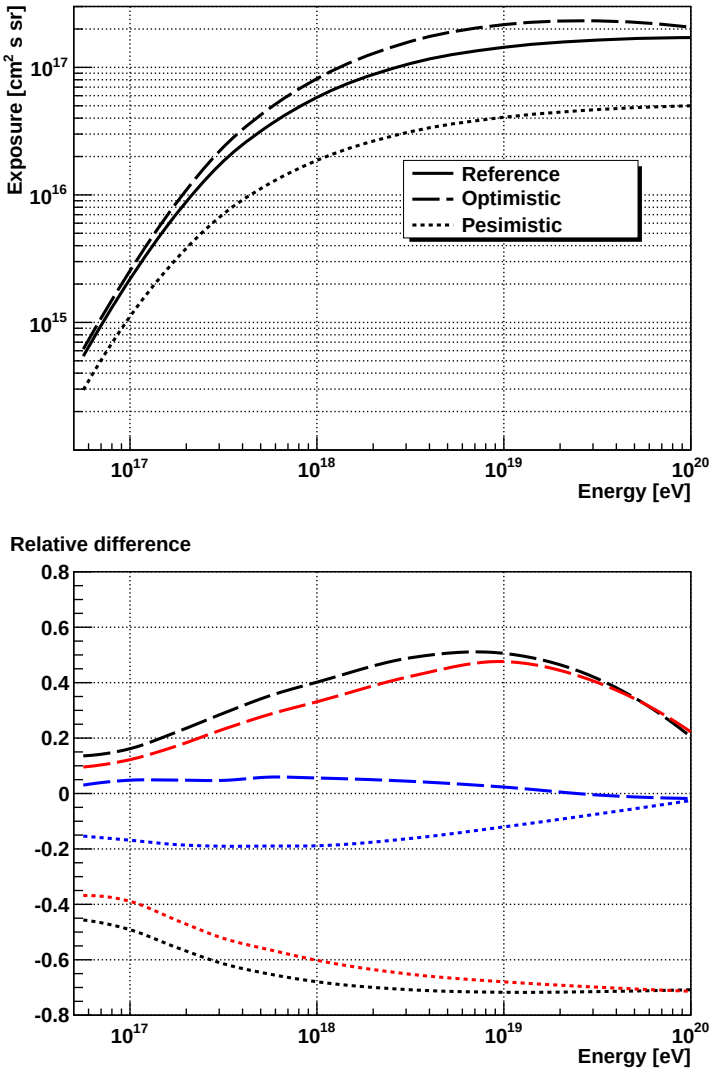

Figure 7.15 Effect of considering different parametrizations for the cross-section and tau energy loss in the exposure of the SD. *Top:* The exposure corresponding to the total period from 1 January to 31 December 2012. *Bottom:* Relative difference in the exposures for the different parametrizations considering that of Sarkar-ALLM as a reference. In blue (red) we show the differences corresponding to changing onlythe cross-section (tau energy losses).

used the simulations described in Section 4.2 as a reference and compared them to variations obtained when changing, one at a time, the involved models.

The complete set of simulations in all the (E_τ, θ, X_d) parameter space comprises ∼200000 events. It would be impracticable to re-simulate the full statistics for each systematic study.

The alternative is to select only a representative fraction of the parameter space. Accordingly, we chose 20 points having a high value of the weight, as defined in Section 4.3, Eq. 4.18. These 20 points are shown in Figure 7.16 and represent ∼30% of the total weight.

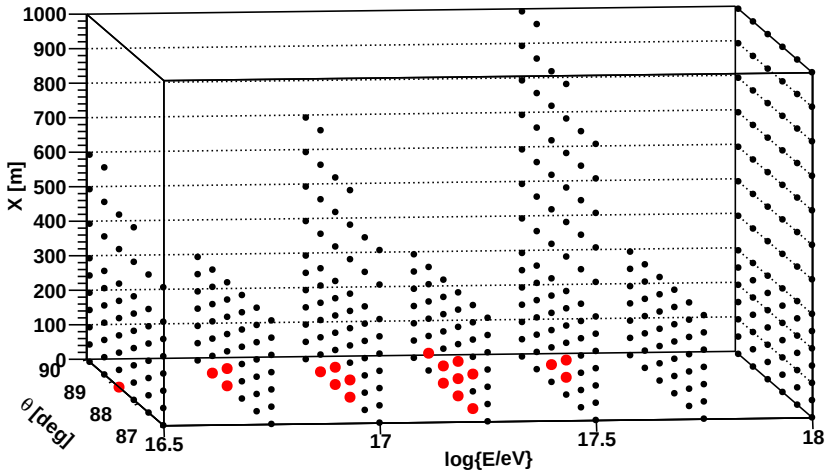

Figure 7.16 In black the points in the parameter space $\log_{10}\frac{E_\tau}{\mathrm{eV}}$, θ and decay height X_d, that have been simulated in the range $[16.5, 18]$, $[90°, 93°]$ and $[0, 1000\mathrm{m}]$ respectively. In red the selected points with high weight value selected to study the systematic uncertainties due to the interactions in the atmosphere.

The magnitude used to perform a comparison between the different models is the sum of the weights ($\sum_i w_i$, see Section 4.3) over the selected and identified showers, which is proportional to the number of expected events. In Table 7.2 we summarize the results. The differences obtained provide an estimation of the uncertainty between the selected models. It can be observed that the differences are small when compared to the statistical uncertainty (∼5%). This means that the systematics associated to the hadronic model or the thinning factor can be neglected.

Parameter	**Reference (A)**	**Modification (B)**	**Difference** $\frac{\mathbf{B-A}}{\mathbf{(B+A)/2}}$
Hadronic model	QGSJETII	QGSJETI [110]	+4.7%
		SIBYLL [109]	-1.0%
Thinning	10^{-6}	10^{-7}	+0.3%

Table 7.2 Summary of the relative differences between alternative models involved in the shower simulation. The statistical uncertainty in the relative differences is ∼5%.

In summary, the uncertaities in the interaction in the Earth dominate over the uncertainties of the simulation of the shower. In particular, the most important effect comes from the tau energy loss models.

8

Results and discussion

As described in Chapter 6, this work used a blind search scheme. The data analysed was divided into three groups: the first two, training and test samples, were used to characterize the detector and develop an algorithm for neutrino identification. The third, search sample, was not scanned until after defining the identification criteria. The procedure of applying the neutrino identification criteria to the events in the search sample is denominated colloquially as "opening the box"

In this Chapter we first apply the identification criteria to the Search sample (Section 8.1). In Sections 8.3 and 8.4 we analyze the number of expected neutrino events under different diffuse neutrino flux predictions and place a limit on the normalization of a flux with a E^{-2} dependence. Finally, in Section 8.5, we study the case of a high energy neutrino flux from a specific point in the sky (point-like sources) and place limits which are dependent on the declination of the source.

8.1 Blind search: "opening the box"

Once the identification criteria is defined, the next step is to analyse the search sample (1 June 2010 - 31 December 2012) applying the following steps:

1. Selection of quality events
2. Selection of inclined events
3. Calculation of the $\langle \text{AoP} \rangle$ for each event
4. Selection of events with $\langle \text{AoP} \rangle > \langle \text{AoP} \rangle_{cut} = 1.82$
5. For 3-station events, demand AoP_min > 1.4.

There are 0 candidates after applying these criteria. In Figure 8.1 we present the distribution of $\langle \text{AoP} \rangle$ for the events in the search sample. The number of expected events according to the background distributions predicted from the Test sample (see Section 6.6) and the number of actually measured events in the Search sample are compared in the four testing regions ($[3\sigma, 4\sigma]$, $[4\sigma, 5\sigma]$, $[5\sigma, 6\sigma]$ and $[6\sigma, 7\sigma]$). There is agreement between measurements and predictions in all the regions within the poissonian statistical fluctuations.

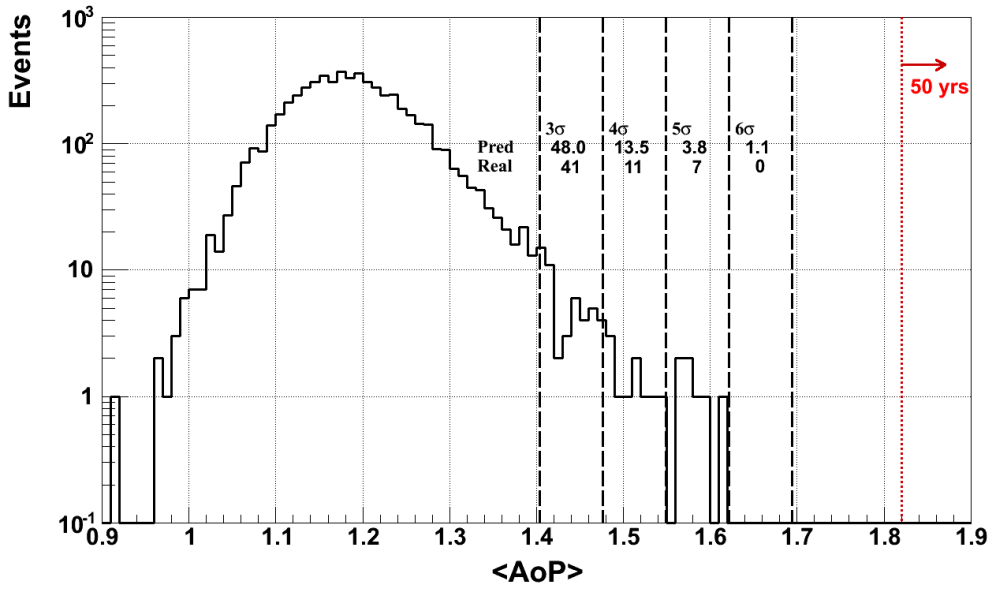

Figure 8.1 Distribution of $\langle \text{AoP} \rangle$ of the data events in the Search sample (1 June 2010 - 31 December 2012). The regions $[3\sigma, 4\sigma]$, $[4\sigma, 5\sigma]$, $[5\sigma, 6\sigma]$ and $[6\sigma, 7\sigma]$ are defined by the Test sample and are shown between dashed vertical lines (see Section 6.6). The predicted number of events for each region according to the exponential fit to the Test sample (Pred.) are in agreement with the number of measured events in the Search sample (Real).

We have also seen in Section 6.6.1 that there was an evolution of the calibrated value of area over peak from the Training sample to the Test sample. In Figure 8.2 we show the evolution with time of the mean value of the distribution of $\langle \text{AoP} \rangle$ including now the Search sample.

The rise in the average calibrated area over peak ($\langle \text{AoP} \rangle_{\text{cal}}$) seems to stop within the statistical uncertainties considered. The effect could be related to the observation that the uncalibrated vertical muon area over peak (AoP_{unc}) of single stations decreased with time by around 10% over the first years of data taking and then it stabelized [126]. This is the opposite pattern of Figure 8.2, which could result from an overcorrection for inclined muons due to the station area and peak calibration derived with vertical muons. Further studies need to be taken however to under-

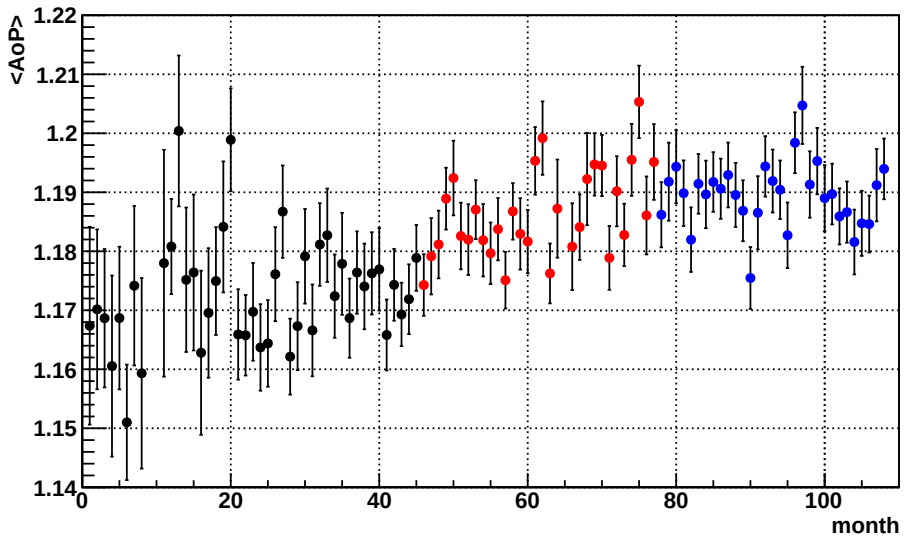

Figure 8.2 Mean value of the distribution of ⟨AoP⟩ per month, from January 2004 (month 0) to December 2012 (month 108). In black (red/blue) dots we show the months corresponding to the Training (Test/Search) sample.

stand this effect which is beyond the scope of this dissertation. We emphasize that this effect is nevertheless negligible for the estimation of the expected number of background events, as discussed in Section 6.6.2.

8.2 Comparison to theory: statistical treatment

In order to define the number of expected events necessary to reject a flux model with 90% confidence level (CL) it is instructive to consider first a simplified case in which we assume a negligible background and an exposure with no uncertainty. The number of observed events n is a random variable with a Poissonian distribution $P_\alpha(n)$, where α is the expected number of events. For a given theoretical prediction we refer to α as $N_{\rm signal}$, which is calculated as:

$$N_{\rm signal} = \int_{E_{\rm min}}^{E_{\rm max}} \Phi(E_\nu)\, \mathcal{E}(E_\nu)\, {\rm d}E_\nu \tag{8.1}$$

where $\Phi(E_\nu)$ is the neutrino diffuse flux under consideration, $\mathcal{E}(E_\nu)$ is the exposure of the detector and $[E_{\rm min}, E_{\rm max}]$ is the energy range.

If α is known, the probability of observing at least one neutrino is given by: $P_\alpha(n \geq 1) = 1 - P_\alpha(0)$. Inversely, knowing that the experiment observed no neutrino, the estimated confidence region of α with $p \times 100\%$ CL is defined as $P_\alpha(n \geq 1) < p$. This confidence region is $[0, \hat{\alpha}]$, where the estimator for the the upper limit, $\hat{\alpha}$, is

obtained from:

$$P_{\hat{\alpha}}(n \geq 1) = p \Rightarrow 1 - P_{\hat{\alpha}}(0) = p \Rightarrow P_{\hat{\alpha}}(0) = 1 - p \tag{8.2}$$

In particular, the upper limit with a 90% CL is:

$$1 - P_{\hat{\alpha}}(0) = 0.9 \Rightarrow 1 - e^{-\hat{\alpha}} = 0.9 \Rightarrow \hat{\alpha} \simeq 2.3 \Rightarrow 0 < \alpha < 2.3 \tag{8.3}$$

This simplified approach, presented only for pedagical reasons, presents essentially three shortcomings:

1. It does not allow for the possible presence of a background contribution to the number of observed events

2. It only applies for upper bounds, rather than offering a unified treatment that can also yield a range for alpha, with lower and upper limits, depending on the number of observed events.

3. It does not consider the contribution of systematic uncertainties to the estimator $\hat{\alpha}$.

The first two points were addressed by Feldman and Cousins (FC) [127], who proposed an unified approach for the classical statistical analysis of small signals based on the confidence belt frequentist construction and the likelihood ratio ordering method. Given a number of observed events, and a predicted background, the FC approach univocally produces upper bounds or confidence ranges. For the particular case of a background free experiment with no events observed, the FC prescription amounts to replace the factor 2.3 by 2.44 in equation 8.3:

$$\hat{\alpha}_{\text{poisson}} \simeq 2.3 \Rightarrow \hat{\alpha}_{\text{FC}} = 2.44 \Rightarrow 0 < \alpha < 2.44 \tag{8.4}$$

Although this scheme provides a unified framework to calculate the limits (upper and lower) with background, it does not include the treatment of systematic uncertainties. Conrad et al developed in [128] a semi bayesian extension of the method which incorporates the systematic contributions to the exposure $\mathcal{E}(E_\nu)$ and the background estimation, N_{bkg}. The fixed values of $\mathcal{E}(E_\nu)$ and N_{bkg} are replaced by probability density functions (pdf) $f(\mathcal{E})$ and $f(N_{\text{bkg}})$ which quantify our knowledge of their possible values.

Then, before applying this method it is necessary to establish the probability density functions which characterize the number of expected events N_{signal} and N_{bkg}. The pdf of N_{signal} is determined by the uncertainty on the total exposure. As discussed in Section 7.2.5.1, the uncertainty is [-65%, +37%] and we assume a uniform distribution for it.

In order to estimate N_{bkg} we recall that in Chapter 6 the neutrino identification criterion, $\langle \text{AoP} \rangle > 1.82$, was defined so that there is one expected background event in 50 years. As the Search period corresponds to 2.3 years of a fully deployed SD the actual expected background is $\sim \frac{2.3}{50} = 0.046$. The distribution of background is obtained from the linear extrapolation in log scale:

$$N_{\text{bkg}}^{2.3\text{yr}}(\langle \text{AoP} \rangle) = \frac{2.3}{2.0} e^{A - B\langle \text{AoP} \rangle} \tag{8.5}$$

where A and B are obtained from the fit to the Test sample, which corresponds to 2 years of a fully deployed SD. Under the assumption of binormal distribution of A and B, using the covariance matrix from the fit, we obtain a probability density function for the number of background events:

$$N_{\text{bkg}} = \frac{1}{\Delta\langle \text{AoP} \rangle} \int_{1.82}^{\infty} d\langle \text{AoP} \rangle \; N^{2.3\text{yr}}(\langle \text{AoP} \rangle) = \frac{1}{\Delta\langle \text{AoP} \rangle} \frac{2.3}{2.0} \frac{e^{A - B \times 1.82}}{B} \tag{8.6}$$

which is shown in Figure 8.3.

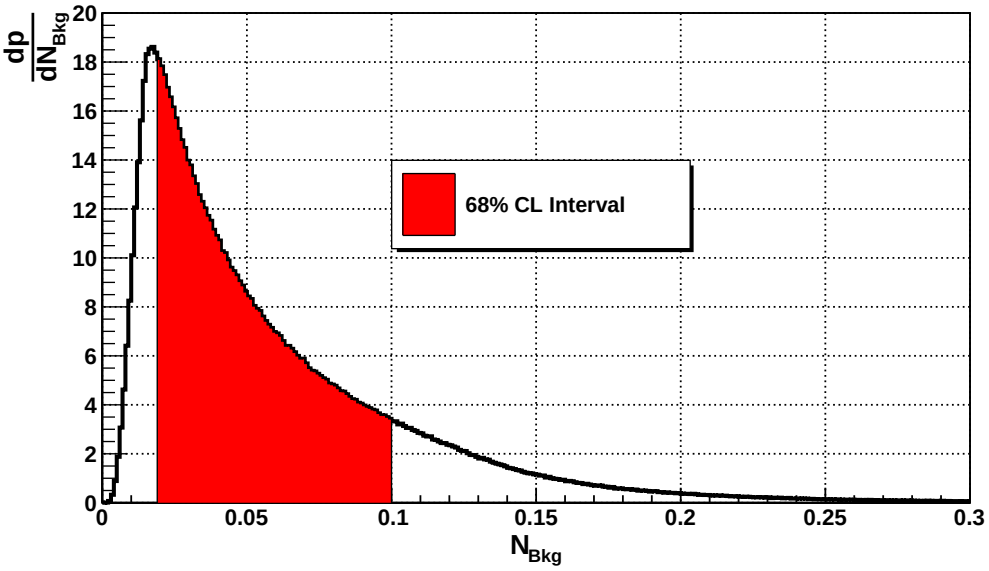

Figure 8.3 Probability density function of expected number of background events.

It has to be noticed that the period unblinded under the Old ES criteria has claimed 0 background events. Consequently, the 68% CL background expectation for the total period is $[0.02, 0.1]$, as shown in Figure 8.3.

Given that the estimated background is small and that it suffers from unknown systematic uncertainties, the number of background events will be assumed to be 0, which results in a more conservative (higher) $\hat{\alpha}$. Using the background free assumption but including the systematic uncertainties on the exposure, we obtain

that the 90% CL region for the number of expected events is:

$$\hat{\alpha}_{\text{Conrad}} = 3.21 \Rightarrow 0 < \alpha < 3.21 \tag{8.7}$$

This means that, for the case of zero observed events, the number of expected events should be greater than 3.21 to reject a given neutrino flux model. The increase on $\hat{\alpha}$ is the direct consequence of including the systematic uncertainties on the exposure which are asymmetrical and larger towards lower values. It is worth noticing that the method is not very sensitive to the choice of the functional form of the distributions of $\mathcal{E}$ or N_{bkg}. Moreover, if we included the effect of the small background estimated in Figure 8.3 $\hat{\alpha}_{\text{Conrad}}$ would be reduced from 3.21 to 3.13, which is negligible.

8.3 Testing theoretical predictions

As discussed in Chapter 1 there is large number of theoretical models predicting neutrino fluxes with energies around 1 EeV. Using the exposure $\mathcal{E}(E_\nu)$ accumulated by the Pierre Auger Collaboration from 1 January 2004 to 31 December 2012 the expected number of events, N_{signal}, for a diffuse neutrino flux $\Phi(E_\nu)$ can be obtained by integrating in energy as in equation 8.1.

The integration can be performed over the entire range of energy or in bins to analyse where the sensitivity of the detector is highest. It needs to be mentioned that $\Phi(E_\nu)$ is the flux of ν_τ, so in case $\Phi(E_\nu)$ corresponds to an all flavour flux, it needs to be divided by 3 under the assumption of the 1:1:1 ratio expected from neutrino oscillations over cosmological distances. In Figure 8.4 we show the expected number of events for the GZK-FermiLat flux prediction (presented in Section 1.2.1) as a function of energy. It can be seen that the sensitivity peaks at 10^{18} eV. This is to be expected as at high energy the flux decrease overcomes the rise in the exposure, while at energies below 10^{18} eV the lower exposure overcomes the higher flux. This behaviour applies to all models where the flux, to first order, behaves with energy as E^{-2}.

The expected signal from GZK-FermiLat diffuse flux of UHE neutrinos is $1.8^{+0.8}_{-1.2}$. The signal to background ratio is 18 considering the upper limit of the 68% CL interval for the background. This means that for this flux we are not limited by the background.

In Table 8.1 we summarize the results for the set of selected models presented in Section 1.2. We also estimate the additional data taking time needed to reject the model at 90% CL, under the assumption that no event is observed.

The most reliable prediction of existence of diffuse neutrinos corresponds to those of cosmogenic origin. As it can be seen there are a variety of models which predict the observation of $\sim$1 event within the present accumulated statistics. If

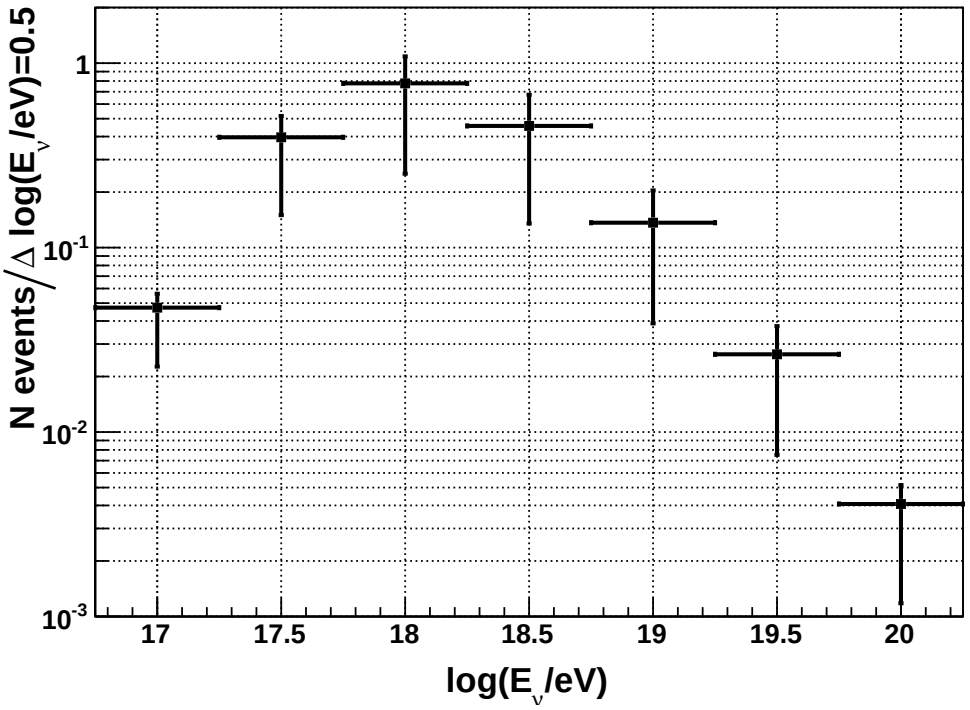

Figure 8.4 Number of expected events from the GZK neutrino flux prediction by Ahlers *et al.* [21] for the exposure accumulated by the Pierre Auger Collaboration from 1 January 2004 to 31 December 2012. The uncertainties arises from the different cross-sections and tau energy losses models considered in Section 7.2.5.1. The total numer of expected events is $1.8^{+0.8}_{-1.2}$.

these models are certain the Pierre Auger Observatory should expect an observation within the next few years. The most optimistic scenario, which corresponds to a FRII strong source evolution, a pure proton composition, and $E_c = 10^{21.5}$ eV, is already rejected at 90% CL. The most pessimistic scenario, i.e. a pure iron UHECR composition and uniform evolution, predicts a flux which is out of reach because the background estimation is higher than the expected signal. It must be noticed that even if not background limited the amount of data to collect would take more time than the observatory expected lifetime. The only chance of observing GZK fluxes predicted by pure iron composition models is to build radio detectors of high energy neutrinos in deep, radio-transparent ice near the South Pole such as ARA [66] or ARIANNA [67]. This detectors are expected to increase the exposure around 1 EeV in a factor between 10 and 100 with respect to Auger. However, they are still initiatives which are only in a development stage.

For the models where the neutrinos are produced at AGNs the prediction of the number of events is very different depending on the model and in particular on the cutoff energy (see Section1.2.2). If the cutoff is produced at energies around 1 EeV

Model	N_{expected}	Time for rejection
GZK-Engel [19]	1.2	6.1 yr.
GZK-FermiLat [21]	1.8	4.2 yr.
GZK-Yuksel [23]	1.8	4.2 yr.
GZK-KoteraTop [22]	0.8	7.4 yr.
GZK-KoteramBottom [22]	0.3	9.0 yr.
GZK-KoteramFRII [22]	4.2	**Rejected**
GZK-KoteramIron [22]	0.008	**Bkg. limited**
AGN-MPR-max [39]	14	**Rejected**
AGN-BBR [40]	5.9	**Rejected**
AGN-Stecker [41]	0.15	**Bkg. limited**
GRB- [43]	0.03	**Bkg. limited**
GRB- [44]	0.14	**Bkg. limited**
TD [45]	>5.4	**Rejected**
Z-Burst [45]	>7.6	**Rejected**

Table 8.1 Prediction, for the set of models described in Chapter 1 [19, 21–23, 39–41, 43–45], of the number of expected events for the period 1 January 2004 to 31 December 2012 using the Earth-skimming ν_τ search. In the third column we present an estimation of the additional data taking time needed to reject the model at 90% CL, under the assumption that no event is observed. If N_{expected} is higher than 3.21 the model is considered rejected while if it is comparable to 0.1 it is considered to be background limited.

the expected number of events is between 1 and 10. However, for scenarios where the cutoff is produced at ∼0.01 EeV the yield is below the observation limit. The search for neutrinos in this energy range is better suited for experiments like IceCube. The fluxes predicted by GRB are also out of reach for the observatory because they are too low compared with the background estimation.

In the case of exotic models predicting UHE neutrinos the number of expected events is usually higher than 3 so these models are disfavoured at more than 90% CL. It has to be mentioned that experiments like ANITA have already rejected these models in the past. Their sensitivity is better at energies higher than 10^{19} eV, as will be shown in Section 8.4.2.

8.4 Upper limit on the diffuse flux

From the no observation of neutrino events, in addition to testing the predictions from concrete models, it is customary to derive an upper bound on the diffuse flux of cosmological neutrinos on the assumption of an E^{-2} dependence of the spectrum [46].

8.4.1 Integral limit

If for the three neutrino flavours a typical differential flux with an energy dependence of $\Phi^{\nu_x} = k^{\nu_x} \cdot E_\nu^{-2}$ is chosen, the result is:

$$N_{\text{signal}}^{\text{total}} = N_{\text{signal}}^{\nu_e} + N_{\text{signal}}^{\nu_\mu} + N_{\text{signal}}^{\nu_\tau} \tag{8.8}$$

where each of the $N_{\text{signal}}^{\nu_x}$ is:

$$N_{\text{signal}}^{\nu_x} = k^{\nu_x} \underbrace{\int_{E_{\min}}^{E_{\max}} E_\nu^{-2}\, \mathcal{E}^{\nu_x}(E_\nu)\, \mathrm{d}E_\nu}_{\equiv \mathcal{N}(\mathcal{E}^{\nu_x})} = k^{\nu_x} \cdot \mathcal{N}(\mathcal{E}^{\nu_x}) \tag{8.9}$$

The magnitude $\mathcal{N}(\mathcal{E})$ has units of [GeV^{-1} cm^2 s sr] and depends only on the exposure $\mathcal{E}$. The integration is performed in the energy interval $[10^{17}, 10^{19.1}]$ eV that contains 90% of expected events, see Section 7.2.4. This is the standard definition of the upper limit. If a 1:1:1 ratio between flavours is assumed:

$$k^{\nu_e} = k^{\nu_\mu} = k^{\nu_\tau} \equiv k^{\text{SF}} = \frac{k^{\text{All}}}{3} \tag{8.10}$$

where k^{SF} is the normalization of a single flavour flux, equation 8.8 can be expressed in a more compact way:

$$N_{\text{signal}}^{\text{total}} = k^{\text{SF}} \cdot (\mathcal{N}^{\nu_e} + \mathcal{N}^{\nu_\mu} + \mathcal{N}^{\nu_\tau}) = k^{\text{SF}} \cdot \mathcal{N}^{\text{total}} = \frac{k^{\text{All}}}{3} \cdot \mathcal{N}^{\text{total}} \tag{8.11}$$

This expression allows us to obtain a limit over the magnitude of the total neutrino flux k^{All} [1]. If we consider the Feldman-Cousins approach in which we assume negligible background and no systematic uncertainty as it has been discussed in Section 8.2 an upper limit on k^{All} with 90% CL is set by:

$$\left.\begin{array}{l} N_{\text{signal}}^{\text{total}} = \frac{k^{\text{All}}}{3} \cdot \mathcal{N}^{\text{total}} \\ \\ N_{\text{signal}}^{\text{total}} \leq 2.44 \end{array}\right\} \Longrightarrow \frac{k^{\text{All}}}{3} \leq \frac{2.44}{\mathcal{N}^{\text{total}}} \tag{8.12}$$

If one uses the total exposure for the period 1 January 2004 to 31 December 2012, the result is:

$$k^{\text{All}} \leq 3.8 \times 10^{-8}\ \text{GeV cm}^{-2}\ \text{s}^{-1}\ \text{sr}^{-1} \tag{8.13}$$

over the energy range from 10^{17} eV to $10^{19.1}$ eV.

Including systematic uncertainties discussed in Section 8.2 with $N_{\text{signal}}^{\text{total}} \leq 3.21$

[1] The limit over the magnitude of the single flavour neutrino flux is obtained dividing k^{All} by 3.

the limit to the neutrino flux is:

$$k^{\mathrm{All}} < 5 \times 10^{-8}\ \mathrm{GeV\ cm^{-2}\ s^{-1}\ sr^{-1}} \tag{8.14}$$

over the energy range from 10^{17} eV to $10^{19.1}$ eV. It can be observed that the limit is worsened in $\sim 30\%$ because of the uncertainties in the exposure.

The result in equation 8.14 can be compared with the last results published by the IceCube and ANITA collaborations as they use the same procedure outlined here to obtain their limits. This is shown in Figure 8.5 together with predictions of a cosmogenic neutrino flux.

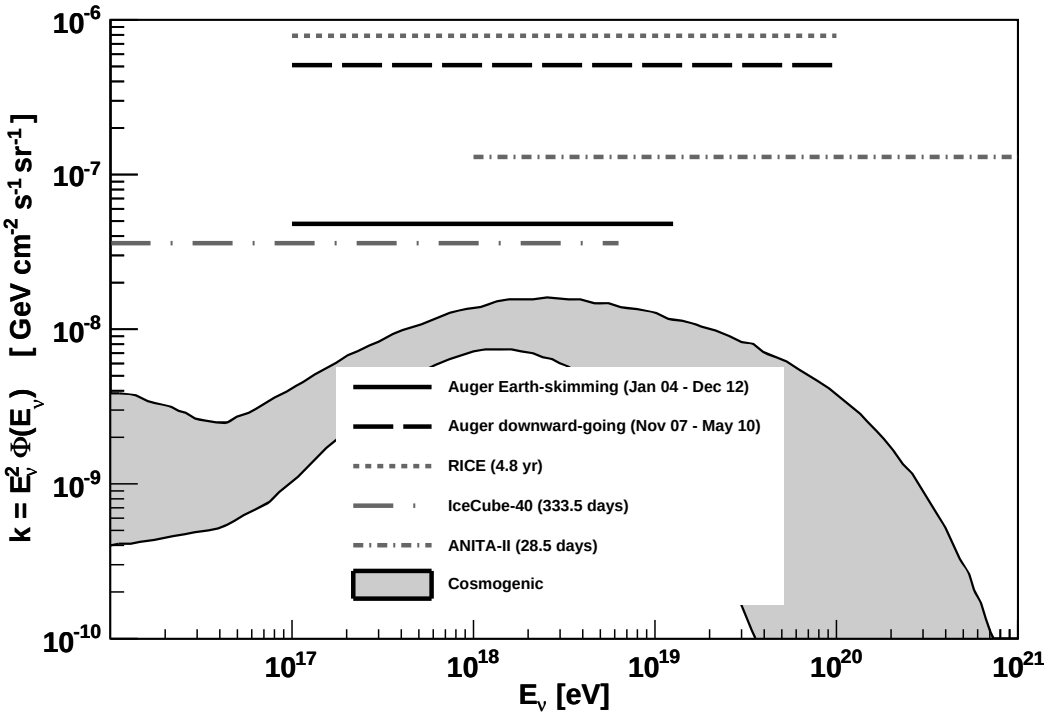

Figure 8.5 All flavour integrated limit to the diffuse neutrino flux (90% CL) obtained for Earth-skimming neutrinos using data acquired by the SD of the Pierre Auger Observatory in the period of 1 January 2004 and 31 December 2012. For comparison we show the limit to downward-going neutrinos (1 November 2007 to 31 May 2010) [75] and results of other experiments searching for neutrinos in similar energy ranges [50, 57, 59]. In grey the predictions from cosmogenic fluxes according to [22].

It is worth discussing the interpretation of this limit as it is not always clear. The limit is composed of three numbers: the value of k and the energy range which contain the 90% of the sensitivity. It is important to notice that if the range is larger, it does not necessarily mean that it is more restraining. For example, if we

consider two limits with the same k but the second one covers twice the range than the first one, this means that the first limit is twice more stringent than the second in the range of energies where they overlap. This is simply because the second limit needs to integrate over a larger range of energies to obtain the same bound. This is why, traditionally, the community not only compares integrated limits but also quasi-differential limits which are useful to quantify the sensitivity region of each experiment. Quasi-differential limits are explained in the following section.

8.4.2 Quasi-differential limit

In the calculation of the integrated limit it was necessary to assume that the neutrino flux depends on the energy like $\Phi(E_\nu) = k\,E^{-2}$, with constant k in the energy range from 10^{17} to $10^{19.1}$ eV. This hypotesis, although reasonable, can be incorrect and it is interesting to study the effect of replacing it with a less restrictive option: considering that the intensity of the flux k has a small dependence on the energy and, consequently, the approximation of the energy dependence E^{-2} is appropiate in small energy ranges.

In this way, around a defined energy $\tilde{E}$ there is a range in which the flux can be approximated by $k(\tilde{E})\,E^{-2}$ with $k(\tilde{E})$ constant so that the integrated limit can be calculated over a restricted range.

Including the systematic uncertainties by considering the factor 3.21, the upper limit in a range $\Delta E(E_\nu)$ which depends on the energy can be written as:

$$k(E_\nu) \leq \frac{3.21}{\mathcal{N}(E_\nu)} \quad \text{with} \quad \mathcal{N}(E_\nu) = \int\limits_{\Delta E(E_\nu)} E_\nu'^{-2}\,\mathcal{E}(E_\nu')\,\mathrm{d}E_\nu' \tag{8.15}$$

When choosing $\Delta E(E_\nu)$ such that all integration ranges have equal width in the logarithmic scale, the result is:

$$k(E_\nu) \leq 3.21 \Big/ \frac{1}{\ln 10} \int_{\log_{10}(E_\nu)-\Delta\log_{10}(E_\nu)/2}^{\log_{10}(E_\nu)+\Delta\log_{10}(E_\nu)/2} E_\nu'^{-1}\,\mathcal{E}(E_\nu')\,\mathrm{d}(\log_{10}(E_\nu')) \tag{8.16}$$

This way of presenting the upper limit is commonly denoted “quasi-differential limit”.

In Figure 8.6 the obtained differential limit is presented together with previous results in a similar energy range. It is interesting to notice that the limits set by the SD of the Pierre Auger Collaboration achieve maximum sensitivity in the same energy region where the flux of cosmogenic neutrinos is expected to peak. It can be seen that in the range of energies between 10^{17} and 10^{19} eV we place the most stringent limits. However, it needs to be noted that in one of the most recent publication of IceCube [51], where they present the first two PeV neutrinos, they analyse data from twice the effective lifetime and twice the number of strings than

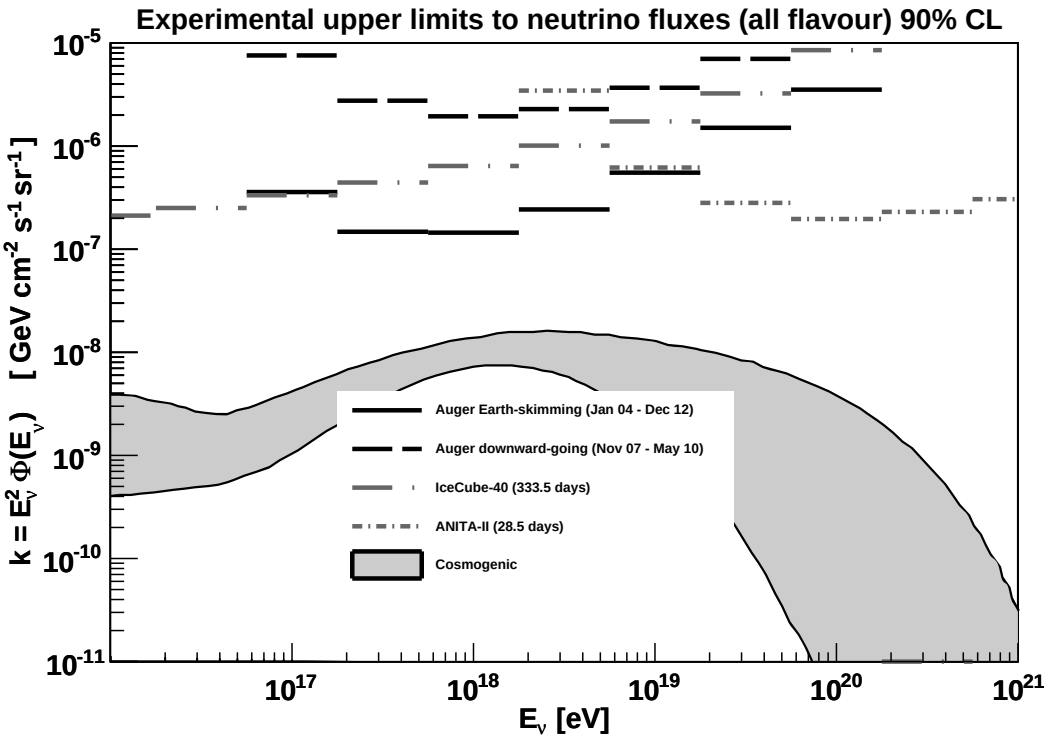

Figure 8.6 All flavour differential limits to the neutrino flux (90% CL) obtained for Earth-skimming neutrinos using data acquired by the SD of the Pierre Auger Observatory in the period of 1 January 2004 and 31 December 2012. For comparison we show the limit to down-going neutrinos (1 November 2007 to 31 May 2010) [75] and results of other experiments searching for neutrinos in a similar energy range [50, 59]. The Pierre Auger and ANITA differential limits are calculated with range of widths of half a decade ($\Delta \log_{10} E_\nu = 0.5$). The limit from the IceCube Neutrino Observatory is rescaled to the same width (the published result uses one decade in energy ($\Delta \log_{10} E_\nu = 1$) [50]).

the limit shown in Figure 8.6. Even though they have not presented the quasi-differential limit in this energy range for the new data set, it is fair to expect a limit improved by a factor 5. Using the new data set, their sensitivity in the range of energies between 10^{17} and 10^{19} eV is expected to be similar to the one obtained in this work.

8.5 Point Sources

In the previous sections we have presented limits to the diffuse neutrino flux at energies around 1 EeV. In this section we use the same identification criteria (discussed in Chapters 5 and 6) and the procedure to calculate the exposure (discussed

in Chapter 7) concentrating on the differences needed to constrain fluxes of UHEν coming from a particular region in the sky (point-like sources) instead of diffuse fluxes.

The first step is to study the sensitivity of the SD of the Pierre Auger Observatory as a function of the declination of the source (in equatorial coordinates). At each instant, Earth-skimming neutrinos can be detected only from a specific portion of the sky corresponding to a zenith angle range which is between 90° and 95°, where the exact range depends on the neutrino energy as shown in Figure 7.8.

A point-like source of declination δ and right ascension α (equatorial coordinates) is seen at the Pierre Auger Observatory (latitude $\lambda = -35.2°$), at a given sidereal time t, as having a zenith angle $\theta(t)$ given by:

$$\cos\theta(t) = \sin\lambda\,\sin\delta + \cos\lambda\,\cos\delta\,\sin(2\pi t/T - \alpha)\ , \tag{8.17}$$

where T is the duration of one sidereal day.

As an example we show in Figure 8.7 the zenith angle for three sources at different declination as a function of time.

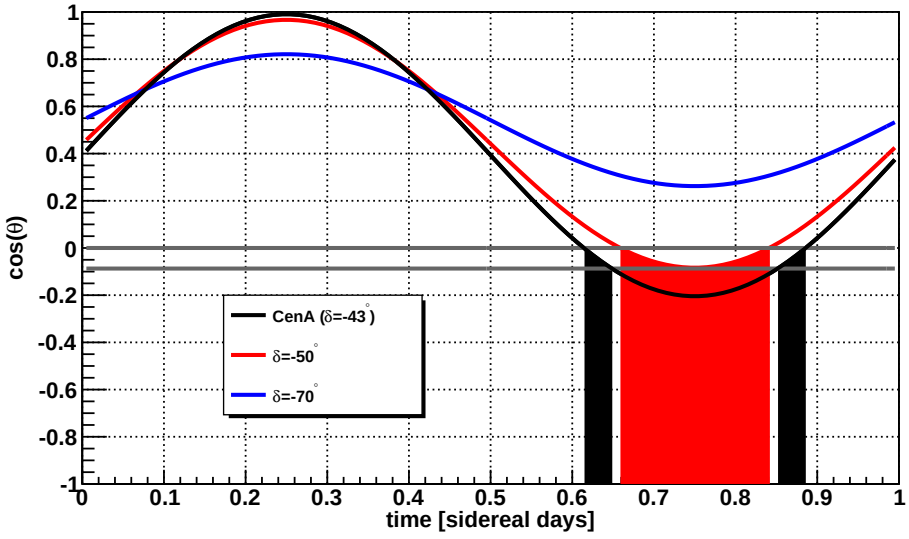

Figure 8.7 Cosine of the zenith angle as seen from the SD of the Auger Observatory (latitude $\lambda = -35.2°$) as a function of time for three declinations. Centaurus A ($\delta = -43°$) is visible ∼6.8% of the time with $90° < \theta < 95°$ (i.e. between the two horizontal lines in the figure) while a source at a declination $\delta = -52°$ is visible ∼18.3% of the time. Sources at declinations lower than $\delta = -55°$ are never within $90° < \theta < 95°$.

From equation 8.17, the fraction of a sidereal day during which a source is detectable by the Pierre Auger Observatory can be obtained. The result, shown in

Figure 8.8, depends only on the source declination. The SD of the Pierre Auger Observatory is sensitive to point-like sources of neutrinos over a broad declination range spanning from $\delta \sim -55°$ to $\delta \sim 60°$. The regions of the sky close to the Northern ($\delta = 90°$) and Southern ($\delta = -90°$) Terrestrial Poles are not accessible. The peaks in Figure 8.8 are a consequence of the relatively smaller rate of variation of zenith angle with time for declinations near the edges of the range accessible to this analysis.

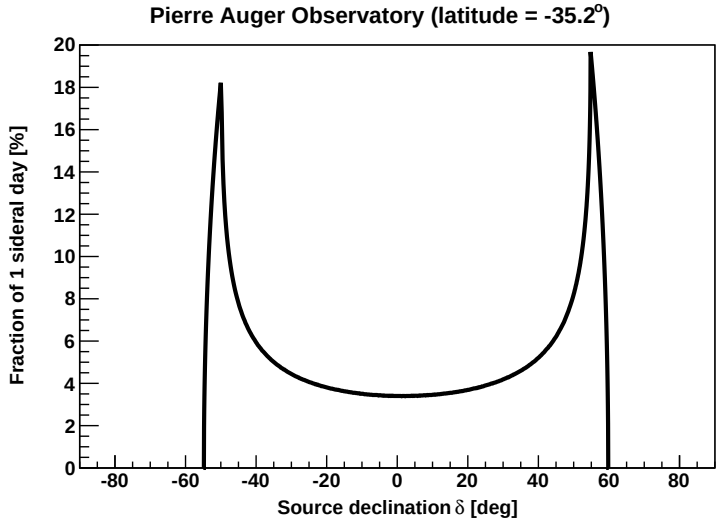

Figure 8.8 Fraction of a sidereal day having a point-like source at declination δ detectable by the Pierre Auger Observatory with the Earth-skimming.

The exposure of the SD as a function of the neutrino energy and of the source position in the sky, $\mathcal{E}(E_\nu, \delta, \alpha)$, is evaluated by folding the SD effective area with the probability density functions. The procedure is identical to that used for the calculation of the exposure for a diffuse flux of UHEνs, with the exception of the solid angle integration (see equation 7.10 for comparison):

$$\mathcal{E}_{PS}(E_\nu,\, \delta,\, \alpha) = \frac{d\mathcal{E}_{\text{diffuse}}}{d\Omega} = \int dt \int dE_\tau \int dX_D \left[f(E_\tau|\theta, E_\nu)\, h(X_D|E_\tau, \theta) \right.$$
$$\left. |\cos\theta(t)|\, \mathcal{A}_{\text{eff}}(E_\tau, \theta, X_D, t) \right] \qquad (8.18)$$

Changes in the detector configuration during data taking, due to the dead times of the SD stations, and to the increase of the array size during the construction phase, may introduce a dependence of the exposure on the right ascension. However, when averaged over a large number of sidereal days, as is the case in this work, the modulation in right ascension caused by this effect is less than 1%. For this reason, the dependence of the exposure on α can be neglected.

The dependence of the exposure on the source declination comes through $\theta(t)$ as obtained from equation 8.17. The integration over time, only considers those periods when the source is within the zenith angle range of the neutrino selection.

The expected number of neutrino events in an energy range $[E_{\rm min}, E_{\rm max}]$ detected by the Pierre Auger Observatory from a point-like source located at a declination δ is given by:

$$N_{\rm expected}^{\rm point\ source}(\delta) = \int_{E_{\rm min}}^{E_{\rm max}} F(E_\nu, \delta)\, \mathcal{E}(E_\nu, \delta)\, {\rm d}E_\nu \ , \tag{8.19}$$

where $F(E_\nu, \delta)$ is the differential flux of UHEνs from a source at a declination δ so it is the intensity per unit of time, area and energy[2].

We have already mentioned that no candidate events have been found. Assuming a differential flux with an energy dependence of $F(E_\nu,\, \delta) = k_{PS}(\delta) \cdot E_\nu^{-2}$, a 90% C.L. upper limit on the neutrino flux from point-like sources can be obtained following the same considerations as in Section 8.4.

In Figure 8.9, the 90% C.L. upper limit on k_{PS} is shown as a function of source declination. Limits for k_{PS} at the level of $\approx 8 \times 10^{-7}$ GeV cm^{-2} s^{-1} are obtained over a broad range of declinations considering Earth-skimming neutrinos.

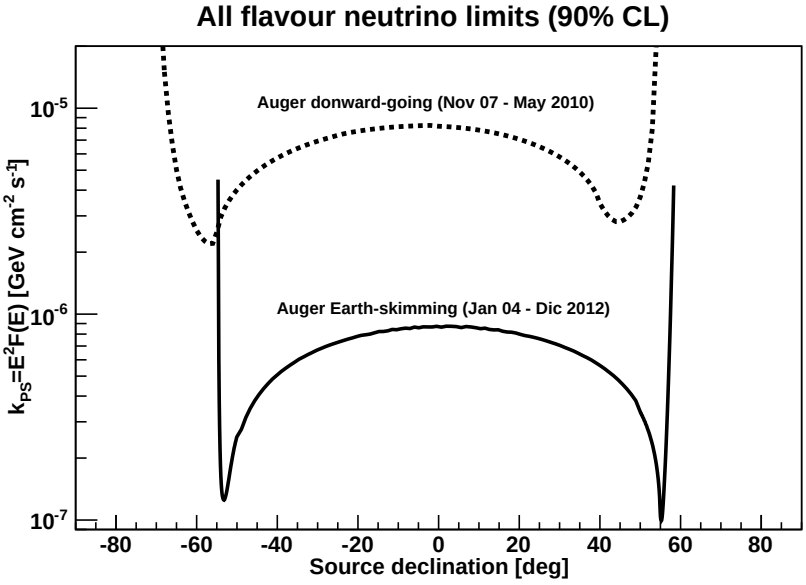

Figure 8.9 Upper limits at 90% C.L. on an all flavour E_ν^{-2} flux from a specific point-like source as a function of the source declination.

The shape of the declination-dependent upper limits is largely determined by the fraction of time a source is within the field of view (see Figure 8.8), and, to a lesser extent, by the zenith angle dependence of the exposure.

[2]The diffuse flux $\Phi(E_\nu)$ is the intensity per unit of time, area, energy and solid angle.

The upper limits are derived for neutrinos in the energy range 10^{17} eV$-10^{19.1}$ eV, with a negligible dependence of these energy intervals on the source declination. This is the best limit in the literature around 1 EeV. The IceCube Neutrino Observatory and the Antares Neutrino Telescope have also searched for UHEνs from point-like sources ([129] and [130], respectively). The bounds obtained by these two experiments apply to energies below the Auger energy range.

Limits for the particular case of the active galaxy Centaurus A, a potential source of UHECRs, are shown in Figure 8.10, together with constraints from other experiments. The predicted fluxes for two theoretical models of UHEν production in the jets [131] and close to the core [132] of Centaurus A are also shown for comparison. The expected number of events for these models are 0.2 and 0.04 respectively, beyond the present reach of the experiment.

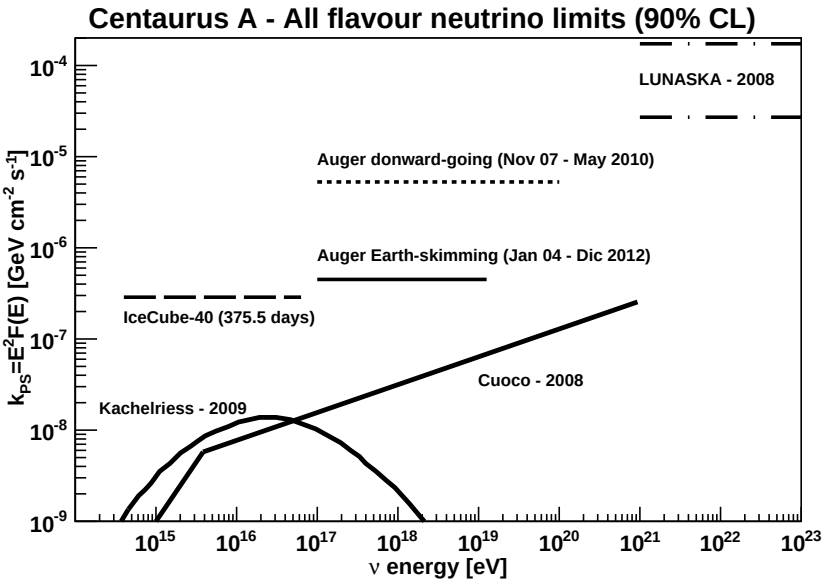

Figure 8.10 Upper limits at 90% C.L. on a single flavour E_ν^{-2} flux from the active galaxy Centaurus A from the Earth-skimming and downward-going neutrino analyses, together with bounds from the IceCube Neutrino Observatory [129] and LUNASKA [133]. The predictions for two models of UHEν production – in the jets [131], and close to the core [132] of CenA – are also shown.

9

Conclusions

This Thesis presents a search for ultra-high energy cosmological Earth-skimming tau neutrinos with the Surface Detector of the Pierre Auger Observatory.

A tau neutrino can turn into a tau lepton in the Earth crust via a charged-current weak interaction. If close enough to the Earth surface, the emerging τ will decay in the atmosphere giving rise to a nearly horizontal shower which can be detected by the surface array of the water-Cherenkov stations.

The original steps developed for this work involve the simulation of neutrino-induced showers (Chapter 4), the design of reconstruction techniques for highly inclined events (Chapter 5), devising algorithms to identify neutrino showers from the dominant background of hadronic cosmic rays (Chapter 6), the determination of the exposure of the observatory, i.e., its potential for discovery (Chapter 7), and finally the extraction of physical conclusions (Chapter 8).

A full simulation chain, from the incident neutrino up to the signals from the phototubes in the water-Cherenkov detectors, was set up to study in detail the expected characteristics of neutrino-induced upgoing quasi-horizontal showers. Inclined events above 10^{17} eV were reconstructed from their footprint on the surface stations, and identification criteria for neutrinos were developed exploiting their significant electromagnetic component. The expected background to the neutrino signal was estimated from a careful study of the fluctuations of the detector, and the characteristics of regular hadronic cosmic rays. Finally, a method was developed to compute the observatory exposure by convoluting the effective area of the surface detector with the probability density functions that describe the interaction of the neutrino, the tau propagation and energy loss in the Earth and their decay in the atmosphere, together with a thorough consideration of their sources of systematic uncertainties.

We used the developed analysis tools to search for neutrinos in the data collected from 1 January 2004 to 31 December 2012, with no candidates found. This result allowed for a number of physical conclusions.

First, we tested different astrophysical models of neutrino production, which comprise the cosmogenic mechanism, active galactic nuclei, gamma ray bursts, as well as unconventional sources. We established which models are rejected with the present data, and estimated which will be within the reach of the Pierre Auger Observatory during the next few years.

Assuming a differential flux $\Phi(E_\nu) = k\,E_\nu^{-2}$ in the energy range from 10^{17} to $10^{19.1}$ eV, we placed a 90% CL upper bound on the all flavour neutrino diffuse flux of $k < 5 \times 10^{-8}$ GeV cm^{-2} s^{-1} sr^{-1}.

Last, we imposed limits to the fluxes from point-like sources as a function of declination. In particular, for the active galaxy Centaurus A, a potential source of ultra-high energy cosmic rays, we established an all flavour 90% CL upper bound of $k_{\rm CenA} < 4.5 \times 10^{-7}$ GeV cm^{-2} s^{-1}, for a $k_{\rm CenA}\,E_\nu^{-2}$ differential flux.

Appendix A:

Top-Down Selection

In this appendix we briefly review the reconstruction of the shower axis.

1. Calculate the barycenter, according to:

$$\boldsymbol{r_b} = \frac{\sum \boldsymbol{r_i} S_i^{\frac{1}{3}}}{\sum S_i^{\frac{1}{3}}} \tag{9.1}$$

   where $\boldsymbol{r_i}$ and S_i are the ground position and integrated signal of the station. In the following, $\boldsymbol{r_i}$ denotes the station coordinates relative to the barycenter.

2. Fit a plane shower front model moving with the speed of light to the signal start times t_i , while neglecting the individual altitude z_i of each station with respect to the ground plane:

$$c(t_i - t_0) = -\boldsymbol{a}\boldsymbol{r_i} \Longleftrightarrow \langle t_i \rangle = t_0 - \frac{1}{c}(ux_i + vy_i) \tag{9.2}$$

   where $\boldsymbol{a} = (u, v, w)^T$ is the shower incoming direction. Free parameters of the model are u, v, and t_0 . A unique and fast solution can be obtained from the linear least squares method for parameter estimation.

3. The shower front fit is improved by approximately taking into account the altitude of the stations:

$$\langle t_i \rangle = t_0 - \frac{1}{c}(ux_i + vy_i + w_0 z_i) \tag{9.3}$$

   where $w_0 = \max(0, 1 - u_0^2 - v_0^2)$ is the fixed vertical component of the normalised shower direction from the first fit. Because w_0 is not considered as a free parameter, the linear least squares method can still be applied.

Bibliografy

[1] F. Halzen *et al.*, Rep. Prog. Phys. **65**, 1025 (2002);
P. Bhattacharjee *et al.*, Phys. Rep. **327**, 109 (2000);
J.K. Becker, Phys. Rep. **458**, 173 (2008).

[2] K. Greisen, Phys. Rev. Lett. **16**, 748 (1966).

[3] G.T. Zatsepin and V.A. Kuzmin, JETP Lett. **4**, 78 (1966).

[4] HiRes Collaboration, Phys.Rev.Lett. **100**, 101101 (2008).

[5] M. Takeda *et al.*, Astropart.Phys. **19**, 447 (2003).

[6] Pierre Auger Collaboration, Eur. Phys. J. Plus, **127**, 87 (2012).

[7] R. J. Gould and G. Schreder, Phys. Rev. Lett., **16**, 252 (1966).

[8] J. V. Jelley, Phys. Rev. Lett. **16**, 479 (1966).

[9] G. Setti *et al.*, Nature Physical Science **231**, 57 (1971).

[10] R. J. Protheroe and P. L. Biermann, Astropart. Phys. **6**, 45 (1996).
Erratum-ibid. **7**, 181 (1997). astro-ph/9605119.

[11] M. Risse *et al.*, Mod. Phys. Lett. A **22**, 749 (2007).

[12] V.S. Berezinsky and G. T. Zatsepin, Phys. Lett. **28B**, 423 (1969).
V.S. Berezinsky y G. T. Zatsepin, Sov. J. Nucl. Phys. **11**, 111 (1970).

[13] F. W. Stecker, Astrophys. Space Sci. **20**, 47 (1973).
F. W. Stecker, ApJ **228**, 919 (1979).

[14] F. W. Stecker *et al.*, Physical Review Letters **66**, 2697 (1991).

[15] E. Waxman and J. Bahcall, Physical Review Letters **78**, 2292 (1997).

[16] S. Yoshida *et al.*, Astrophys.J. **479**, 547 (1997).

[17] T. Weiler, Phys. Rev. Lett. **49**, 234 (1982).

[18] L. A. Anchordoqui and T. Montaruli, Annual Review of Nuclear and Particle Science **60**, 129 (2010).

[19] R. Engel *et al.*, Phys. Rev. D **64**, 093010 (2001).

[20] M. Ave *et al.*, Astroparticle Physics **23**, 19 (2005).

[21] M. Ahlers *et al.*, Phys. Rev. D **72**, 023001 (2005).

[22] D. Allard *et al.*, Journal of Cosmology and Astroparticle Physics **09**, 005 (2006).

[23] H. Yuksel and M. D. Kistler, Phys. Rev. D **75**, 083004 (2007).

[24] D. Hooper *et al.*, Astroparticle Physics **23**, 11 (2005).

[25] F. W. Stecker, Phys. Rev. **180** no. 5, 1264 (Apr, 1969).

[26] Pierre Auger Collaboration, Physical Review Letters **104** no. 9, 091101 (2010).

[27] Telescope Array Collaboration, "Ultra-high energy cosmic-ray spectra measured by the Telescope Array experiment from hybrid observations", 32nd International Cosmic Ray Conference. 2011.

[28] N. A. Bahcall, J. P. Ostriker *et al.*, Science **284**, 1481 (1999).

[29] S. M. Carroll, Living Reviews in Relativity **4**, 1 (2001).

[30] A. J. Bunker *et al.*, Mon.Not.Roy.Astron.Soc. **355**, 374 (2004).

[31] D. Hopkins and J. F. Beacom, ApJ **651**, 142 (2006).
H. Yuksel *et al.*, ApJ **683**, L5 (2008).

[32] M. Lemoine and E. Waxman, Journal of Cosmology and Astro-Particle Physics **11**, 9 (2009).

[33] J. V. Wall *et al.*, Astronomy and Astrophysics **434**, 133 (2005).

[34] T. Le and C. D. Dermer, ApJ **661**, 394 (2007).

[35] E. Roulet *et al.*, JCAP01, 028 (2013).

[36] T. K. Gaisser, F. Halzen, and T. Stanev, Physics Reports **258** no. 3, 173 (1995).

[37] E. Fermi, Phys. Rev. **75** (1949).

[38] R. J. Protheroe, "High energy neutrinos from blazars," arXiv:astro-ph/9607165.

[39] K. Mannheim, R. J. Protheroe, and J. P. Rachen, Phys. Rev. D **63** no. 2, 023003 (2001).

[40] J. K. Becker *et al.*, Astropart. Phys. **23** 355, (2005).

[41] F. W. Stecker, Phys. Rev. D **72** no. 10, 107301 (2005).

[42] E. Waxman, S. R. Kulkarni, and D. A. Frail, Astrophys.J. **497**, 288 (1998).

[43] E. Waxman and J. N. Bahcall, Astrophys.J. **541**, 707 (2000).

[44] S. Razzaque, P. Meszaros, and E. Waxman, Physical Review Letters **90** no. 24, 241103 (2003).

[45] O. Kalashev *et al.*, Phys. Rev. D **66**, 063004 (2002).

[46] E. Waxman and J. N. Bahcall, Phys.Rev. **D59**, 023002 (1999).

[47] E. Waxman, Astrophys.J. **452**, L1 (1995).

[48] F. Halzen and S. R. Klein, Phys.Today **61N5**, 29 (2008).

[49] BAIKAL and TUNKA Collaboration, Nuclear Instruments and Methods A **442** no. 1, 368 (2000).

[50] IceCube Collaboration, Phys. Rev. D **83** no. 9, 092003 (2011).

[51] IceCube Collaboration, Phys. Rev. Lett. **111**, 021103 (2013).

[52] Antares Collaboration, Astroparticle Physics **26**, 314 (2006).

[53] NEMO Collaboration, Nuclear Physics B Proceedings Supplements **143**, 359–362 (2005).

[54] The Nestor Collaboration, Nuclear Instruments and Methods in Physics Research A **552** 420 (2005).

[55] Km3NeT Collaboration, Nuclear Instruments and Methods in Physics Research A **602**, 98 (2009).

[56] G. A. Askar'yan, Soviet Journal of Experimental and Theoretical Physics **21**, 658 (1965).

[57] RICE Collaboration, Phys.Rev. **D73** 082002 (2006).

[58] ANITA Collaboration, Phys.Rev.Lett. **103**, 051103 (2009).

[59] ANITA Collaboration,Phys. Rev. D **82**, 022004 (2010);
Erratum arXiv:1011.5004v1 [astro-ph]

[60] P. W. Gorham *et al.*, Phys. Rev. Lett. **93** 041101 (2004).

[61] R. Dagkesamansky *et al.*, Int.J.Mod.Phys. **A21S1**, 142 (2006).

[62] C. W. James *et al.*, Mon.Not.Roy.Astron.Soc. **379**, 1037 (2007).

[63] O. Scholten *et al.*, J.Phys.Conf.Ser. **81** 012004 (2007).

[64] www.skatelescope.org

[65] C. W. James *et al.*, Phys.Rev. **D81** 042003 (2010).

[66] P. Allison *et al.*, arXiv:1105.2854 [astro-ph.IM].

[67] S. W. Barwick, Journal of Physics Conference Series **60**, 276 (2007).

[68] T. Barrella, S. Barwick, and D. Saltzberg, Journal of Glaciology **57**, 61–66 (2011).

[69] P. Gorham *et al.*, Nuclear Instruments and Methods A, **490** no. 3, 476 (2002).

[70] J. Alvarez-Muniz *et al.*, Int.J.Mod.Phys. **A21S1**, 55 (2006).

[71] R. D. Stewart and R. R. Unterberger, Geophysics **41** no. 1, 123 (1976).

[72] HiRes Collaboration, arXiv:0803.0554 [astro-ph].

[73] HiRes Collaboration, arXiv:0707.4417 [astro-ph].

[74] Pierre Auger Collaboration, Nucl.Instrum.Meth. **A523**, 50 (2004).

[75] Pierre Auger Collaboration, Phys. Rev. D **84**, 122005 (2011).

[76] Pierre Auger Collaboration, Phys. Rev. Lett., **100**, 211101 (2008).

[77] Pierre Auger Collaboration, Astrophysical Journal Letters, **755**, L4 (2012).

[78] J. Abraham *et al.* Pierre Auger Collaboration, Astropart. Phys. **27**, 155 (2007); J. Abraham *et al.* Pierre Auger Collaboration, Astropart. Phys. **31**, 399-406 (2009).

[79] W. Heitler, The Quantum Theory of Radiation, third ed., Oxford University Press, London, p. 386 (Section38), (1954).

[80] I. Valiño (PhD thesis), Univ. de Santiago de Compostela, ISBN: 9788497509664 (2008).

[81] J. Tiffenberg (PhD thesis), Univ. de Buenos Aires (2011).

[82] R. Gandhi *et al.*, Astropart. Phys. 5 (1996) 81.

[83] J. G. Learned *et al.*, Astropart. Phys. **3**, 267 (1995).

[84] Super-Kamiokande Collaboration, Phys. Rev. Lett. **81**, 1562 (1998).

[85] D. Fargion, Astrophys. J. **570**, 909 (2002).

[86] A. Letessier-Selvon, AIP Conf. Proc. **566**, 157 (2001).

[87] J. L. Feng *et al.*, Phys. Rev. Lett. **88**, 161102 (2002).

[88] M. Fukushima, Prog. Theor. Phys. Supplement **151** 206 (2003).

[89] G. I. Rubtsov *et al.*, Phys. Rev. D **73**, 063009 (2006)

[90] AGASA Collaboration, NIM **311**, 338 (1992).

[91] R. N. Coy *et al.*, Astroparticle Physics, 6, (1997).

[92] Pierre Auger Collaboration, Nucl. Instrum. Meth. A **523**, 50 (2004).

[93] Pierre Auger Project Design Report, (1997).

[94] Pierre Auger Colaboration, Nuclear Instruments & Methods A, **523**, 50 (2004).

[95] X. Bertou et al., Nuclear Instruments & Methods A **568**, 839 (2006).

[96] Pierre Auger Collaboration, Nuclear Instruments and Methods A **613**, 29 (2010).

[97] A. Cooper-Sarkar and S. Sarkar, JHEP **0801**, 075 (2008).

[98] Amanda Cooper-Sarkar, Philipp Mertsch, Subir Sarkar. JHEP **08**, 042 (2011).

[99] N. Armesto *et al.*, Phys. Rev. D **77**, 013001 (2008).

[100] N. Armesto *et al.*, Phys. Rev. Lett. **94**, 022002 (2005).

[101] S. I. Dutta *et al.*, Phys. Rev. D **63**, 094020 (2001).

[102] A. A. Petrukhin et V.V. Shestakov, Can. J. Phys. **46**, S377 (1968).

[103] R. P. Kokoulin et A. A. Petrukhin, Proc. of the 12^{th} ICRC, Australia, Vol **6**, 2436 (1971).

[104] H. Abramowicz *et al.*, Phys. Lett. B **269**, 465 (1991);
H. Abramowicz and A. Levy, hep-ph/9712415.

[105] D. A. Timashkov and A. A. Petrukhin, Procs. 29th International Cosmic Ray Conference, Vol 9, 89, 2005

[106] S. Jadach *et al.*, Comput. Phys. Commun. **76**, 361 (1993).

[107] *http://www-ik.fzk.de/corsika*

[108] S. Sciutto, AIRES. *http://www.fisica.unlp.edu.ar/auger/aires*

[109] *http://arxiv.org/abs/0906.4113*

[110] *http://arxiv.org/abs/0706.3784*

[111] *http://arxiv.org/abs/astro-ph/0412591v1* and *http://arxiv.org/abs/hep-ph/0412332*

[112] A. M. Hillas, Proceedings of the 17th International Cosmic Ray Conference, Paris Vol. 8, 193 (1981).

[113] S. Argiro *et al.*, Nucl. Instrum. Meth. A **580**, 1485-1496 (2007).

[114] Pierre Auger Collaboration, Procs. 30th International Cosmic Ray Conference 2007, #0300, Merida, Mexico.

[115] P. Billoir, Astropart. Phys. **30**, 270-285 (2008).

[116] *http://geant4.web.cern.ch/geant4/*

[117] Pierre Auger Collaboration, Nucl. Instr. and Meth. A **613**, 29-39 (2010).

[118] I. Lhenry-Yvon and P. L. Ghia,"Implementation of PMTs Quality Cuts in Auger Sd Data", Auger internal note GAP-2009-080 (2009); I. Lhenry-Yvon, "CDAS production v1r0: overview of new data avialable", Auger internal note GAP-2012-077 (2012).

[119] P. Lipari, Astropart. Phys. **1**, 195–227 (1993).

[120] J. Blumer, "On the influence of accidental muons on air shower detection", Auger internal note GAP-2008-110 (2008).

[121] P. Billoir, "FADC trace cleaning in Surface Detector through a segmentation procedure", Auger internal note GAP-2005-074 (2005).

[122] P. Billoir, "Top-down Selection of Events and Stations in Surface Detector Triggers", Auger internal note GAP-2006-072 (2006).

[123] P. Billoir, "Reconstruction of first year EA events from the Surface Detector", Auger internal note GAP-2002-044 (2002).

[124] A. Roodman, PHYSTAT2003, 166 (2003).

[125] X. Berotu *et al.*, Astropart.Phys, **17** 183(2002).

[126] H. Wahlberg, "Long Term Evolution of the VEM Area to Peak ratio", Auger internal note GAP-2002-044 (2002).

[127] G. J. Feldman and R.D Cousins, Phys. Rev. D **57**, 3873 (1998).

[128] J. Conrad *et al.*, Phys. Rev. D **67** 12002 (2003).

[129] IceCube Collaboration, Astrophys. J. **732**, 18 (2011).

[130] Antares Collaboration, Astrophys. J. Lett. **743**, L14 (2011).

[131] A. Cuoco and S. Hannestad, Phys. Rev. D **78**, 023007 (2008).

[132] M. Kachelriess, S. Ostapchenko and R. Tomas, New J. Phys. **11**, 065017 (2009).

[133] LUNASKA Collaboration, MNRAS **410**, 885 (2011).